NTNU

Norwegian University of
Science and Technology

Dynamic Identification and Modelling of a Pantograph

Anders Nygaard Knutzen

John-Arne Berg Sivertsen

Civil and Environmental Engineering
Submission date: June 2018
Supervisor: Anders Rönnquist, KT
Co-supervisor: Stefano Derosa, KT
Petter Røe Nåvik, KT

Norwegian University of Science and Technology
Department of Structural Engineering

Department of Structural Engineering
Faculty of Engineering
NTNU- Norwegian University of Science and Technology

ACCESSIBILITY

MASTER THESIS 2018

SUBJECT AREA: Structural Dynamics	DATE: June 25. 2018	NO. OF PAGES: 166

TITLE:

Dynamic Identification and Numerical Modelling of a Pantograph

BY:

John-Arne Berg Sivertsen
Anders Nygaard Knutzen

SUMMARY:
The main objective of this thesis is to measure and determine the dynamic properties of a measurement pantograph, and then create a numerical model with the same properties. The purpose of the model is to give a better representation of the actual behavior of the pantograph compared to the previously used lumped mass models. The thesis presents the process from very simple operation of the pantograph and contact force measurements, to more advanced studies of the attachment of the accelerometers and the development of test setups and procedures to measure the dynamic properties. The measurements done on the dynamic properties are then analyzed using scripts in MATLAB and the modal analysis software ARTeMIS.

Using the results from the dynamic analysis, a numerical 3D model is created in Abaqus CAE with the same dynamic behavior as the pantograph in the lab.

RESPONSIBLE TEACHER: Professor Nils Erik Anders Rønnquist

SUPERVISOR(S) Nils Erik Anders Rønnquist, Petter Røe Nåvik and Stefano Derosa

CARRIED OUT AT: Department of Structural Engineering NTNU

Preface

This is the master thesis completing a M.Sc. Degree at the Department of Structural Engineering at NTNU. The thesis is a result of the work of John-Arne Berg Sivertsen and Anders Nygaard Knutzen. The thesis was written during the spring of 2018.

We would like to thank Professor Anders Rønnquist, Postdoctrual resaercher Petter Røe Nåvik and PhD Candidate Stefano Derosa for their guidance in this thesis.

We would also like to thank Ragnar Moen, Terje Petersen and Christian Frugone for helping us in the lab.

John-Arne Berg Sivertsen
June 25. 2018

Anders Nygaard Knutzen
June 25. 2018

Abstract

The main objective of this thesis is to measure and determine the dynamic properties of a measurement pantograph, and then create a numerical model with the same properties. The purpose of the model is to give a better representation of the actual behavior of the pantograph compared to the previously used lumped mass models. The thesis presents the process from very simple operation of the pantograph and contact force measurements, to more advanced studies of the attachment of the accelerometers and the development of test setups and procedures to measure the dynamic properties. The measurements done on the dynamic properties are then analyzed using scripts in MATLAB and the modal analysis software ARTeMIS.

Using the results from the dynamic analysis, a numerical 3D model is created in Abaqus CAE with the same dynamic behavior as the pantograph in the lab.

Sammendrag

Hovedmålet i denne avhandlingen er å måle og bestemme de dynamiske egenskapene til en målepantograf, for deretter å konstruere en numerisk modell med de samme egenskapene. Hensikten med modellen er at den skal kunne gi en bedre representasjon av den faktiske oppførselen til pantografen enn det "lumped mass" modellene gir. Oppgaven tar for seg prosessen fra veldig enkel operasjon av pantografen og kontaktkraftmåling til å se på innfesting av akselerometre, og videre til utviklingen av testoppsett og metoder for å måle de dynamiske egenskapene. Målingene blir så analysert ved hjelp av skrip i MATLAB og analyseprogramvaren ARTeMIS.

Ved bruk av resultatene av de dynamiske analysene er en numerisk 3D modell konstruert i Abaqus CAE med den samme dynamiske oppførselen.

Table of Contents

List of Figures

List of Tables

1 — Introduction

This report presents the results of a study of a train pantograph used for measurement of the catenary system delivering power to operation of electric trains. Following is a presentation of the motivation behind the study and description of the scope of this report and the studies performed.

1.1 Motivation

In today's society railway vehicles with electrical traction are one of the most economical, environmentally friendly and safe means of transportation [Ambrósio et al., 2012]. To be able to compete with planes, the railroad is required to transport people over long distances in a relatively short period of time. This requires the trains to operate at high speeds, and with the high speeds comes the obstacle of delivering enough power to the train.

At these high speeds, the interaction between the catenary system and the pantograph introduces high-frequency contributions that need to be analyzed. If the contact is lost between the catenary and the pantograph, there will be a momentary loss of power to the motors, and arching will occur. Arching between the pantograph head and the contact wire causes additional wear and tear. The arching also causes distortions in the waveform of the voltage and current and generates transients on the railroad system interfering with other trains and transformers on the line [Midya et al., 2009]. Increasing the contact force between the pantograph and the contact wire would improve the contact and the energy transfer, but would result in increased tear of the contact wire and collector strip. This is not a viable solution due to the required reliability of operation and preferred long service spans. The solution is then to keep the contact force low and study the dynamics of the interaction.

The pantograph models currently used in simulations of the catenary-pantograph interaction are lumped mass models rendering limited dynamic modes. Most of these models only contain the opportunity for vertical motion. The lumped mass models also require to run the simulation using two parallel models, where the results from the catenary model at specific time increments are the input of the lumped mass model of the pantograph, before returning new input to the catenary model. This makes the running procedure quite complicated even though the pantograph model itself is simple. A solution to improve the simulations is to create a numerical model of the pantograph. This is the motivation of the studies performed in this thesis.

1.2 Scope of the study and this final report

The focus of this thesis has been to identify the dynamic properties of a pantograph, to create a numerical dynamic model of the pantograph. To achieve this, a lab procedure was developed, case-specific studies of the dynamic properties of the pantograph was performed and validation of the laboratory approach have been performed. Followed by a modal analysis of the pantograph, and subsequently the creation of a numerical model.

The theory behind the methods used is presented in two chapters. The first theory chapter focuses on numerical calculation of dynamic models and the second focuses on the signal processing applied during this study. The theory has been used in practical implementation to study the dynamics of the pantograph, and has only been evaluated in relation to its practical implementation.

As part of this study was to create a laboratory procedure to study the pantograph, the measuring equipment used are presented followed by a short description of the pantograph system. Further, the operation of the pantograph has been shortly studied and an investigation of the static behavior of the pantographs in the operational height domain was performed.

Preliminary observations lead to the belief that the sensor attachment should be evaluated. Therefore, a subordinate study of sensor behavior with and without support was conducted.

After the initial studies of the stationary behaviour, and measurement equipment was conducted, a laboratory procure was established. Then the dynamic properties of the pantograph were measured, and case specific studies and a modal analysis was performed on the measurement data. Finally, a numerical model of the pantograph has been created and tweaked to match some of the dynamic properties found in the pantograph. This report is structured such that it largely follows the order of presentation in this section.

1.3 Objectives of this Thesis

The objective of this master thesis is to describe the dynamic behavior of a train pantograph and create a numerical multibody dynamic model that reproduces the behavior observed in experimental data. To reach this objective, four sub-objectives have been defined:

- Understand how the pantograph works, and how it is operated.
- Develop a laboratory procedure capable of identifying the dynamic behavior in the pantograph.
- Measure the response of the pantograph in the lab, and analyze and determine its the dynamic behavior.
- Create a numerical model of the pantograph in Abaqus that reproduces the dynamic behavior observed in the experimental data

Understanding how to pantograph works, and how it is operated is important to be able to determine proper testing conditions. That is, what contact force and what operational height should be used. This understanding should influence the development of the laboratory procedure, to assure that the further analysis is assessing response in the desired operating conditions. The numerical model should be able to both run dynamic analysis and to assist as a reference in the further experimental analysis of the physical pantograph.

2 — Theory of dynamics

This chapter will start by presenting the theory of a single degree of freedom (SDOF) system, followed by the theory of a multi-degree of freedom (MDOF) system and natural frequencies of beams in bending.

2.1 Single degree of freedom system

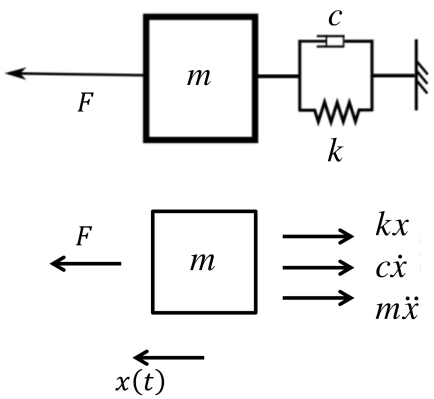

Figure 2.1: Mass, spring, damper system

Summing up the forces acting on the mass yields the equation

$$m\ddot{x}(t) + c\dot{x}(t) + kx(t) = F(t) \tag{2.1}$$

where m is the mass of the wagon, k is the spring stiffness, and c is the damping coefficient. $\ddot{x}(t)$, $\dot{x}(t)$, and $x(t)$ are the acceleration, velocity and the displacement from the equilibrium position. The total solution consists of two components: one complementary solution and one particular. The complementary can be obtained by solving the homogeneous version of equation 2.1 with $F(t) = 0$.

$$m\ddot{x}(t) + c\dot{x}(t) + kx(t) = 0 \tag{2.2}$$

By using the method of pre-manufactured solutions and substituting $x(t) = Xe^{\lambda t}$, the equation can be written as.

$$\lambda^2 + \frac{c}{m}\lambda + \frac{k}{m} = 0 \tag{2.3}$$

with the non-trivial solution:

$$\lambda = -\frac{c}{2m} \pm \sqrt{\left(\frac{c}{2m}\right)^2 - \frac{k}{m}} \tag{2.4}$$

Introducing the definitions of the natural frequency ω_n, critical damping constant c_{cr}, and damping ratio ξ.

$$\omega_n = \sqrt{\frac{k}{m}}\,, \qquad c_{cr} = 2m\omega_n\,, \qquad \xi = \frac{c}{c_{cr}} \tag{2.5}$$

The variables c, m, and k can be substituted with ω_n and ξ, expressing λ as follows:

$$\lambda = -\xi\omega_n \pm \omega_n\sqrt{\xi^2 - 1} \tag{2.6}$$

The general solution for the system is on the form

$$x_c(t) = X_1 e^{\lambda_1 t} + X_2 e^{\lambda_2 t} \tag{2.7}$$

With λ determined by the system characteristics by equation 2.6. The constants X_1 and X_2 are determined by the initial conditions for the system

$$\begin{aligned} X_1 + X_2 &= x_0 \\ \lambda_1 X_1 + \lambda_2 X_2 &= \dot{x}_0 = v_0 \end{aligned} \tag{2.8}$$

Rewriting the equations yield the general terms for the constants X_1 and X_2

$$X_1 = -\frac{\lambda_2 x_0 - v_0}{\lambda_1 - \lambda_2} \qquad X_2 = \frac{\lambda_1 x_0 - v_0}{\lambda_1 - \lambda_2} \tag{2.9}$$

And finally combined to the general solution for the system

$$x_c(t) = -\frac{\lambda_2 x_0 - v_0}{\lambda_1 - \lambda_2} e^{\lambda_1 t} + \frac{\lambda_1 x_0 - v_0}{\lambda_1 - \lambda_2} e^{\lambda_2 t} \tag{2.10}$$

Using the expression for λ obtained from 2.6 in the general solution 2.10 three simplified equations can be obtained.

$$x_c(t) = \begin{cases} e^{-\xi\omega_0 t}[A \cdot cos(\omega_d t) + B \cdot sin(\omega_d t)], & for\ \xi < 1 \\ e^{-\omega_0 t}[A + B \cdot t], & for \xi = 1 \\ e^{-\xi\omega_0 t}[A \cdot cosh(\overline{\omega} t) + B \cdot sinh(\overline{\omega} t)], & for\ \xi > 1 \end{cases} \tag{2.11}$$

Where $\omega_d = \omega_n \sqrt{1 - \xi^2}$, and $\overline{\omega} = \omega_n \sqrt{\xi^2 - 1}$.

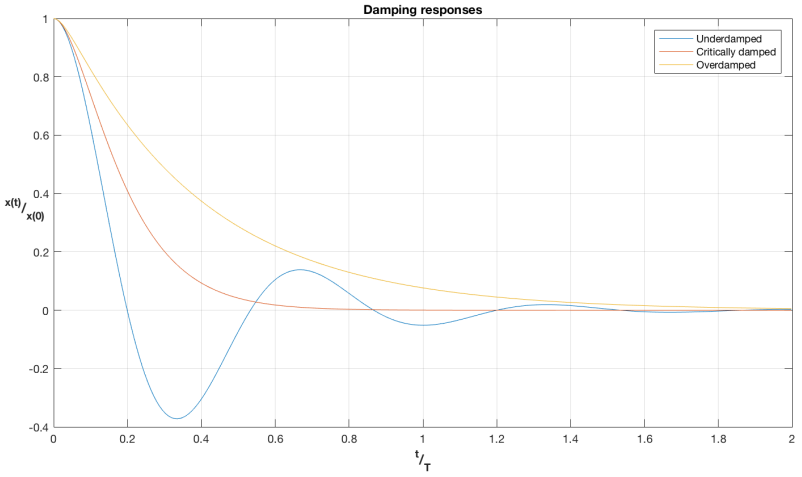

Figure 2.2: Characteristic system response.

The three characteristic solutions depends on the damping value of ξ. The first equation is with a damping less than the critical damping, $\xi < 1$. The solution for λ will then result in two complex values, and the response is described as underdamped. If the damping is

equal to the critical damping, $\xi = 1$, the root component equals zero, and λ will be a real number. This response is known as critically damped. The last response of the system is with a damping higher than the critical one, resulting in a slower response as the angular frequency increases and the solution has real valued roots. From Figure 2.2 it can be seen that the critical damped systems comes to rest first. The overdamped system has the similar properties as the critical system but the response is much slower. The underdamped systems will oscillate around the equilibrium position before it comes to rest.

The particular solution of equation will be dependent on the load acting on the system. Here a harmonic force with an amplitude F_0, phase $\theta = 0$ and natural frequency Ω is used.

$$F(t) = F_0 \, cos(\Omega t) = F_0 \, Re\{e^{i\Omega t}\} \tag{2.12}$$

The response of the system will have the same frequency as the force and the amplitude of the response will vary based on the relationship between the systems natural frequency and the frequency of the force. This ratio is expressed by β,

$$\beta = \frac{\Omega}{\omega_n} \tag{2.13}$$

Using the expression for β and ξ, equation 2.1 can be rewritten as

$$\begin{aligned} (\, -\Omega^2 m + i\Omega c + k \,)\, X_p e^{i\Omega t} &= F_0 e^{i\Omega t} \\ (\, (1-\beta^2) + i2\beta\xi \,)\, k X_p &= F_0 \\ X_p &= \frac{F_0}{k \,(\, (1-\beta^2) + i2\beta\xi \,)} \end{aligned} \tag{2.14}$$

By dividing the response amplitude X_p by the amplitude of the force F_0, the modulus of the frequency response function can be obtained.

$$|H(\Omega)| = \frac{1}{k\sqrt{(1-\beta^2)^2 + (2\xi\beta)^2}} \tag{2.15}$$

The phase angle between the force and the response is then calculated by the ratio between the imaginary and the real part

$$\angle H(\Omega) = \arctan\Big(-\frac{2\xi\beta}{1-\beta^2} \Big) \tag{2.16}$$

If the damping is null, and the frequency ratio is equal to one, i.e $\xi = 0$ and $\beta = 1$, the modulus of the response diverges to infinity. The drastic increase of the response at a given load frequency is known as resonance, and the frequency it occurs at defines the systems resonance frequency. The resonance frequency of a system differs from the natural frequency depending on the amount of damping in the system. If there is none, the two are the same and a damping of 20% results in a resonance frequency of 96% of the natural one. So for structures and systems with relative small damping the shift in resonance is relatively small.

The particular solution is then expressed by the frequency response function, amplitude of the force and the phase angle as follows:

$$\begin{aligned} x_p(t) &= Re\Big\{|H(\Omega)||F_0|e^{i(\Omega t+\varphi)}\Big\} \\ x_p(t) &= X\cos(\Omega t+q) \\ X &= |H(\Omega)||F_0|, \quad q = \angle H(\Omega) \end{aligned} \tag{2.17}$$

The final solution is then the two parts combined

$$\begin{aligned} x(t) =& x_c(t) + x_p(t) \\ x(t) =& X_1 e^{\lambda_1 t} + X_2 e^{\lambda_2 t} + X\cos(\Omega t+q) \end{aligned} \tag{2.18}$$

2.1.1 Non-viscous damping

Non-viscous damping can be categorized as follows: hysteretic, Coulomb and radiation damping. These are used to describe the loss of energy out of the system. Radiation damping is associated with the loss of energy out of the boundary for the system. For instance, the loss of energy in the pantograph due to interaction with the roof of the train through the fixtures. Coulomb damping is associated with dry friction, such as friction in the joints of the pantograph, and the sliding contact of the pantograph head and the contact wire. Hysteretic damping is associated with the energy loss due to internal friction in the material due to the repetitive internal deformation and restoration to the original shape. This energy is consequently dissipated into the crystal lattice as random vibrations.

Of the different types of physical damping, only the viscous damping is easy to represent by dynamic equations. And according to [Cook et al., 2002, p.388-390] most damping in structures are low and can be presented as viscous damping without any large errors. In the pantograph system this is mostly the case and the large dampers used in the system are possible to idealize as viscous dampers.

2.2 Multiple degrees of freedom

When analyzing more complex systems than the SDOF system it is required to describe the behaviour of multiple bodies and/or behaviour along one body. For simple multi-degree of freedom systems the dofs can be mapped to a minimum by defining the Jacobian matrix for the system to transform from the local dofs to the global ones. As the system complexity increases this approach is too time consuming and the use of FEM software is beneficial.

2.2.1 Equation of motion for Finite element models

Reference for theory : [Cook et al., 2002, p. 374-377]. To be able to perform numerical calculations on a physical object it is required to discretize the object into a finite set of elements. Each of these elements have a displacement field $\{\boldsymbol{u}\}$, which is described by a set of nodal dofs $\{\boldsymbol{d}\}$, and the interpolation functions $[\boldsymbol{N}]$.

$$\{\boldsymbol{u}\} = [\boldsymbol{N}]\{\boldsymbol{d}\} \tag{2.19}$$

The equation of motion for a FEM model can be derived through the principle of virtual work. For each element in the model the work done by the externally applied loads must be equal to the internal energy in form of inertia, dissipation of energy, and internal stresses in the element. To be able to describe these, the displacement and strain field must be defined.

The strain field of the element is obtained by the partial derivative of the displacement field. The operator $\boldsymbol{\partial}$ represents the partial derivative on matrix form.

$$\{\boldsymbol{\epsilon}\} = \boldsymbol{\partial}\{\boldsymbol{u}\} = \boldsymbol{\partial}[\boldsymbol{N}]\{\boldsymbol{d}\} = [\boldsymbol{B}]\{\boldsymbol{d}\} \tag{2.20}$$

Where $[\boldsymbol{B}]$ is known as the strain-displacement matrix. And the matrix $[\boldsymbol{E}]$ expresses the relationship of the stress-field $\{\boldsymbol{\sigma}\}$ and the strain-field $\{\boldsymbol{\epsilon}\}$,

$$\{\boldsymbol{\sigma}\} = [\boldsymbol{E}]\{\boldsymbol{\epsilon}\} \tag{2.21}$$

The external work acting on an element is summed up by:

$$\delta W_e = \int_V \{\delta\boldsymbol{u}\}\{\boldsymbol{F}\}dV + \int_S \{\delta\boldsymbol{u}\}^T\{\boldsymbol{\Phi}\}dS + \sum_{i=1}^{n}\{\delta\boldsymbol{u}\}_i^T\{\boldsymbol{p}\}_i \tag{2.22}$$

Where V is the volume of the element with the forces $\{\boldsymbol{F}\}$ working on the element. S is the surface of the element, with the traction forces $\{\boldsymbol{\Phi}\}$ acting on it. $\{\boldsymbol{p}\}_i$ represents the prescribed concentrated loads and the the corresponding virtual displacement at the loads is defined by $\{\delta\boldsymbol{u}\}_i$ for the n nodes.

The internal virtual work of the element is defined as.

$$\delta W_i = \int_V \Big(\{\delta\boldsymbol{u}\}^T\rho\{\ddot{\boldsymbol{u}}\} + \{\delta\boldsymbol{u}\}^T c\{\dot{\boldsymbol{u}}\} + \{\delta\boldsymbol{\epsilon}\}^T\{\boldsymbol{\sigma}\}\Big)dV \tag{2.23}$$

ρ represents the mass density, and c is the viscous damping parameter. $\{\delta\boldsymbol{u}\}$ represents the virtual displacements and $\{\delta\boldsymbol{\epsilon}\}$ is the corresponding virtual strains.

Introducing the terms for nodal velocity and acceleration,

$$\{\dot{u}\} = \boldsymbol{N}\{\dot{d}\} \tag{2.24}$$

$$\{\ddot{u}\} = \boldsymbol{N}\{\ddot{d}\} \tag{2.25}$$

combined with the expression previously represented for the strains $\{\boldsymbol{\epsilon}\}$, and nodal displacement $\{\boldsymbol{u}\}$ the expression for the virtual work can be rewritten as follows. Note, here the two terms for virtual work are combined, $\delta W_i - \delta W_e = 0$.

$$\begin{aligned}\{\delta\boldsymbol{d}\}^T\Bigg[\int_V \rho[\boldsymbol{N}]^T[\boldsymbol{N}]dV\{\ddot{\boldsymbol{d}}\} + \int_V c[\boldsymbol{N}]^T[\boldsymbol{N}]dV\{\dot{\boldsymbol{d}}\} + \int_V [\boldsymbol{B}]^T\{\boldsymbol{\sigma}\}dV \\ - \int_V [\boldsymbol{N}]^T\{\boldsymbol{F}\}dV - \int_S [\boldsymbol{N}]^T\{\boldsymbol{\Phi}\}dS - \sum_{i=1}^{n}\{\boldsymbol{p}\}_i\Bigg] = 0\end{aligned} \tag{2.26}$$

The two first terms in 2.26 is recognized as the the consistent mass and damping matrices for the element.

$$[\boldsymbol{m}] = \int_V \rho[\boldsymbol{N}]^T[\boldsymbol{N}]dV \tag{2.27}$$

$$[\boldsymbol{c}] = \int_V c[\boldsymbol{N}]^T[\boldsymbol{N}]dV \tag{2.28}$$

The next term in 2.26 is associated with the energy stored in the element due to forces and moments.

$$\{\boldsymbol{r}^{int}\} = \int_V [\boldsymbol{B}]^T\{\boldsymbol{\sigma}\}dV \tag{2.29}$$

If the material is linearly elastic the expression can be rewritten to the more known form of $\{\boldsymbol{r}^{int}\} = [\boldsymbol{k}]\{\boldsymbol{d}\}$, and the external forces acting on the element can be summed up to one term.

$$\{\boldsymbol{r}^{ext}\} = \int_V [\boldsymbol{N}]^T\{\boldsymbol{F}\}dV + \int_S [\boldsymbol{N}]^T\{\boldsymbol{\Phi}\}dS + \sum_{i=1}^{n}\{\boldsymbol{p}\}_i \tag{2.30}$$

The final dynamic equation for the element can then be written in matrice form similar to the SDOF system.

$$[\boldsymbol{m}]\{\ddot{\boldsymbol{d}}\} + [\boldsymbol{c}]\{\dot{\boldsymbol{d}}\} + [\boldsymbol{k}]\{\boldsymbol{d}\} = \{\boldsymbol{r}^{ext}\} \tag{2.31}$$

For the system consisting of multiple bodies and these again consisting of multiple elements it is necessary to link the element dofs to the global ones. The mapping of element i, to the global system is performed by matrix $\boldsymbol{a}_i$. Where $\{\boldsymbol{D}\}$ is the global dofs.

$$\{\boldsymbol{d}_i\} = [\boldsymbol{a}_j]\{\boldsymbol{D}\} \tag{2.32}$$

As a result, the transformation and summation of the elements to the global system the new global mass, damping and stiffness matrices is defined as.

$$[\boldsymbol{M}] = \sum_{i=1}^{n}\{\boldsymbol{a}\}_i^T[\boldsymbol{m}_i]\{\boldsymbol{a}\}_i = \sum_{i=1}^{n}\{\boldsymbol{a}\}_i^T\int_{V_i}\rho[\boldsymbol{N}]^T[\boldsymbol{N}]dV\{\boldsymbol{a}\}_i \tag{2.33}$$

$$[\boldsymbol{C}] = \sum_{i=1}^{n}\{\boldsymbol{a}\}_i^T[\boldsymbol{c}_i]\{\boldsymbol{a}\}_i = \sum_{i=1}^{n}\{\boldsymbol{a}\}_i^T\int_{V_i}c[\boldsymbol{N}]^T[\boldsymbol{N}]dV\{\boldsymbol{a}\}_i \tag{2.34}$$

$$[\boldsymbol{K}] = \sum_{i=1}^{n}\{\boldsymbol{a}\}_i^T[\boldsymbol{k}_i]\{\boldsymbol{a}\}_i = \sum_{i=1}^{n}\{\boldsymbol{a}\}_i^T\int_{V_i}[\boldsymbol{B}]^T\{\boldsymbol{\sigma}\}dV\{\boldsymbol{a}\}_i \tag{2.35}$$

And following the load matrix.

$$\begin{aligned}\{\boldsymbol{R}^{ext}\} &= \sum_{i=1}^{n}\{\boldsymbol{a}\}_i^T\{\boldsymbol{r}^{ext}\}_i \\ &= \sum_{i=1}^{n}\{\boldsymbol{a}\}_i^T\left[\int_{V_i}[\boldsymbol{N}]^T\{\boldsymbol{F}\}dV + \int_{S_i}[\boldsymbol{N}]^T\{\boldsymbol{\Phi}\}dS + \sum_{i=1}^{n}\{\boldsymbol{p}\}_i\right]\end{aligned} \tag{2.36}$$

The final equation of motion for the system then yields.

$$[\boldsymbol{M}]\{\ddot{\boldsymbol{D}}\} + [\boldsymbol{C}]\{\dot{\boldsymbol{D}}\} + [\boldsymbol{K}]\{\boldsymbol{D}\} = \{\boldsymbol{R}^{ext}\} \tag{2.37}$$

2.2.2 Mass and stiffness matrices

Using the interpolation functions to define the mass matrix results in a consistent mass matrix where the mass is weighted according the the element's interpolation function. The resulting mass matrix is real, which makes the complex conjugate of the matrix equal to the matrix itself, $[\bar{\boldsymbol{M}}] = [\boldsymbol{M}]$. The matrix is furthermore symmetric, resulting in the transposed matrix being equal to the matrix itself, $[\boldsymbol{M}]^T = [\boldsymbol{M}]$, and it's positive definite. For any real non-trivial $\{\boldsymbol{x}\}$, $\{\boldsymbol{x}\}^T[\boldsymbol{M}]\{\boldsymbol{x}\} \geq 0$.

The elements used in Abaqus are B31 elements, i.e. linear 3D beam elements with particle mass lumping. Particle mass lumping involves the mass is lumped to the nodes of the element without the weighting of the interpolation functions. The resulting mass matrix is diagonal and known as the lumped mass matrix. The matrix is real and symmetric due to only diagonal terms. For plate and beam elements the inertia connected to the rotation degrees of freedom are often neglected. As a result the lumped mass matrix is only positive semi-definite. For the B31 element in Abaqus, the inertia is lumped in the same manner as the mass in the translation degrees of freedom as default.

With any linear hyperelastic material, the constitutive matrix, $[\boldsymbol{E}]$ is real and symmetric. In the analysis performed in Abaqus any hysteric effects in the material is neglected and it's defined as ideally elastic, thus the stiffness matrix is real and symmetric. With the assumption of a real and positive definite constitutive matrix $[\boldsymbol{E}]$, the work that goes into deforming a body has to be positive, $W = 1/2\int_V\{\boldsymbol{\epsilon}\}^T[\boldsymbol{E}]\{\boldsymbol{\epsilon}\}dV > 0$. As a result, the stiffness matrix $\boldsymbol{K}$ is positive definite except for structures where rigid body modes are possible. This is very much the case in the Abaqus model where multiple bodies are connected and rigid body modes can occur. If $\{\boldsymbol{x}\}$ is a rigid body motion, there will be no internal forces in the element, thus $[\boldsymbol{K}]\{\boldsymbol{x}\} = \boldsymbol{0}$. The points above shows that the mass and stiffness matrices are real, symmetric and only positive definite.

2.2.3 The eigenvalue problem

To solve the problem the displacement and acceleration have to be connected to frequency. This is done by expressing the vibration motion by a vector $\{\bar{\boldsymbol{D}}\}$, that consists of the nodal amplitudes varying periodic with a sinusoidal shape. The displacement and acceleration vectors can therefore be expressed as.

$$\{\boldsymbol{D}\} = \{\bar{\boldsymbol{D}}\}\sin(\omega t) \tag{2.38}$$

$$\{\ddot{\boldsymbol{D}}\} = -\omega^2\{\bar{\boldsymbol{D}}\}\sin(\omega t) \tag{2.39}$$

The undamped, free vibration solution of equation 2.37, i.e. with $\{\boldsymbol{R}^{ext}\} = 0$ and $[\boldsymbol{C}] = 0$ with the displacement and acceleration expressed by 2.38 and 2.39 can be written as follows.

$$\Big([\boldsymbol{K}] - \omega^2[\boldsymbol{M}]\Big)\{\bar{\boldsymbol{D}}\} = \{\boldsymbol{0}\} \tag{2.40}$$

Where ω^2 is the eigenvalue and ω is a natural frequency of the system. The matrix $[\boldsymbol{K}] - \omega^2[\boldsymbol{M}]$ is called the dynamic stiffness matrix. The physical interpretation of the matrix is that the frequency controls the balance between the inertia loads to the elastic resistance. This is the problem solved by the linear perturbation analysis in Abaqus. The damping is neglected, and the natural frequencies of the system are found. Further theory of the eigenvalue problem will not be presented, and can be read in [Singiresu, 2011, p. 583-585].

2.3 Natural frequencies of beams

For beams in bending the equation of motion is.

$$EI\frac{\partial^4 w(\xi,t)}{\partial \xi^4} = -\rho A\frac{\partial^2 w(\xi,t)}{\partial t^2} \tag{2.41}$$

by substituting $w(\xi,t) = \psi(\xi)G(t)$, dividing the solution into one time dependent and one space dependent part the equation can be rewritten as follows.

$$\begin{aligned} EI\psi^{(4)}(\xi)G(t) &= -\rho A\psi(\xi)\ddot{G}(t) \\ \frac{\ddot{G}(t)}{G(t)} &= -\frac{EI}{\rho A}\frac{\psi"(\xi)}{\psi(\xi)} \end{aligned} \tag{2.42}$$

For the solution to be stable the time dependent term has to be singular for the natural frequency of the beam.

$$\begin{aligned} \ddot{G}(t) + \omega^2 G(t) &= 0 \\ \frac{\ddot{G}(t)}{G(t)} &= -\omega^2 \end{aligned} \tag{2.43}$$

By substitution the relationship to the natural frequency of the system can be introduced.

$$\begin{aligned} -\frac{EI}{\rho A}\frac{\psi^{(4)}(\xi)}{\psi(\xi)} &= -\omega^2 \\ \psi^{(4)} - \frac{\omega^2\rho A}{EI}\psi(\xi) &= 0 \end{aligned} \tag{2.44}$$

By substituting,

$$\gamma^4 = \frac{\omega^2 \rho A}{EI} \tag{2.45}$$

$$\psi(\xi) = Fe^{\delta\xi} \tag{2.46}$$

$$\psi^{(4)}(\xi) = \delta^4 Fe^{\delta\xi} \tag{2.47}$$

the equation of motion can be rewritten,

$$(\delta^4 - \gamma^4)Fe^{\gamma\xi} = 0 \tag{2.48}$$

The sum of the non-trivial solution of equation 2.48 gives the expression for the deflection of the beam,

$$\begin{aligned} w(\xi, t) = &\Big[F_1 \cosh(\gamma\xi) + F_2 \sinh(\gamma\xi) + F_3 \cos(\gamma\xi) + F_4 \sin(\gamma\xi)\Big] \\ &\cdot \Big[A \cos(\omega t) + B \sin(\omega t)\Big] \end{aligned} \tag{2.49}$$

By imposing the boundary conditions for a simply supported beam, the relation of a singular system matrix and the shape form γ can be obtained from the requirement of $\sin(\gamma L) = 0$.

$$\gamma_n = \frac{n\pi}{L} \tag{2.50}$$

Thus the natural frequencies of a simply supported beam is expressed as,

$$\omega_n = \left(\frac{n\pi}{L}\right)^2 \sqrt{\frac{EI}{\rho A}} \tag{2.51}$$

This expression will be used as a guidance for where the modes of beam elements in the pantograph is expected to be found in the spectrums. If one resonance frequency and it's corresponding shape are found, this gives an idea for where the next will be.

3 — Theory signal processing

3.1 System Response Spectrum

The response of a system caused by an external excitation can be written as the sum of the systems frequency response function and the force frequency content [Newland, 2012, p. 71-73].

$$R(\omega) = H(\omega)F(\omega) \tag{3.1}$$

where $R(\omega)$ is the total system response spectre due to an external load $F(\omega)$ and the systems response function $H(\omega)$. In the following equations $H(\omega)^*$ is the complex conjugate of $H(\omega)$, same goes for $F(\omega)$. And by the definition of the spectral density.

$$S_{RR} = \frac{R(\omega)R(\omega)*}{\Delta\omega} \tag{3.2}$$

where $\Delta\omega = 2\pi/T$ with $T \to \infty$.

$$S_{RR} = H(\omega)H(\omega)^* \frac{F(\omega)F(\omega)^*}{\Delta\omega} = |H(\omega)|^2 S_{FF} \tag{3.3}$$

As a result it is possible to estimate the systems frequency response function, FRF, from the spectral density of the response of the system when the force spectrum is known.

3.2 General Spectral Density

The Spectral Density of a response gives information about the frequency content in the response. The spectral density of periodic functions can easily be obtained by the Fourier-transform, but since the response of functions is not ideal periodic functions the method can not be directly applied. To overcome this, the autocorrelation function is used as input to the Fourier-transform instead. The autocorrelation function goes to 0 as $\tau \to \infty$ for a random process. This makes the requirement to use Fourier valid [Newland, 2012, p. 41].

$$\int_{-\infty}^{\infty} |R_x(\tau)| d\tau < \infty \tag{3.4}$$

To obtain the frequency spectre of the process we use the Fourier on the autocorrelation function. The Power Spectral Density of a process, $x(t)$ is therefore defined as;

$$S_x(\omega) = \frac{1}{2\pi} \int_{-\infty}^{\infty} R_x(\tau) e^{-i\omega t} d\tau \tag{3.5}$$

3.3 Auto- and crosscorrelation

For a random process $x(t)$, the autocorrelation function is defined as the average value of the product $x(t)x(t+\tau)$. This is done by sampling the value of x at time t, and then again at a time lag, τ later. The product of all these samples are then averaged over an ensemble of samples to average out errors in the series. The definition of the autocorrelation function is [Newland, 2012, p. 26].

$$R_x(\tau) = E[x(t)x(t+\tau)] \tag{3.6}$$

In a similar manner the crosscorrelation between the random process $x_1(t)$ and the random process $x_2(t+\tau)$, including a time lag τ, can be established [Newland, 2012, p. 29].

$$R_{x_1x_2}(\tau) = E[x_1(t)x_2(t+\tau)] \tag{3.7}$$

3.4 Discrete Fourier Transform

A periodic signal can be broken up into harmonic components by the use of the Fourier transform. The result is that the the signal is expressed as a infinite trigonometric series of the form view below. [Newland, 2012, p. 114]

$$x(t) = a_0 + \sum_{k=1}^{\infty}(a_k \cos\frac{2\pi kt}{T} + b_k \sin\frac{2\pi kt}{T}) \tag{3.8}$$

Where a_k and b_k is the coefficients of the real and imaginary component of harmonic component k defined as.

$$a_k = \frac{1}{T}\int_0^T x(t)\cos\frac{2\pi kt}{T}dt, \quad k \geq 0 \tag{3.9}$$

$$b_k = \frac{1}{T}\int_0^T x(t)\sin\frac{2\pi kt}{T}dt, \quad k \geq 1 \tag{3.10}$$

Rewriting this to complex notation, the real and imaginary part can be combined to one, and by the use the Euler notation for the harmonic components $\cos$ and $\sin$ the expression can be simplified.

$$X_k = a_k - ib_k \tag{3.11}$$

$$e^{-(2\pi kt/T)} = \cos\frac{2\pi kt}{T} - i\sin\frac{2\pi kt}{T} \tag{3.12}$$

$$X_k = \frac{1}{T}\int_0^T x(t)e^{-i(2\pi kt/T)}dt, \quad k \geq 0 \tag{3.13}$$

When using this on a discrete time series, the continuous function $x(t)$ is substituted by sampling value x_r which is the value at time $t = r\Delta$ where the sampling spacing is defined as $\Delta = T/N$. Rewriting the latter equation for a series yields;

$$X_k = \frac{1}{T}\sum_{r=0}^{N-1} x_r e^{-i(2\pi k/T)(r\Delta)}\Delta \tag{3.14}$$

Substituting for Δ and t gives the DFT;

$$X_k = \frac{1}{N}\sum_{r=0}^{N-1} x_r e^{-i(2\pi kr/N)} \tag{3.15}$$

For a continuous signal the DFT will not provide enough information to exactly replicate the signal, but for a discrete series it is able to exactly replicate the sample of the signal [Newland, 2012, p. 115]. The Fast-Fourier transform is an enhanced algorithmic version of the DFT and will be used on the data in Matlab.

3.5 The fast Fourier transform

The fast Fourier transform (FFT) is an algorithm used by computers for calculating the discrete Fourier transforms (DFT's). It's a more efficient algorithm to calculate the finite series expressed by 3.15. If the series was to be calculated by the direct approach it would require N multiplications for each of the N values of X_k, resulting in a total of N^2 operations. The FFT reduces this work to a number of operations of $N \cdot \log_2(N)$. If $N = 2^{16}$ the direct approach would require $O \approx 4.29 \cdot 10^9$ while the FFT would require $O \approx 1.05 \cdot 10^6$. That is less than 1/4000th of the required operations with the direct approach. The FFT is therefore extremely powerful when large data sets is to be analyzed. An added benefit of the FFT is that the computational errors caused by round-off errors due to limitations in number resolution (allocated bits per value) is reduced due to less operations.

The way the FFT works is by dividing the full sequence into smaller sequences. The FFT algorithm calculates the DFT of the individual series before combining them to form the full DFT for the whole series. The equations and algorithm can be found in [Newland, 2012, p.150-166].

3.6 Nyquist frequency

The Nyquist frequency is the highest frequency which can correctly be represented by a sampling with frequency f_{sample}. The Nyquist frequency is fundamental in the use of DFT because it limits the frequency range which can be analyzed. At higher frequencies the spectrum will show aliases of the true spectrum [Newland, 2012, p. 119].

$$f_{Nyquist} = \frac{1}{2 \cdot \Delta} = \frac{f_{sample}}{2} \tag{3.16}$$

Here, Δ is here the time spacing for the sampling in the data series.

3.7 Welch's Method

Welch's Method is a method to obtain the Power Spectral Density function of a process where the signal of the process is divided into N signals of equal length. By using the method some of the resolution in the PSD is traded off to average out noise in the series by using multiple series. This is done because the series obtained in real life measurements is not as perfect as in theory and noise and variations will occur.

3.8 Windowing

Since the FFT-algorithm sees the input signal as one period of a repeating signal, any discontinuities between the start and end value can introduce spectral leakage. An example is that the amplitude is large and positive at the start of the series, while in the end of the series the value is negative. This will be interpreted as a high frequency since the change is so rapid. This can often be higher than the Nyquist frequency and result in the energy leaking into all the other frequencies in the specter. This can be reduced by the use of a technique called windowing [Instruments, 2016, p. 9]. The way it works is that the samples in the series is multiplied with a periodic function with equal length of the signal series. These periodic functions have different properties depending on the application. E.g. the Hanning window is 0 at the start and end of the time series to eliminate frequency jumps in the series. This will reduce or eliminate any false frequencies introduced by cutting of the series. In the processing of the recordings, uniform and Hanning windowing will be used. The uniform window, also known as rectangular window, will be used for the impulse testing when the whole series is used with "N" Welch divisions are equal to one. When the series are divided into two or more, the Hanning window will be used to deal with the possible high frequency jumps. The Hanning window is chosen here when dealing with multiple divisions and sweeps since it's recommended for sine wave signal content as well as unknown content [Instruments, 2016, p. 15].

$$w(n) = \sin^2\left(\frac{\pi n}{N-1}\right) \tag{3.17}$$

Where n denotes the sample in the total series of N samples, or in this case discrete time. If the original sample values are given by $u(n)$, the values fed into the FFT-algorithm is;

$$u_n = u(n) \cdot w(n) \tag{3.18}$$

3.9 Peak-Picking Method

The Peak-Picking method is one of the simplest methods used to analyze the dynamic response of structures. The method is based on the result from the response spectrum of a system, shown by equation 3.3. The key point in the equation is that the response is closely connected to the systems FRF, and as the frequency approaches the systems natural frequencies the FRF will peak. The frequencies at where these peaks then occur are natural frequencies of the system and they are used to establish the response by finding the operational shapes.

3.10 Operational shape identification

To be able to predict the shape of the deformation at the frequencies found by the peak-picking method, the autocorrelation must be used. By using the relations for generalized coordinates;

$$r_1(t) = r(x_1, t) \approx \phi(x_1)\eta(t) \tag{3.19}$$

$$r_2(t) = r(x_2, t) \approx \phi(x_2)\eta(t) \tag{3.20}$$

and for the autocorrelation;

$$S_{r1r1}(\omega_k) \approx \phi(x_1)^2 S_{\eta\eta}(\omega_k) \tag{3.21}$$
$$S_{r2r2}(\omega_k) \approx \phi(x_2)^2 S_{\eta\eta}(\omega_k) \tag{3.22}$$
$$S_{r1r2}(\omega_k) \approx \phi(x_1)\phi(x_2) S_{\eta\eta}(\omega_k) \tag{3.23}$$

the mode shape can be established by comparing the real part of the autocorrelation spectrum of the different accelerometers. To do this the second accelerometer is chosen as reference, $\phi(x_2) \equiv 1$. The magnitude at point x_1, $\phi_k(x_1)$ can then be solved for by dividing $S_{r1r1}(\omega_k)$ by $S_{r2r2}(\omega_k)$.

$$\phi_k(x_1) = \sqrt{\frac{S_{r1r1}(\omega_k)}{S_{r2r2}(\omega_k)}} \tag{3.24}$$

By applying this along one member or on different members, it's possible to establish the relation between the accelerometers at a given frequency.

3.11 Frequency-Domain Decomposition (FDD)

The main idea behind the FDD methods is to decompose the response in the frequency domain using a singular value decomposition. Doing this results in spectral densities for the entire system with respect to the singular values instead of the individual nodal spectral densities. Then the entire system can be assessed based on its own spectral densities. The goal with this approach is to reduce required dimensions of the the vector space describing the system. In the following chapter the FDD approach is presented on the basis of [Brincker and Ventura, 2015, p. 266-272].

Considering the response $\{\boldsymbol{y}(t)\}$ of a system can be given as a combination of modal vectors multiplied be a corresponding set of modal responses for each mode shape, as described in equation (3.25).

$$\{\boldsymbol{y}(t)\} = \{\boldsymbol{a}_1\}q_1(t) + \{\boldsymbol{a}_2\}q_2(t) + ... = [\boldsymbol{A}]\{q(t)\}^T \tag{3.25}$$

This formulation renders the opportunity to generate a correlation function matrix for the response $[\boldsymbol{R}_y(\tau)]$ as in equation (3.26) and then expressing its relation to the correlation function for the modal coordinates $[\boldsymbol{R}_q(\tau)]$ as in equation (3.28)

$$[\boldsymbol{R}_y(\tau)] = E[\{\boldsymbol{y}(t)\}\{\boldsymbol{y}(t+\tau)\}^T] \tag{3.26}$$
$$= [\boldsymbol{A}]E[\{\boldsymbol{q}(t)\}\{\boldsymbol{q}(t+\tau)\}^T][\boldsymbol{A}]^T \tag{3.27}$$
$$= [\boldsymbol{A}][\boldsymbol{R}_q(\tau)][\boldsymbol{A}]^T \tag{3.28}$$

Taking the Fourier transform of equation (3.28) renders the spectral density matrix $[\boldsymbol{G}_y(f)]$ as shown in equation (3.29). Assuming that the modal coordinates are uncorrelated, implies that only the auto-correlations of $[\boldsymbol{R}_q(\tau)]$ are non-zero. This gives a modal spectral density function matrix $[\boldsymbol{G}_q(f)]$ that is diagonal and positive valued. In order to account

for the complexity in the mode shapes and in the spectral density function matrix, the Hermitian is used and not the transpose. The result is in equation (3.30).

$$[\boldsymbol{G}_y(f)] = [\boldsymbol{A}][\boldsymbol{G}_q(f)][\boldsymbol{A}]^T \tag{3.29}$$
$$= [\boldsymbol{A}][g_n^2(f)][\boldsymbol{A}]^H \tag{3.30}$$

By taking the singular value decomposition of the spectral density function matrix shown in equation (3.31), one arrives at a patented interpretation of the singular values $[s_n^2]$ as the auto spectral densities of the modal coordinates and the singular vectors in $[\boldsymbol{U}] = [\boldsymbol{u}_1, \boldsymbol{u}_2, \ldots]$ as the mode shapes. Patent is found in Rune Brincker [1999].

$$[\boldsymbol{G}_y(f)] = [\boldsymbol{U}][\boldsymbol{S}][\boldsymbol{U}]^H = [\boldsymbol{U}][s_n^2][\boldsymbol{U}]^H \tag{3.31}$$

$$[\boldsymbol{G}_y(\tau)] = [\boldsymbol{U}][\boldsymbol{S}][\boldsymbol{V}]^H \tag{3.32}$$

The approach used in equation (3.31) in only approximate. Because a singular value decomposition, even in its general form shown in equation (3.32), can not completely correspond to the theoretical decomposition of the spectral density matrix, shown in equation (3.33).

$$[\boldsymbol{G}_y(\omega)] = \sum_{n=1}^{N}\left(\frac{\{\boldsymbol{a}_n\}\{\boldsymbol{\gamma}_n\}^T}{-i\omega-\lambda_n} + \frac{\{\boldsymbol{a}_n^*\}\{\boldsymbol{\gamma}_n\}^H}{-i\omega-\lambda_n^*} + \frac{\{\boldsymbol{\gamma}_n\}\{\boldsymbol{a}_n^*\}^T}{-i\omega-\lambda_n} + \frac{\{\boldsymbol{\gamma}_n^*\}\{\boldsymbol{a}_n^*\}^H}{-i\omega-\lambda_n^*}\right) \tag{3.33}$$

Introducing the approximation of the modal participation vectors $\{\boldsymbol{\gamma}_n\}$ given in (3.34), based on the assumption of reasonably well separated modes.

$$\{\boldsymbol{\gamma}_n\} \cong c_n^2\{\boldsymbol{a}_n\} \tag{3.34}$$

Now utilizing this expression for $\{\boldsymbol{\gamma}_n\}$ and assuming a lightly damped system, then only the two middle terms remains in the decomposition as shown in (3.35).

$$[\boldsymbol{G}_y(\omega)] \cong \sum_{n=1}^{N}\left(\frac{c_n^2\{\boldsymbol{a}_n^*\}\{\boldsymbol{a}_n\}^H}{-i\omega-\lambda_n^*} + \frac{c_n^2\{\boldsymbol{a}_n^*\}\{\boldsymbol{a}_n\}^T}{-i\omega-\lambda_n}\right) \tag{3.35}$$
$$\cong \sum_{n=1}^{N} 2c_n^2 Re\left(\frac{\{\boldsymbol{a}_n^*\}\{\boldsymbol{a}_n\}^T}{-i\omega-\lambda_n}\right) \tag{3.36}$$

Assuming general complex mode shapes and uncorrelated modal coordinates the spectral density matrix for a modal decomposition is given in (3.37).

$$[\boldsymbol{G}_y(\omega)] = [\boldsymbol{A}][Q_n(-\omega)Q_n(\omega)][\boldsymbol{A}]^T + [\boldsymbol{A}][Q_n(-\omega)Q_n^*(\omega)][\boldsymbol{A}]^H \tag{3.37}$$
$$+ [\boldsymbol{A}^*][Q_n^*(-\omega)Q_n(\omega)][\boldsymbol{A}]^T + [\boldsymbol{A}^*][Q_n(-\omega)^*Q_n(\omega)^*][\boldsymbol{A}]^H \tag{3.38}$$

The same assumption of a diagonal modal spectral density function matrix results in the expression below.

$$[\boldsymbol{G}_y(\omega)] \cong \sum_{n=1}^{N} \left(\frac{(g_{1n}\{\boldsymbol{a}_n\} + g_{3n}\{\boldsymbol{a}_n^*\})\{\boldsymbol{a}_n\}^T}{i\omega - \lambda_n} + \frac{(g_{2n}\{\boldsymbol{a}_n\} + g_{4n}\{\boldsymbol{a}_n^*\})\{\boldsymbol{a}_n\}^H}{-i\omega - \lambda_n^*} \right) \quad (3.39)$$

Under the assumption of well separated modes or uncorrelated modal coordinates the above expression is a reasonable approximate decomposition of the spectral density matrix. However, the complexity in the modes are largely affected by the two ignored terms, and one should therefor be careful when evaluating the physical interpretation of the complexity.

The computational approach to estimate mode shapes in the FDD analysis is shown below.

$$[\boldsymbol{G}_y(f)] = [\{\boldsymbol{u}_1\}, \{\boldsymbol{u}_2\}] \begin{bmatrix} s_1^2 & 0 \\ 0 & s_2^s \end{bmatrix} \begin{bmatrix} \{\boldsymbol{u}_1^H\} \\ \{\boldsymbol{u}_2^H\} \end{bmatrix} \quad = s_1^2 \{\boldsymbol{u}_1\}\{\boldsymbol{u}_1 + s_1^2\}\{\boldsymbol{u}_2\}\{\boldsymbol{u}_2\} \quad (3.40)$$

In the Extended FDD the modal spectral densities are calculated, before being transformed back to the time domain. Then the damping properties of the modes are calculated by curve fitting of a logarithmic damping.

3.12 Stochastic Subspace Identification (SSI)

Stocastic subspace idenitification is a modal analysis method performed mainly in the time domain, where one assumes the order of the problem first, before calculating the modal parameters based on the method of least squares errors. The calculations involved in the SSI analysis are presented based on [Brincker and Ventura, 2015, p. 254-256].

Arranging the measured data $\{\boldsymbol{y}(1)\}$ with np number of data points and 2 number of rows directly in a Hankel matrix as shown in equation (3.41), generates a matrix consisting of two block Hankel matrices $[\boldsymbol{H}_1]$ and $[\boldsymbol{H}_2]$, often noted respectively as "the past" and "the future".

$$[\boldsymbol{H}] = \begin{bmatrix} \{\boldsymbol{y}(1)\} & \{\boldsymbol{y}(2)\} & \dots & \{\boldsymbol{y}(np-2s+1)\} \\ \{\boldsymbol{y}(2)\} & \{\boldsymbol{y}(3)\} & \dots & \{\boldsymbol{y}(np-2s+2)\} \\ \vdots & \vdots & & \vdots \\ \{\boldsymbol{y}(s)\} & \{\boldsymbol{y}(s+1)\} & \dots & \{\boldsymbol{y}(np-s)\} \\ \{\boldsymbol{y}(s+1)\} & \{\boldsymbol{y}(s+2)\} & \dots & \{\boldsymbol{y}(np-s+1)\} \\ \{\boldsymbol{y}(s+2)\} & \{\boldsymbol{y}(s+3)\} & \dots & \{\boldsymbol{y}(np-s+2)\} \\ \vdots & \vdots & & \vdots \\ \{\boldsymbol{y}(2s)\} & \{\boldsymbol{y}(2s+1)\} & \dots & \{\boldsymbol{y}(np)\} \end{bmatrix} = \begin{bmatrix} [\boldsymbol{H}_1] \\ [\boldsymbol{H}_2] \end{bmatrix} \quad (3.41)$$

Constructing a projection matrix $[\boldsymbol{O}]$ by using the expression in equation (3.42).

$$[\boldsymbol{O}] = E[[\boldsymbol{H}_2]|[\boldsymbol{H}_1]] \quad (3.42)$$

Calculating this projection can be done using

$$[\boldsymbol{O}] = [\boldsymbol{T}_{21}][\boldsymbol{T}_{11}^{+}][\boldsymbol{H}_1] \tag{3.43}$$

where $[\boldsymbol{T}_{11}^{+}]$ is the pseudo inverse of $[\boldsymbol{T}_{11}]$ and the block Toeplitz matrices $[\boldsymbol{T}_{21}]$ and $[\boldsymbol{T}_{11}]$ are as follows

$$[\boldsymbol{T}_{21}] = [\boldsymbol{H}_2][\boldsymbol{H}_1]^T \tag{3.44}$$

$$[\boldsymbol{T}_{11}] = [\boldsymbol{H}_1][\boldsymbol{H}_1]^T \tag{3.45}$$

However, this computational approach is expensive. Therefore, the projection matrix is usually calculated based on the assumption that the projection can be presented by a singular value decomposition as shown in (3.47). Resulting in the following expression for the projection matrix:

$$[\boldsymbol{O}] = [\boldsymbol{\Gamma}][\boldsymbol{X}] \tag{3.46}$$

$$[\boldsymbol{O}] = [\boldsymbol{U}][\boldsymbol{S}][\boldsymbol{V}]^T \tag{3.47}$$

Then the $[\boldsymbol{\Gamma}]$ and $[\boldsymbol{X}]$ matrices in equation (3.46) can be estimated as follows.

$$[\hat{\boldsymbol{\Gamma}}] = [\boldsymbol{U}_n]\sqrt{[\boldsymbol{S}_n]} \tag{3.48}$$

$$[\hat{\boldsymbol{X}}] = \sqrt{[\boldsymbol{S}_n]}[\boldsymbol{V}_n^T] \tag{3.49}$$

In order to make sure the problem is positive valued, weighting functions may be introduced. The definitions of the filters are from [Peter van Overschee, 1996, p. 78]

$$[\boldsymbol{W}_1][\boldsymbol{O}][\boldsymbol{W}_2]^T = [\boldsymbol{U}][\boldsymbol{S}][\boldsymbol{V}]^T \tag{3.50}$$

In the Principal Component analysis the weighting function in equation (3.50) are defines as

$$[\boldsymbol{W}_1] = [\boldsymbol{I}_{li}], [\boldsymbol{W}_2] = [\boldsymbol{Y}_p]^T\sqrt{\Phi[\boldsymbol{Y}_p, \boldsymbol{Y}_p]}^{-1}[\boldsymbol{Y}_p] \tag{3.51}$$

In the Unweighted Principal Component analysis the weighting function in equation (3.50) is simply defines as

$$[\boldsymbol{W}_1] = [\boldsymbol{I}_{li}], [\boldsymbol{W}_2] = [\boldsymbol{I}_j] \tag{3.52}$$

Extended UPC, also referred to as SSI-UPCX or just UPCX, utilizes statistical calculations on the measurement data to provide dynamic property estimations with the corresponding uncertainty. This gives valuable information about the estimations based on a single data sample, and in some sense information about the quality of the data content in the sample. The procedure presented in Michael Döhler [2017] is implemented in the software ARTeMIS Modal Pro, which is used during the modal analysis in chapter 11.

3.13 Modal Assurance Criteria (MAC)

When performing modal analysis it is useful to compare the different modes that have been estimated. Such a comparison can be between modes estimated from the same estimation technique, modes estimated using different techniques or modes calculated from numerical models. The Modal Assurance Criteria, evaluated in Allemang [2003] and formulated as in the equation below, provides information about the cosine of the angle between two mode shapes squared, giving a mean to valuate whether to what degree two mode correspond with each other.

$$MAC(a_i, b_i) = \frac{|\{\boldsymbol{a}_i\}^H \{\boldsymbol{b}_i\}|^2}{(\{\boldsymbol{a}_i\}^H \{\boldsymbol{a}_i\})(\{\boldsymbol{b}_i\}^H \{\boldsymbol{b}_i\})} \tag{3.53}$$

On the bases of multiple MAC values between two sets of mode shape vectors a MAC matrix is defined. The MAC-matrix will display which mode shape vectors from the two initial sets correlates with each other.

4 — Measuring Equipment

This chapter will give a brief introduction to the equipment used in the lab, as their practical application have been emphasized, and not their technical properties. The equipment presented is the CompactRIO, accelerometers, impulse hammer, the magnet with amplifier, function generator and servo controller, and a load cell used to measure contact force.

4.1 CompactRIO

A CompactRIO system, Figure 4.1a, were used to record the data from the accelerometers and were controlled over WiFi by the use of LabVIEW on a laptop, Figure 4.1b. The recorded data were saved on a USB flash drive as ".tdms" files and are later converted to ".mat" files with MATLAB. The CompactRIO system can be configure with the desired number of analog to digital converters (ADC's). The one used in the lab was equipped with three, 4-channel ADC's, adding up to a total of 12 channels.

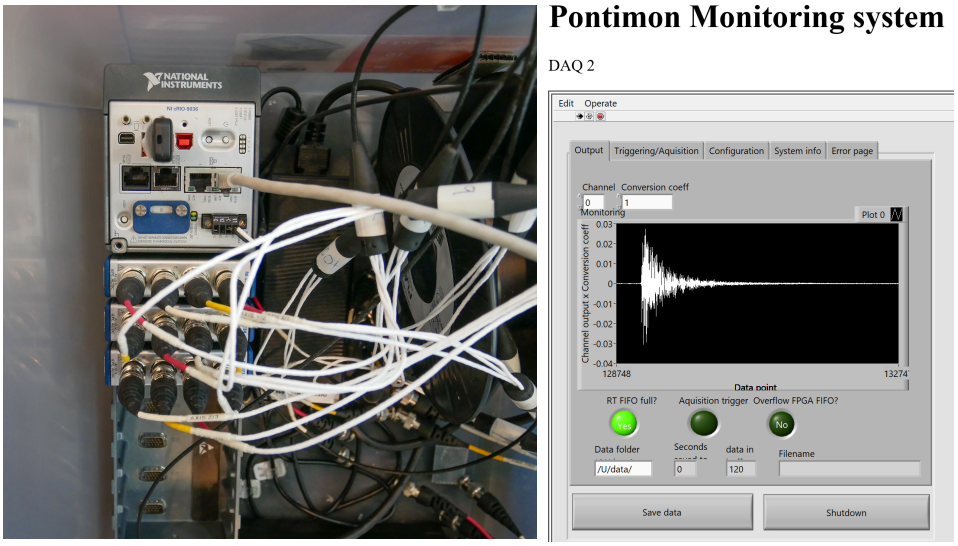

(a) CompactRIO with accelerometers attached

(b) LabVIEW

Figure 4.1: CompactRIO and LabVIEW

4.1.1 Use of the CompactRIO

The CompactRIO can be configured in multiple ways. It can either be triggered manually from the interface in LabVIEW by the ”save data” button or it can be set to trigger at a given threshold on the standard deviation on a channel, Figure 4.2. The measurements before the trigger and after can be set by defining pre- and post-trigger times. These are most useful for the impulse testing as the standard deviation trigger method was used on the hammer channel. For the sweeping measurements, the manual method was found to work the best.

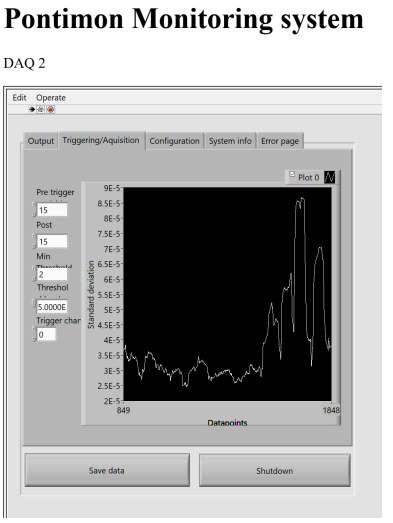

Figure 4.2: Trigger/Acquisition tab in LabVIEW

4.2 Accelerometers

The accelerometers used are Dytran 3583BT and have the possibility to measure up to 10G acceleration in x, y, and z with a sampling frequency of 4000Hz. The accelerometers can be attached to magnetic surfaces with the magnets they are screwed onto, Figure 4.3a. The total number of accelerometers supplied were 11. Since each axis require one channel the number of ADC channels in the CompactRIO setup was the limiting factor. The connectors in Figure 4.3b belongs to one sensor. The wire marked with red tape is the x-axis, yellow is the y-axis and white is the z-axis. As stated in the datasheet in Appendix A, A.1 and A.2, the accelerometers outputs 500mV/g, and were later converted in MATLAB.

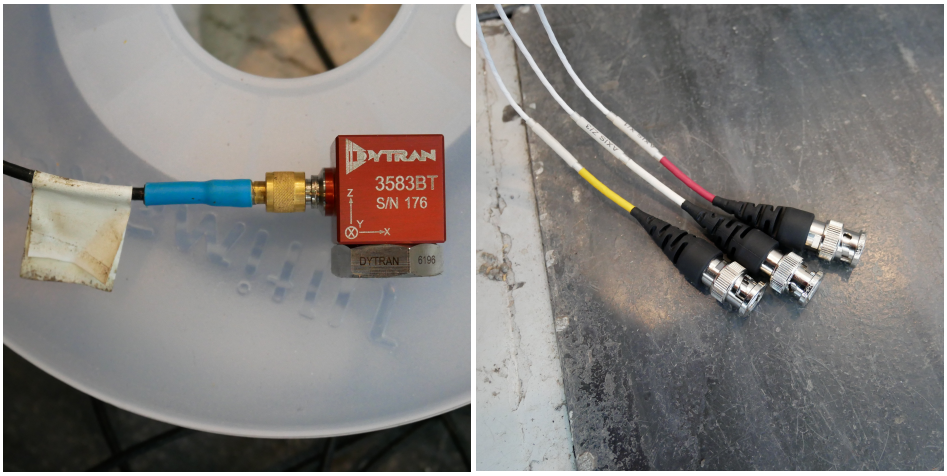

(a) Accelerometer **(b)** Connectors

Figure 4.3: Accelerometer and connectors

4.3 Impulse Hammer

The impulse hammer was only used in the testing of the accelerometer attachments in Chapter 8. The hammer was only used to trigger the recording in LabVIEW, as the analysis was performed as an output only analysis. The impulse hammer is shown in Figure 4.4.

Figure 4.4: Impulse hammer used, picture from ”Modal Hammer For Dummies”, written by Nathalie Labonnote in 2013

4.4 Magnet and Amplifier

To excite the pantograph with a given frequency, a magnet was used, Figure 4.5a. The magnet was attached to the pantograph with a steel wire and was excited by amplifying a sinusoidal signal from the function generator or servo controller with the amplifier, Figure 4.5b. The setup and interaction with the pantograph is further explained in Chapter 9, presenting the test setups.

(a) Magnet **(b)** Brüel & Kjaer Type 2712 Amplifier

Figure 4.5: Magnet and amplifier

4.5 Function generator and servo controller

To control the magnet, the amplifier requires an input signal. To generate this, two different controllers have been utilized. The first, a manual function generator, Figure 4.6a, works by selecting the desired function curve and frequency. To control the magnet, the sinusoidal curve option has been used before specifying the desired frequency by adjusting the potentiometer on the left in Figure 4.6a. The output is an AC-signal with a periodic sinusoidal shape with the requested frequency. The second controller is the servo controller in Figure 4.6b. This is a more advanced controller as it requires feedback from the system to operate. The feedback is provided by placing an accelerometer on the magnet and using the z-axis channel's signal to control the displacement and acceleration of the magnet. The servo controller can either be used as a fixed frequency generator, much like the function generator, or programmed to sweep over a requested frequency range. In addition to specifying a range to sweep, the frequency ramp must be specified in octaves per minute.

(a) Tenma 72-7710 **(b)** Labworks Inc. SC-121

Figure 4.6

4.6 Load Cell

The contact force of the pantograph was measured using a beam load cell, Figure 4.7a. The load cell was connected to a computer through an ADC. The force was displayed in kilograms and Newton, Figure 4.7b.

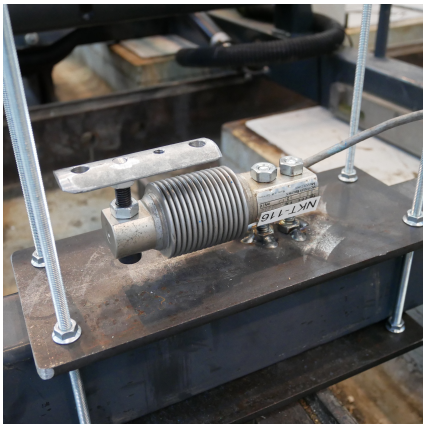

(a) Hottinger Baldwin Messtechnik Typ Z 6-4, Load cell

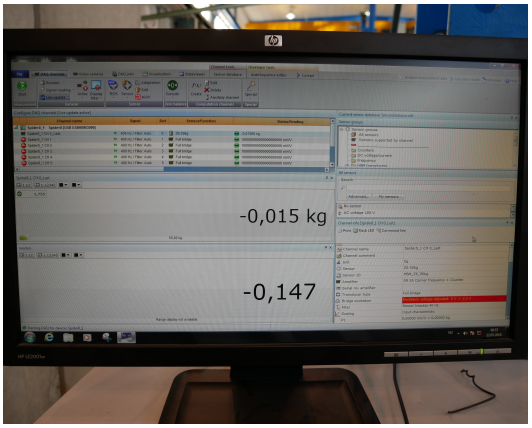

(b) PC monitoring the force

Figure 4.7: Load cell setup

5 — The pantograph system

This Chapter presents the task and function of the pantograph. The pantograph used in this thesis is a Bartels FM 2k measurement pantograph, and the differences this implies compared to a power transferring pantograph are presented here. The basic function and assembly features, such as joints and connections are presented as well as all the parts and their given names that will be used throughout the thesis. Figure 5.1a shows the pantograph in the lab, and Figure 5.1b shows the SolidWorks model of the pantograph.

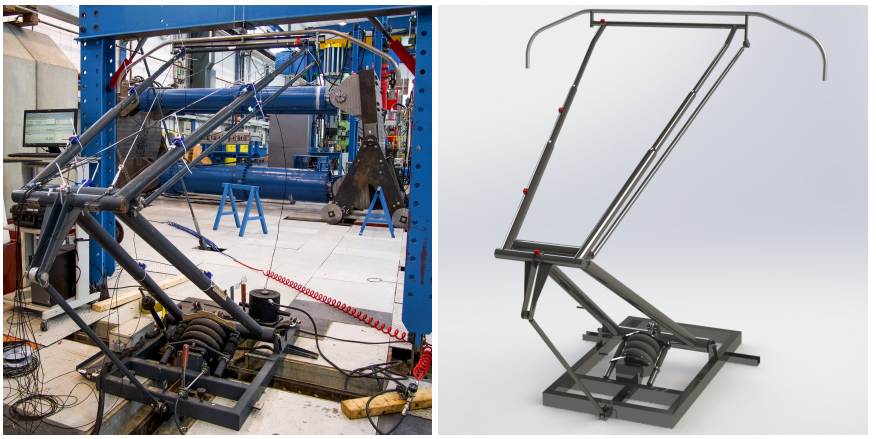

(a) Physical Pantograph **(b)** SolidWorks model

Figure 5.1: Physical model and SolidWorks model

5.1 Task and basic function

A pantograph's primary task is to transfer electric power from the catenary system to the train's motors. It consists of multiple bodies connected with bearings and joints to ensure that it can adapt to the variations in catenary height along the track. A general pantograph used to transfer power has one mechanism responsible for the large and low-frequency motions, and a head mechanism responsible for dealing with the smaller and higher frequency motions. The pantograph used in these test differs slightly from the ones used on trains. This is due to it being a measurement pantograph used to measure the height of the contact wire at low speeds. It therefore lacks the adaptive head and is instead equipped with a static bar on top. As a result, this removes the high-frequency characteristics of the pantograph head, and thus we only have the possibility to estimate the rigid body motions of the mechanism responsible for the low frequencies and the natural frequencies of the parts.

The pantograph works by pressurizing the air bellow to raise the arms. The air bellow is connected to the frame and the lower arm. As the pressure rises it causes the lower arm to

rotate at the hinge where it's connected to the frame and lift the rest of the assembly up. The upper arm is connected to the other end of the lower arm and to the frame by a rod in front. The rod causes the upper arm to rotate in the opposite direction relative to the lower arm and lift the head up. At the top of the upper arm, the head is connected. The head is also connected to the lower arm with a rod. The rod is there to keep the head oriented vertically in the whole motion of the pantograph.

When mounted correctly for use, the base frame is connected to the roof using three insulators. These are connected at the fixture points shown in 5.3g. The insulators are used because the electricity is to be transferred through cables to the motors and not through the train car. This pantograph does not have the required electrical routing since it's only used for measurement.

5.2 Parts of the pantograph

Figure 5.2 identifies the individual parts of the pantograph as the frame, the bellow, the lower arm, the upper arm, the lower rod, the upper rod and the head. The names presented under the figures will be used for future reference to the parts.

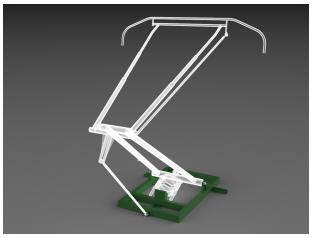

(a) Frame

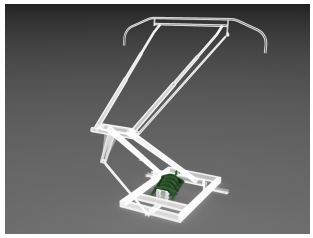

(b) Bellow

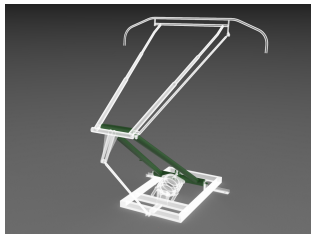

(c) Lower Arm

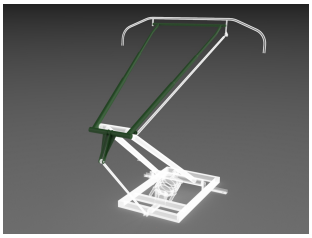

(d) Upper Arm

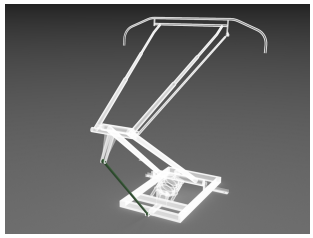

(e) Lower Rod

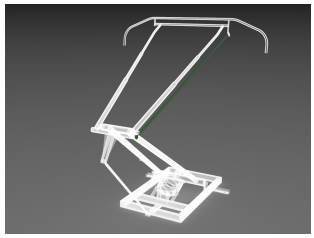

(f) Upper Rod

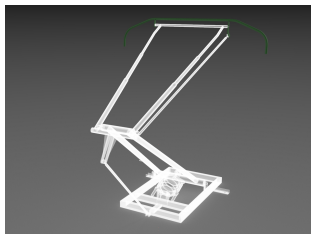

(g) Head

Figure 5.2: Pantograph part overview

5.3 Connections

The moving parts of the pantograph are connected using four different types of connections. The connections between the lower arm and the frame in Figure 5.3a, between the lower and upper arm in Figure 5.3b and on the rod connecting the frame and the upper arm in Figure 5.3h uses radial bearings. They only allow for rotation about the cylindrical direction of the bearing.

The upper rod connecting the head and the lower arm in Figure 5.3e and between the bellow and lower arm in Figure 5.3d use spherical bearings. They allow rotation in all directions, and only translation is transferred through the joint. The connection between the head and the upper arm in Figure 5.3f is a simple bolted connection with a plastic shim between the parts to minimize friction and allow the head to rotate freely.

To attach the bellow to the frame in Figure 5.3c, machined bolts are used to minimize the friction. There are no bearings used in this connection. The Pantograph itself is attached to the roof at the points highlighted is in Figure 5.3g. In the lab, the base frame is supported all along the frame as it's resting on the floor in the lab and secured with clamps.

(a) Lower Arm - Frame

(b) Lower Arm - Upper Arm

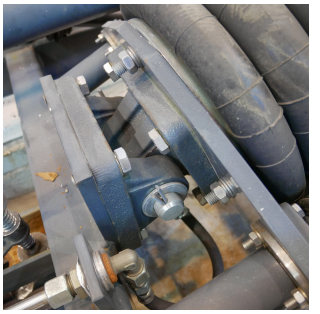

(c) Bellow - Frame

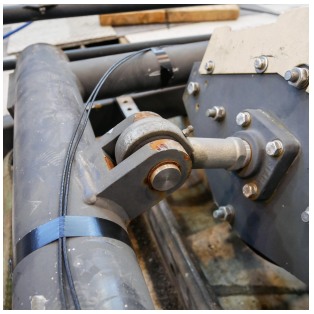

(d) Bellow-Lower Arm

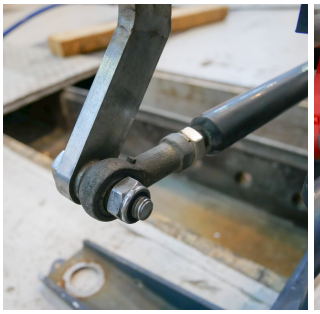

(e) Upper Rod-Head

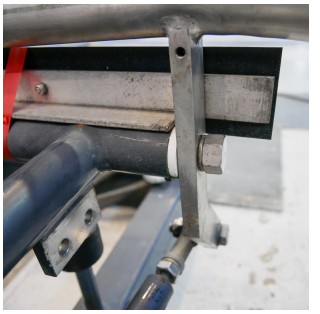

(f) Upper Arm - Head

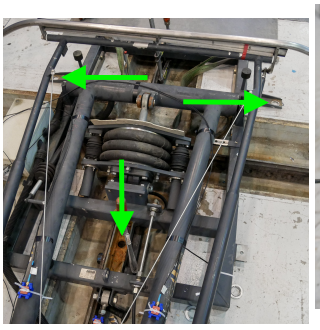

(g) Frame Fixtures

(h) Lower Rod - Upper Arm Bearing

Figure 5.3: Connections and fixtures on the Pantograph

6 — Operation of the pantograph

The first stage in operating the pantograph was to raise the pantograph. This was done by pressurizing the bellow of the pantograph. The pressure in the bellow was controlled by a simple valve seen in Figure 6.1a. The pantograph is originally delivered with a more advanced regulator to keep the pressure and force constant with the use of a feedback loop. This regulator had unfortunately not made its way to NTNU and the lab, and the results are therefore only valid for this specific setup with this controller and not the general pantograph model.

6.1 Method

Initial testing was performed with the load cell mounted to the horizontal beam over the pantograph shown in Figure 6.1b. The height of the pantograph head tube in this test was 2.019m. The pressure in the bellow was adjusted, and the corresponding contact force was read out on the computer described in Chapter 4, Figure 4.7b.

(a) Pressure regulator **(b)** Load Cell mounted to beam

Figure 6.1: Setup used to control the contact force

6.2 Results

The testing showed that controlling the pressure was very a imprecise and time-consuming process to achieve a stable force at the target value. A small adjustment of the valve could result in no change in the contact force, a significant and rapid change, or it could cause the force to drop 10N over several minutes.

6.3 Conclusion

Because of the difficult behavior of the regulator a choice regarding the contact force had to be made. The ideal contact pressure to test with would be 55N according to the technical document [Jernbaneverket, 2007] and possibly a higher force of 70N. Unfortunately, this proved to be too time-consuming, and the choice of a stable pressure providing a contact force between 40N and 60N was deemed acceptable for further testing. Note that when the tests were performed with the magnet, the force had to be dropped further down due to limitations caused by the capacity of the magnet. This is further presented in Chapter 9, Section 9.1.

7 — Contact force over the operational height

The purpose of this test it to collect data on the behavior of the bellow, how the force varies in the range of operation, the spring behavior and ratio between the displacement of the head and the bellow.

7.1 Setup

The load cell was for this test mounted to the rear lateral beam of the frame, see Figure 7.1a. The upper arm of the pantograph was attached to the load cell with a rope, see Figure 7.1b. The pantograph was raised to an operating height of 2.084m, and the measured initial force was 67.8N. Note that the rope had an angle from the vertical plane in Figure 7.1a. This was not taken into account when recording the force due to the shear compensation in the load cell, and the force applied by the bellow only acting in the vertical direction and not in the longitudinal direction. The effect of this angle was therefore assumed negligible.

The blue frame in Figure 7.1c was used as the reference to measure the height of the head. It measured 2.095m from the ground up to the underside of the flange of the beam. The displacement of the bellow was measured with a measuring gauge mounted between the plates of the bellow assembly, see Figure 7.1d. The pressure displayed on the regulator was not noted in the experiment. This was because a significant change in force did not show any significant change in pressure displayed on the gauge.

(a) Rope at an angle

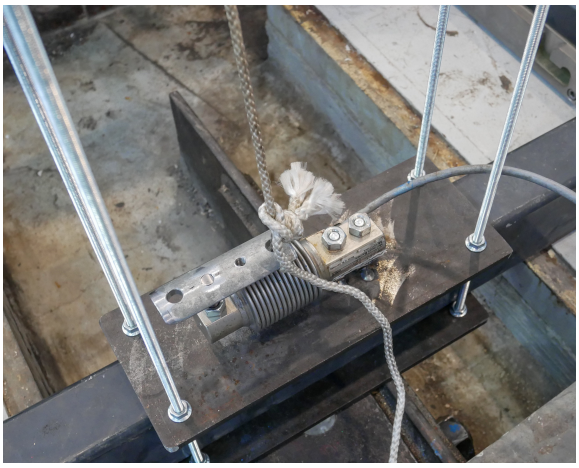

(b) Rope attached to load cell

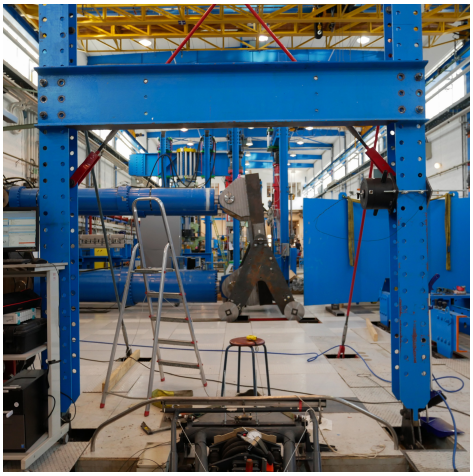

(c) Large blue frame in the Lab

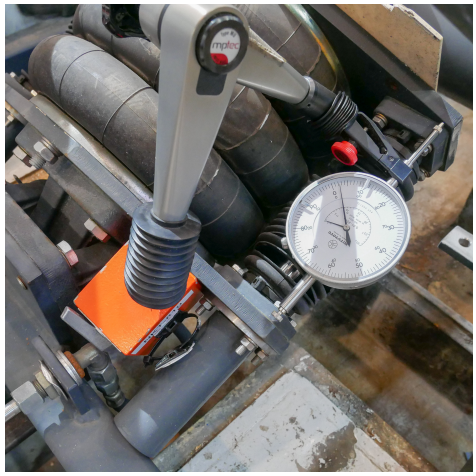

(d) Measuring gauge on bellow

Figure 7.1: Measurement setup

7.2 Method

The test was performed by manually adjusting the length of the rope. The rope was shortened in increments of roughly 1.5cm on average, and then the displacement of the head was measured and noted. The same was done for the displacement of the bellow and the force exerted on the load cell. When the head was lowered the force increased before it decreased a little over a period of time. To allow the force to stabilize, it was first noted after measuring the displacement of the head and bellow, so roughly 20 seconds after the height adjustment.

7.3 Results

The plot in Figure 7.2a shows the force the system delivers over the operation height tested in this experiment. The force measured was the stationary force when the system had stabilized. The average force in the operation range was 73.4N, with a maximum of 76.5N and minimum of 67.8N. The total change was 8.7N over the height. From Figure 7.2a it can be seen that the force was non-linear in the range tested. Observations in the data show that the force increased as the head was lowered. In Figure 7.2c the change in stiffness over the tested height is displayed. This stiffness curve is derived from the polynomial fit of the head height - force curve seen in Figure 7.2a.

From Figure 7.2b it can be seen that the relationship between the displacement of the head and the bellow can be assumed as linear in the range tested. The range for the head height was from 2.084m to 1.583m. The ratio between the head and bellow displacements are 32.8 when both displacements are converted to the same units.

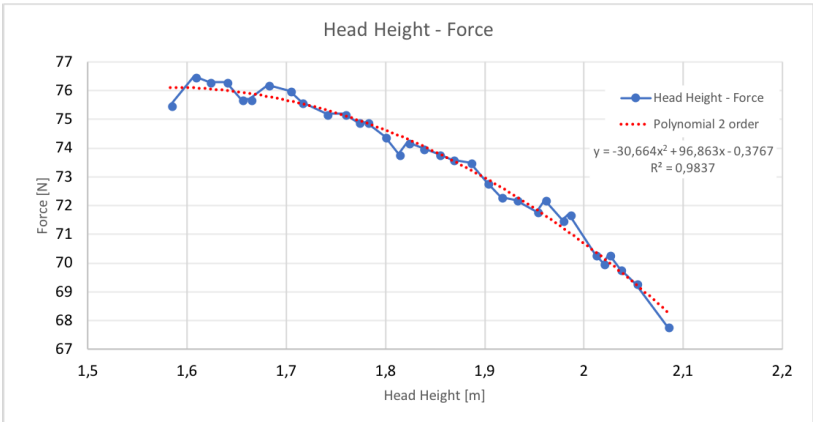

(a) Head height - Force plot

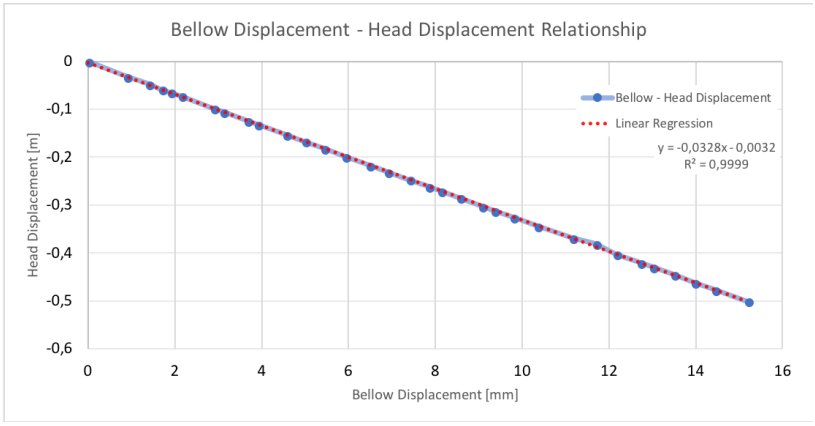

(b) Displacement relationship plot

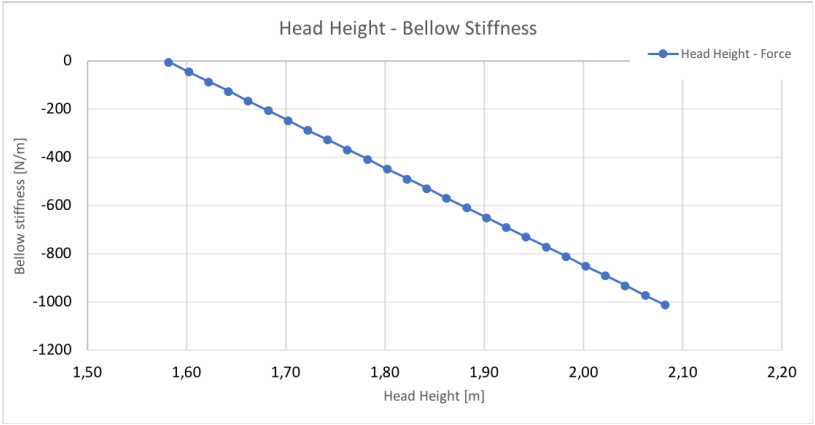

(c) Head height - Bellow stiffness plot

Figure 7.2: Force and displacement plots for the pantograph

7.4 Discussion

Regarding the results obtained, a couple of points should be highlighted. When conducting the experiment, the measurement gauge mounted between the plates of the bellow had some internal friction restricting it from extending and being in contact with the plate facing the lower arm. This was caused by the bellow being over-compressed as the rope was tied compared to the position it had when applying load on the rope. It was therefore required to manually extend the gauge for it to be in contact, thus interfering and possibly moving the gauge arm. The second point is that the measurement of the head height was conducted using a measurement tape and handling errors can occur. The third is the uncertainty of the shear compensation as this was not tested in a standalone test.

The result of the force increasing as the head was lowered contradicts the expectation that the force would remain constant as the pressure in the bellow would be constant and the ratio between bellow displacement and the head displacement is constant. However, the observation of the force increasing as the head is lowered, before gradually decreasing and then stabilizing leads one to believe that the valve could release some pressure over time. Similarly, the effect of the force increasing as the head is lowered, before the curve in Figure 7.2a flattens out, indicates that there is some internal friction in the relief valve. As the pressure reaches the level resulting in a force of 76N, it seems like the valve releases all excessive air as this is the threshold of the spring mechanism in the valve. This is assumed to be the cause of the stiffness, that is resulting in a change in force delivered by the bellow, in Figure 7.2c to gradually decrease until it reaches zero. The change in the force when the head is lowered, is therefore assumed to be an effect of the regulator.

7.5 Conclusion

The relationship between the displacement of the head and bellow is concluded to be linear in the range tested. The change in the force over the height is caused by the regulator and not the characteristic of the system. The results obtained concerning the bellow in this test can be considered as parameters of the stationary system, and are not transferable as parameters to establish a model for the bellow in the dynamic model. The dynamic properties of the bellow therefore need to be defined through dynamic studies.

8 — Accelerometer attachment

When mounting the accelerometers to the structure, it is essential to constrain the accelerometers sufficiently to the structure. This is to prevent the accelerometers from sliding, rotating or rocking on the surface it is attached to. Any bad connections can corrupt the recorded responses of the system. In this chapter, the quality of the connections and how to assure that they are sufficient will be addressed.

8.1 Initial testing only using magnets

In this section, a validation of the connections is presented along with suggestions for better attachment solutions.

8.1.1 Setup

The test was performed with the accelerometers attached to the upper arm. One accelerometer was attached on the 30mm tube, one on the 40mm tube and the third on the 50mm tube, see Figure 8.1b. The accelerometers were attached only by the use of magnets, while the cables were stretched along the tube and secured with cable ties to minimize the forces exerted on the accelerometers by the wires. The measurements were performed in the local y-direction of the accelerometers, i.e. towards the right in Figure 8.1b. The axis of the accelerometers can be seen in Figure 8.1a.

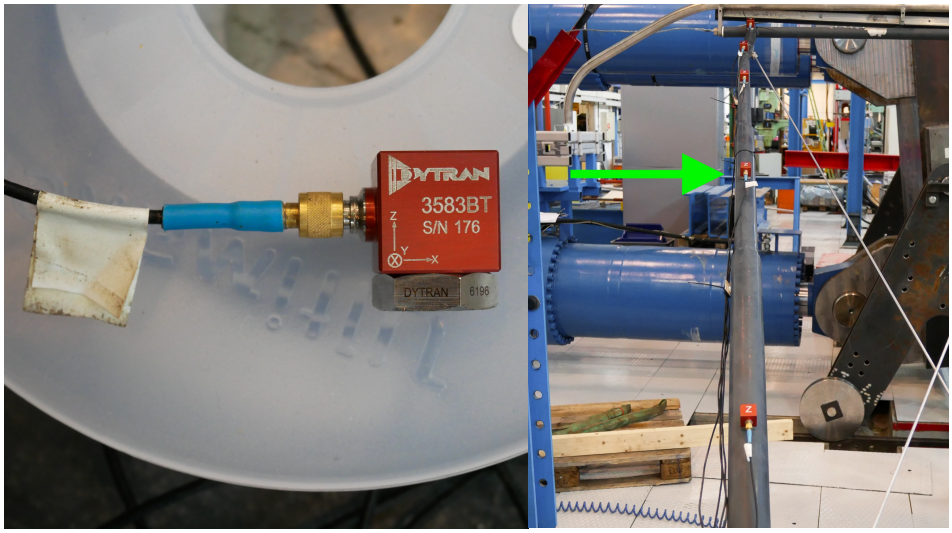

(a) Magnet screwed into the accelerometer **(b)** Arrangement of sensors

Figure 8.1: Accelerometers, placement of them and point of impact

8.1.2 Method

Two different types of tests were performed. The first was lateral excitement of the pantograph. In this test, an impulse hammer was used. The hammer blow was applied at the sensor placed on the 40mm tube, in the direction and at the point of the green arrow in Figure 8.1b. The analysis performed was an output only analysis, and the impulse hammer was used merely to trigger the recording on the CompactRIO.

The second test was the actuation of the sensors rocking on the pipes. This was performed using a finger to angle the sensor on the tube, before releasing it. See Figure 8.2b.

To estimate the response of the system, five series were recorded. For each of the series, the power spectral density for each channel was calculated, and the results were averaged to filter out errors. The same method was applied on the second test, but here three series were recorded for each of the sensors.

Welch's method was used to estimate the spectrums. The time series were cut in length to reduce the amount of energy included for frequencies consisting of noise since the response of interest decays quickly and the recordings where much longer than required. To ensure the appropriate accuracy of the natural frequencies the minimum frequency resolution was set to 0.1Hz. This resulted in a required time series length of minimum 5 seconds using a sampling frequency of 400Hz, and one Welch window. Since this was an impulse test the uniform window, also known as the rectangular window, was used.

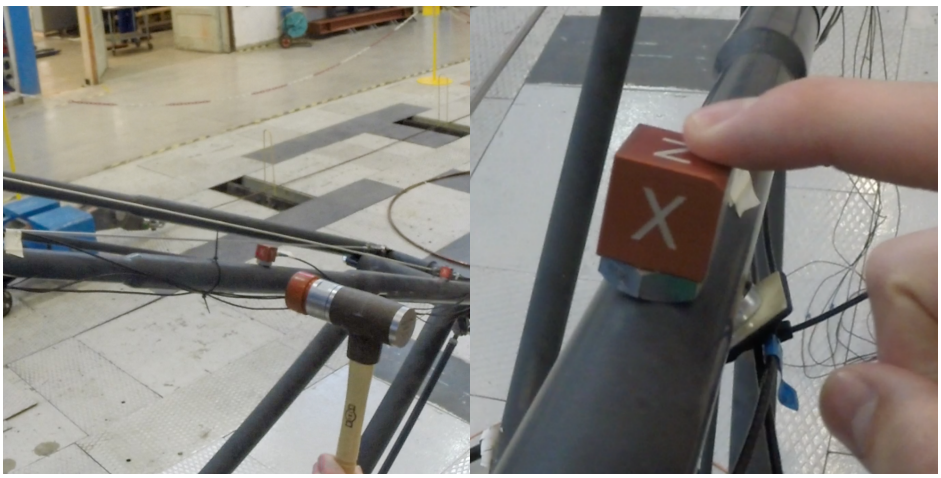

(a) Impulse hammer **(b)** Actuation by finger

Figure 8.2: Actuation method

8.1.3 Results

One of the series recorded by the lateral excitement using the impulse hammer was corrupt and it was not possible to convert from the recorded file format .tdms to .mat. Therefore, only four series were used. The spectrum of the sensor rocking on the tube is multiplied in the comparison spectrums to increase readability. The reason for it being lower is that the total energy in the test is lower than the one performed on the system response.

In Figure 8.3a, the time series of the accelerometer attached to the 30mm tube can be viewed. The response dies out quickly, and the series were therefore cut to the minimum of 5 seconds. The spectrum of the response shows two peaks. One at 24.61Hz and the other at 49.61Hz.

The time series of the accelerometers rocking on the 30mm tube also decays rapidly, Figure 8.4a. These series were therefore also cut to the minimum length of 5 seconds. The time series for the sensors on the 40mm and 50mm tubes can be viewed in the Appendix A. The spectrum of the sensor rocking on the 30mm tube shows one peak at 32.42Hz, Figure 8.4b.

In Figure 8.5 both the spectrums are plotted. From the plot, it is evident that the two spectrums have energy in the same frequency range. This is even more apparent for the 40mm tube, Figure 8.6c, where the two coincide. The comparison of the spectrums on the 50mm pipe, Figure 8.7c, also shows this tendency.

Response recorded on 30mm tube

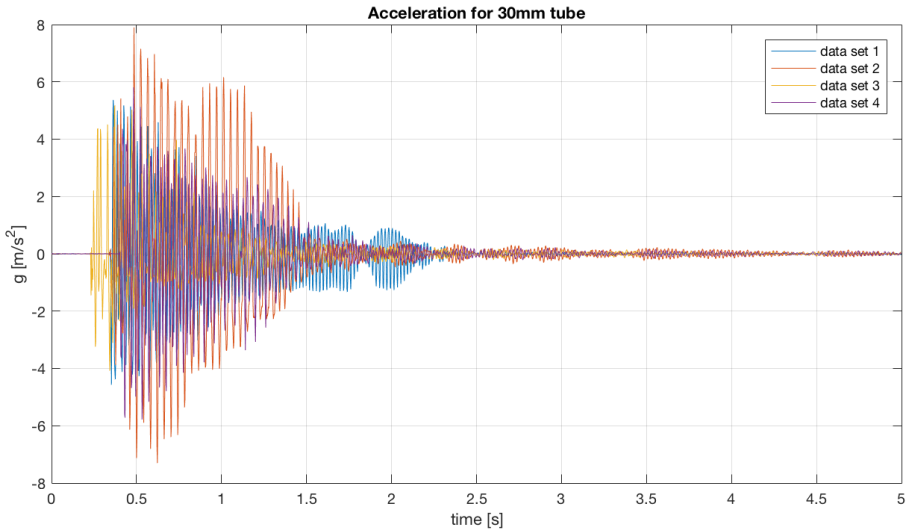

(a) Cut time series

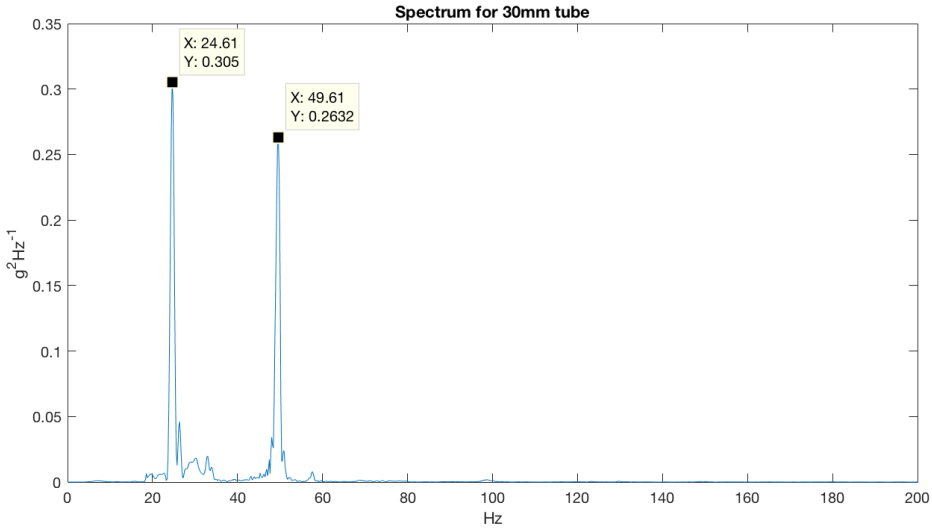

(b) PSD of time series

Figure 8.3: Recorded system response, 30mm tube

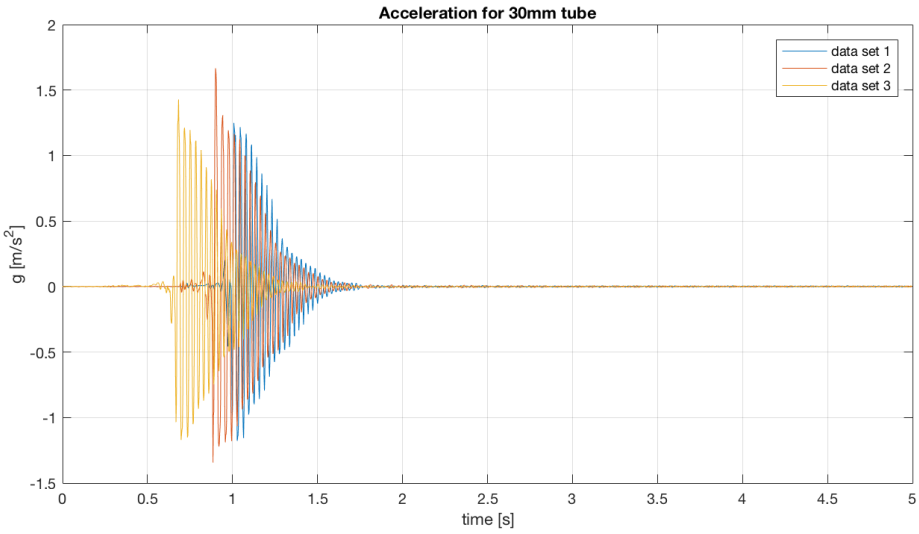

(a) Cut time series

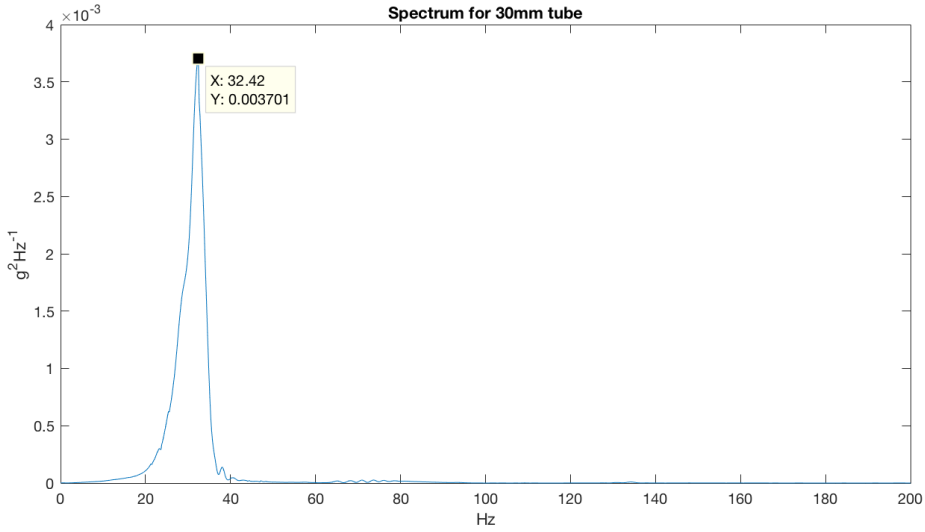

(b) PSD of time series

Figure 8.4: Recorded frequency of sensor rocking on 30mm tube

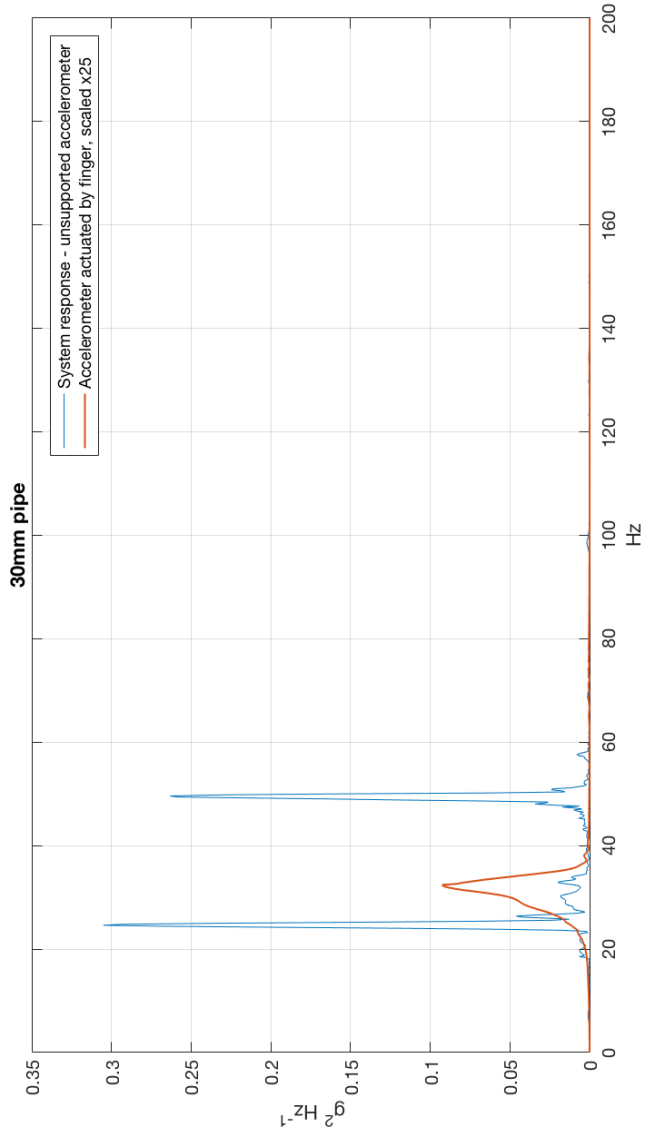

Figure 8.5: Comparison of system response spectrum and rocking sensor spectrum, 30mm

Response recorded on 40mm tube

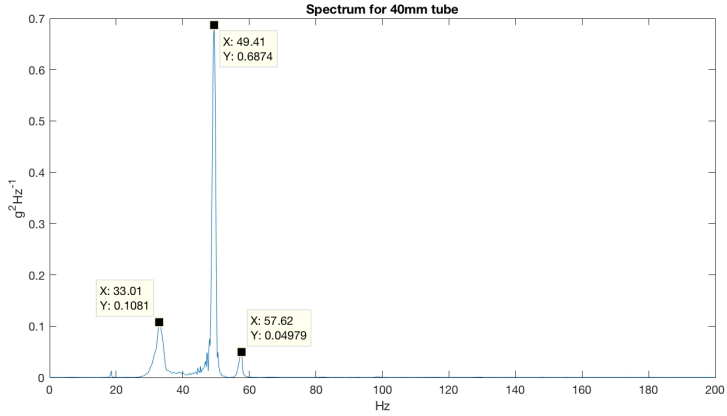

(a) PSD of system response

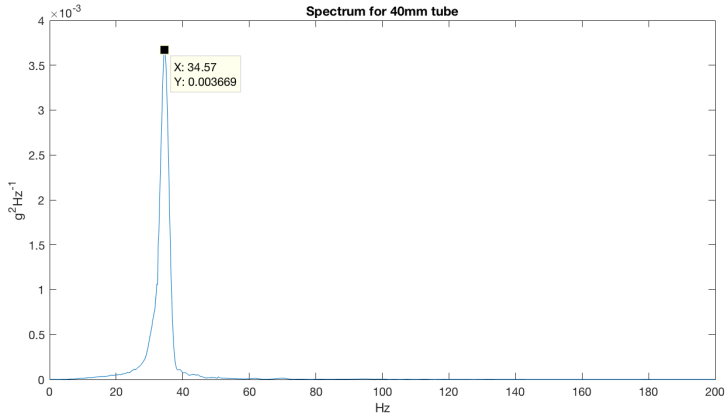

(b) PSD of rocking accelerometer

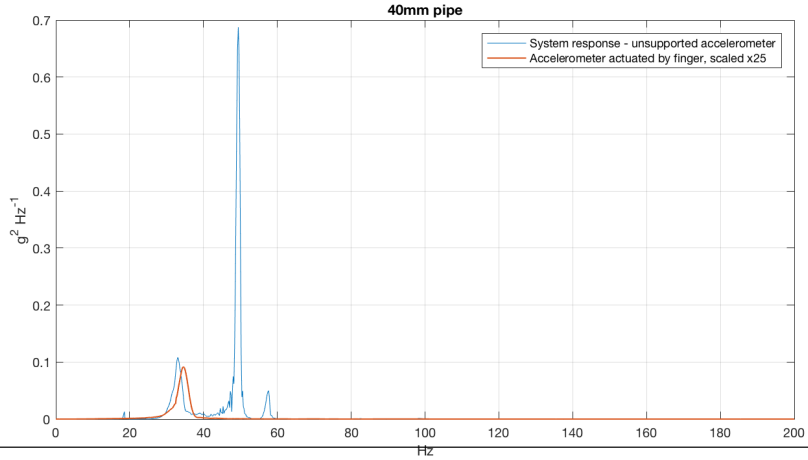

(c) Comparison of system response spectrum and rocking sensor spectrum

Figure 8.6: Spectrums, 40mm tube

Response recorded on 50mm tube

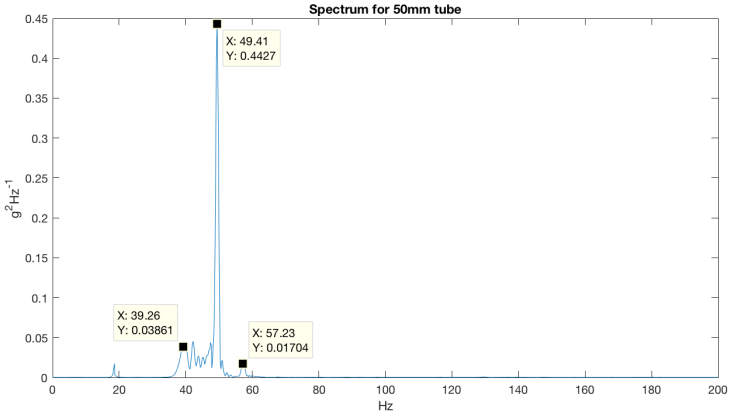

(a) PSD of system response

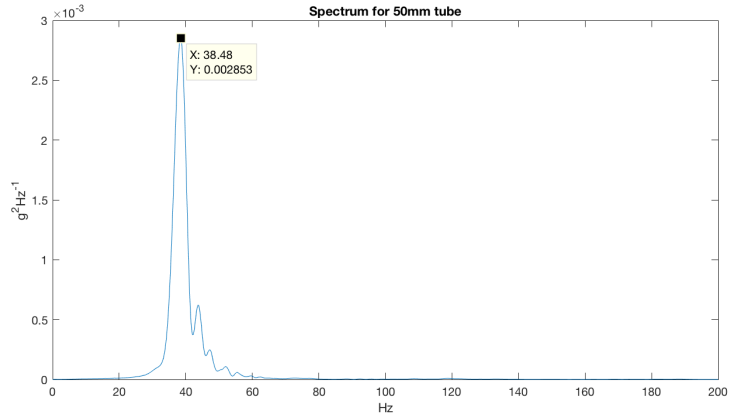

(b) PSD of rocking accelerometer

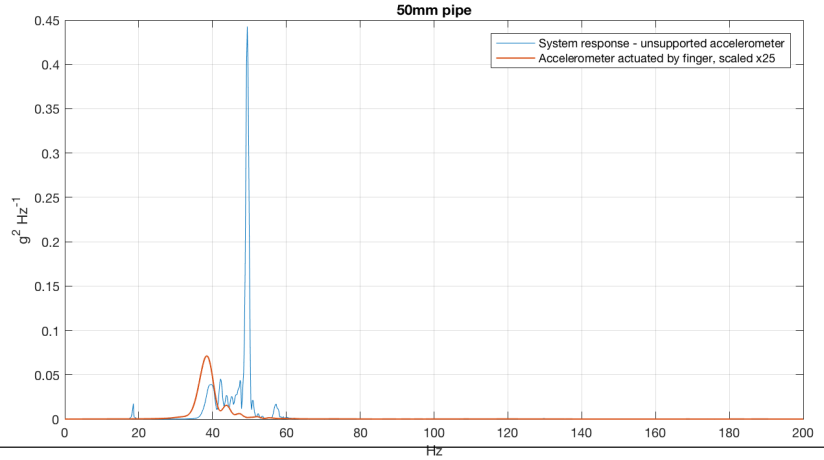

(c) Comparison of system response spectrum and rocking sensor spectrum

Figure 8.7: Spectrums, 50mm tube

8.1.4 Discussion

From the comparison plots of the spectrums, it can be seen that the system responses have energy in the same frequencies as the sensors rocking on the profiles. Since all the sensors were placed on the same element, even though it changes cross-section along the length, it was expected to find peaks at the same frequencies along the length. For the peaks at 49.41Hz and the one right above 57Hz, this is the case. While for the lower frequencies closer to the frequencies of the sensors rocking, this is not the case. This points to the interaction between the accelerometer and tube interfering with the response of the system.

Another indicator that points to the connection being insufficient is the lack of response at higher frequencies in the structure. From the basic theory of beam dynamics presented in section 2.3, it is expected to find a harmonic at four times the base frequency corresponding to a single sinusoidal shape. For all three profiles, there is a lack of energy above 60Hz which could indicate a loss of energy transfer.

8.1.5 Conclusion

Based on the results obtained it is likely that the connection is insufficient and the information is lost. It was therefore decided to spend more time exploring better ways to attach the accelerometers to see if there was any loss of energy.

8.1.6 Possible solutions to improve attachement

Three possible solutions to the problem were discussed. The first is to grind the profiles flat at the points of interest, in regard to sensor placement. This was quickly chosen as the backup if the others failed due to a couple of cons. It is not a flexible solution and requires a good understanding of the system to reduce the number of grinding points. It also compromises the integrity of the structure and damages the protective paint layer on the steel parts.

The second solution was to use cable ties. This was tested on the profiles, but due to inconsistent pre-tensioning and capacity of the cable ties made it quite time-consuming to get the connection adequate. The cable ties had low friction for rotating the accelerometer around the cross-section, and a more stable solution was desired.

The third, and in the end chosen solution, was to develop sensors supports. The goal was to create a 3D printed support bracket that was easy to mount, gave adequate support and was easy to attach to the structure.

8.2 Development of sensor supports

The primary objective for the sensor support bracket is to fit on all the tube profiles used on the pantograph, in order to ensure adequate attachment of sensors. The outer diameter of the tubes varies from 90mm to 22mm. The support brackets are to be printed on an Ultimaker V2 in plastic material PLA.

8.2.1 Design

The support brackets are designed to be a tight fit around the accelerometers to ensure that all the motion are transferred. The accelerometers are to be attached using their magnets when the supports are used. The supports will assist by inhibiting the accelerometer from rocking on the profile in both directions. The sensor with support will be secured with cable ties.

To help secure the cable ties from sliding two groves are made on each side of the accelerometer, see Figure 8.8b and 8.9a. These are placed high enough so that they do not intersect with the cable from the accelerometer, see Figure 8.8a. In addition there are made cut-outs at the sides of the sensor to allow for a cable tie going around the cross-section and the accelerometer with the supports, see Figure 8.10a and 8.10b. The angled feet of the supports allow them to fit on cross sections of varying dimensions, see Figure 8.9b.

Machine drawing can be found in Appendix A, A.7.

8.2.2 Production method

To obtain a tight fit, the support brackets were printed with scaling of 99%, 100%, and 101%. The 99% printed bracket was too tight, while the 100% bracket was a perfect fit.

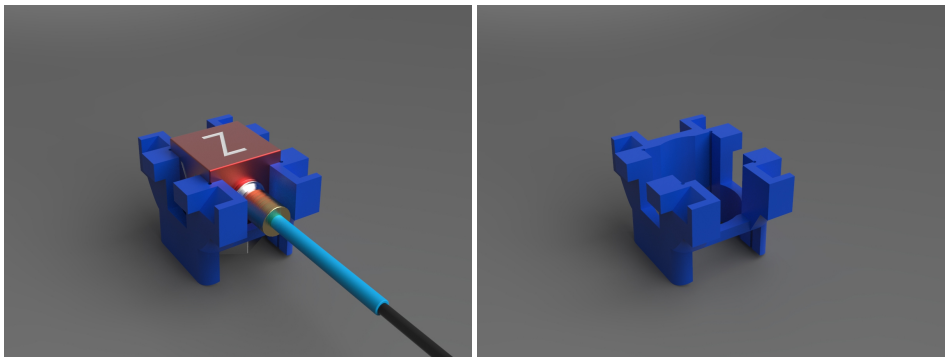

(a) Sensor support with sensor **(b)** Sensor support bracket

Figure 8.8: Sensor support render

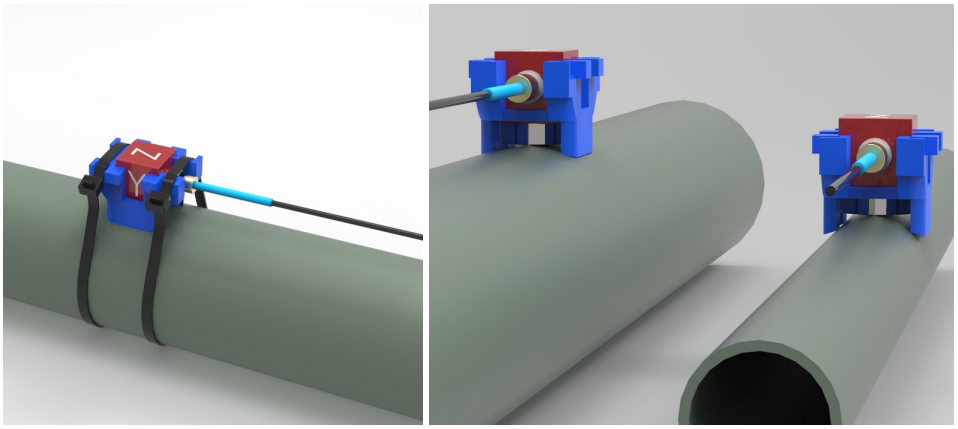

(a) Single sensor secured with cable ties **(b)** Accelerometers on different cross sections

Figure 8.9: Accelerometers mounted with support brackets

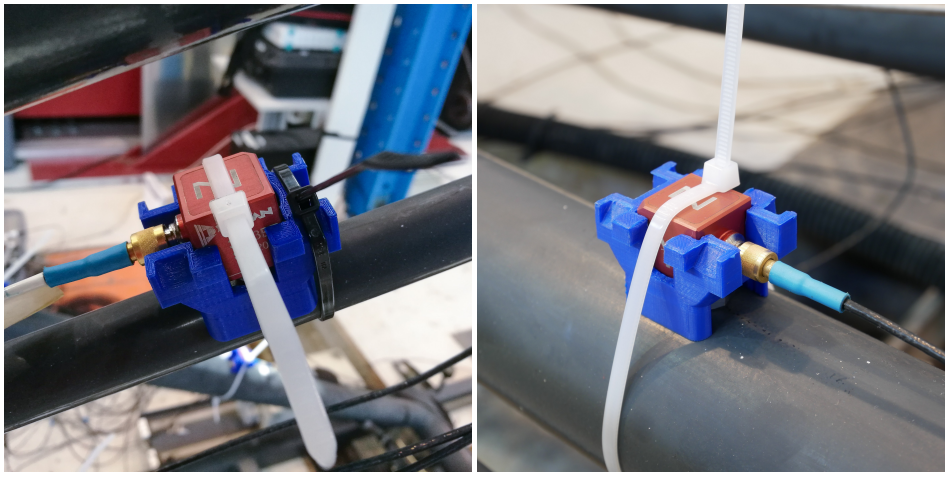

(a) Upper rod, Ø22mm **(b)** Lower arm, Ø65mm

Figure 8.10: Accelerometer with support and cable ties in lab

8.3 Testing with the supports

With the produced supports, as described in the previous section, the same test as in section 8.1 were performed, and the results will be presented here.

8.3.1 Setup and method

The setup and method were the same as without the supports, except that the accelerometers were attached using the supports, Figure 8.11.

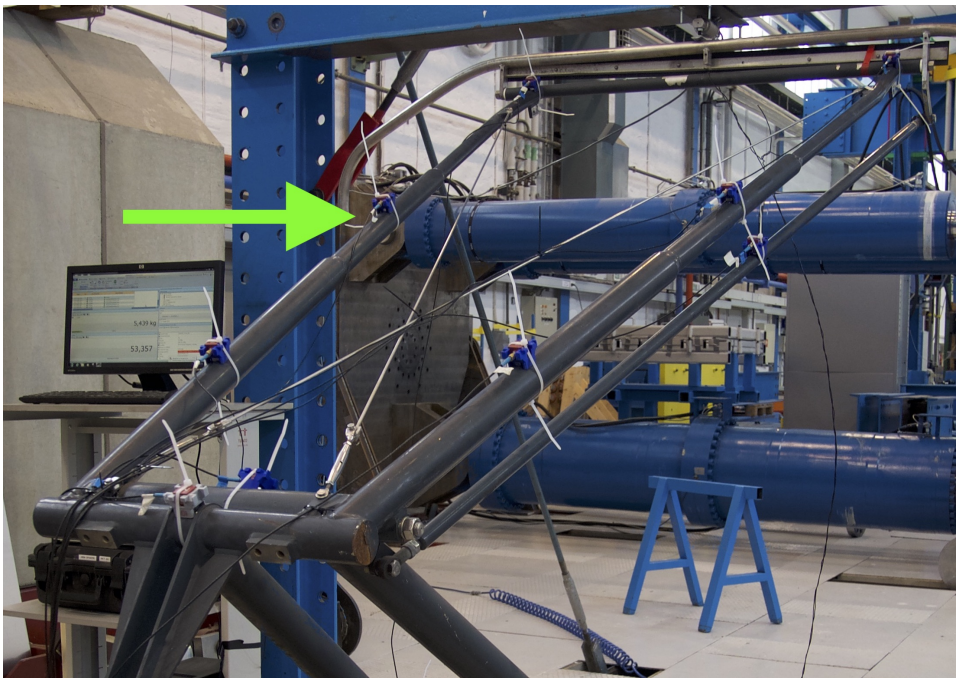

Figure 8.11: Accelerometers with supports

8.3.2 Results

From the time series in Figure 8.12a and 8.12b the signal recorded with the accelerometers mounted with the supports shows cleaner signal with the characteristic decaying amplitude.

Figure 8.13 shows the spectrums from the initial testing of the system with the accelerometers only attached with magnets, the natural frequency of the sensors rocking, and the system response with supports. In the spectrums obtained with supports, there is no energy in the frequency range of the sensors rocking on the profiles. All three sensors are recording a response at 48.54Hz and 56.84Hz. In contrast to the spectrums without the supports, peaks above 60Hz have emerged in the spectrums. All three sensors show a peak at 129.3-129.4Hz. The sensor mounted on the 30mm tube has some energy at 178.1Hz. This can barely be seen in the spectrum for the 40mm tube and is not visible in the spectrum of the 50mm tube.

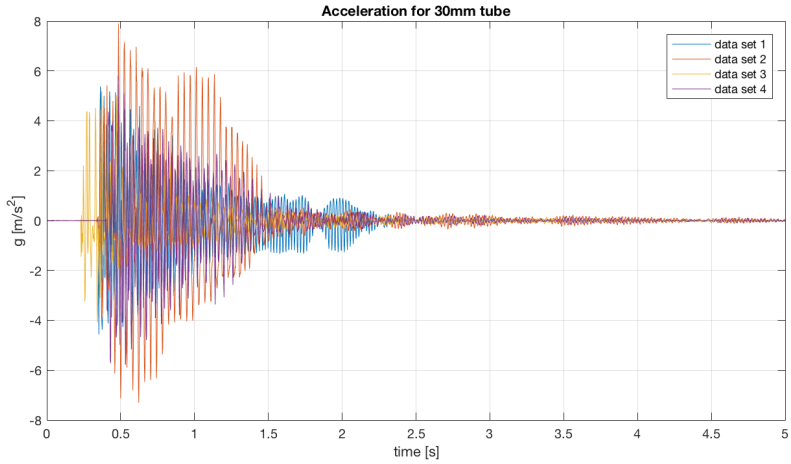

(a) Time series unsupported accelerometer, 30mm tube

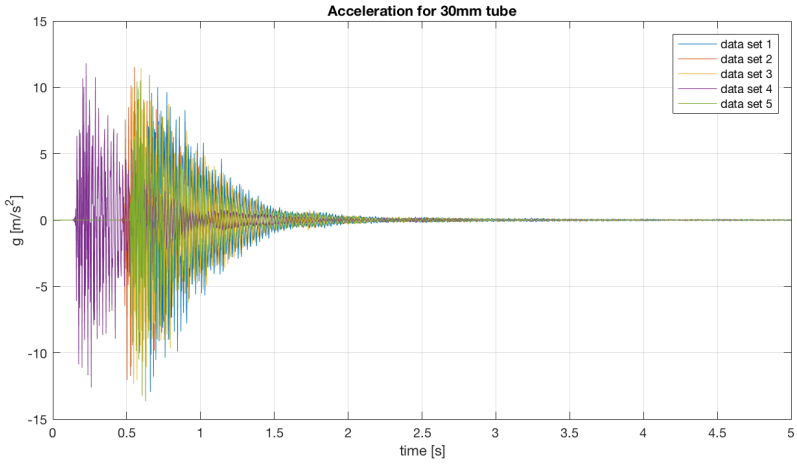

(b) Time series supported accelerometer, 30mm tube

Figure 8.12: Comparison of time series 30mm tube

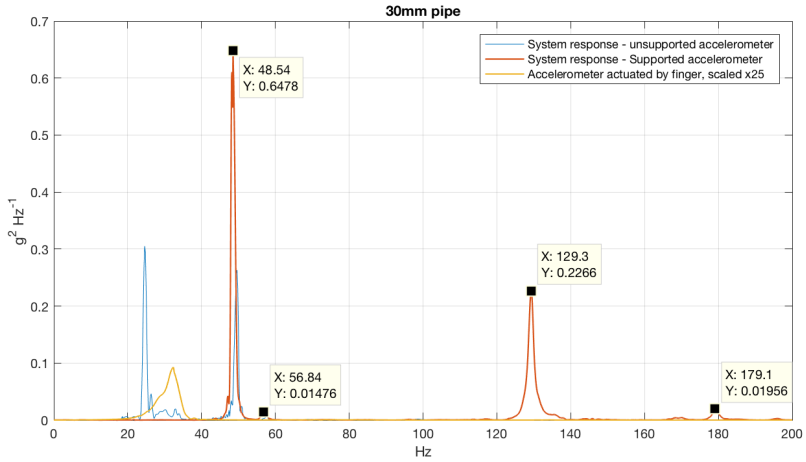

(a) 30mm tube

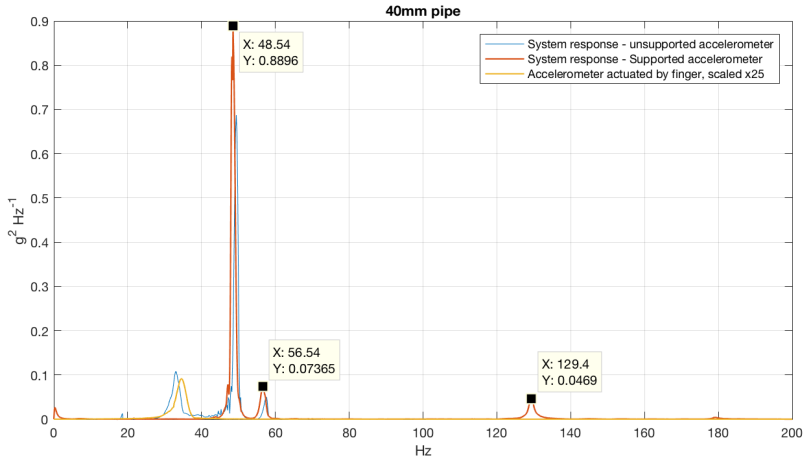

(b) 40mm tube

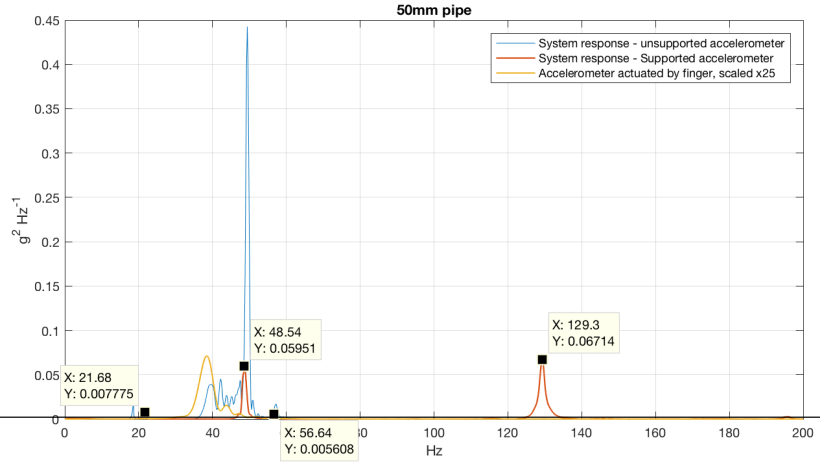

(c) 50mm tube

Figure 8.13: System response spectrums

8.3.3 Discussion

From the results, it is quite apparent that the sensor support bracket removes the natural frequency of the sensor rocking on the profile. The system response spectrum is altered by removing fake system resonance frequencies introduced by poor attachment. By the use of the supports, high-frequency vibrations are successfully transferred from the structure to the accelerometers.

A limitation with these supports is that the mounting of the accelerometers is limited to the element axis. When analyzing the global vertical modes, it would be practical to have the sensors mounted in the global CYC axis, presented in chapter 9. This would require pantograph and part specific brackets to get the correct orientation. These brackets would also separate the magnet of the accelerometer from the element of the pantograph and possibly require a more in-depth study of the transfer of frequencies and possible natural frequencies in the brackets.

From Figure 8.12 the time series with the supports have the expected decaying behavior compared to the response recorded for the unsupported sensors. The response without the supports has a more random decay function. This could be caused by a combination of the rocking motion and sliding on the profile as the hammer blow was applied.

From the results all three sensors contain the same frequencies for the tube. Thus the transfer is assumed to be successful. The upper peak of 179.1Hz seen in the spectrum for the 30mm tube, and barely in the spectrum of the 40mm tube could be a local mode of the 30mm tube or a response of the head that is transferred down the tube.

8.3.4 Conclusion

The attachment using the sensor supports ensures that the vibrations of the structure are transferred and removes false frequencies in the connection. They are therefore used in further measurements of the pantograph response measurements as the default attachment method. It is further assumed that for all further test the system frequencies, within the considered domain of 0-200Hz, are transferred to the accelerometer without introducing any artificial frequencies in the connection.

9 — Dynamic response setup

This chapter presents the general lab setup and conditions for the dynamic testing of the pantograph. Further, the part specific setups are presented, and finally the observations of the first modes of the pantograph are presented.

9.1 General Setup

Here, general conditions and choices made for the setups, applying for all the part specific setups, are presented.

9.1.1 Boundary conditions

In all tests, the frame was resting on the concrete floor in the lab and clamped at the front and rear. With this boundary condition, it is assumed that some of the response of the frame will be removed from the response of the system. This is possible to change in the lab setup in future work by attaching the pantograph at the fixture points. Other variables possible to change are the operating height of the pantograph, different pressures and hence contact forces.

9.1.2 Connection between magnet and pantograph

For all the tests the magnet was attached to the pantograph at the upper arm on the center of the lateral top tube, Figure 9.1a. The magnet was attached using a steel wire which was looped and twisted around the tube and the bolt in the magnet, Figure 9.1b. The natural frequencies of the steel wire have not been calculated analytically because the twisting at the ends resulted in a varying stiffness at the ends compared to the middle. At different frequencies, the wire was observed swinging with the whole length, and also with a reduced effective length where the twisted ends had no deflection. Because of this, the assumption that the wire transfers all frequencies applied by the magnet was made. However, the wire may amplify false responses in the pantograph, and a transfer function for the wire was established for two different contact forces in chapter 10, section 10.1.3.

The magnet was in all these tests connected to the pantograph using a wire, where the magnet restricted the pantograph. This boundary condition can be changed in future experiments to check the consequence of friction at the head and how it changes both the vertical and lateral modes of the structure. This can be achieved by letting the pantograph rest against the load cell or any other surface. A quick study in the lab showed that the friction of the load cell removed the first lateral mode, presented at the end of this chapter, from the structure. While substituting the load cell with a polished wrench allowed the structure to be excited by this mode. This was an interesting effect, but was not investigated further due to other analyzes being prioritized.

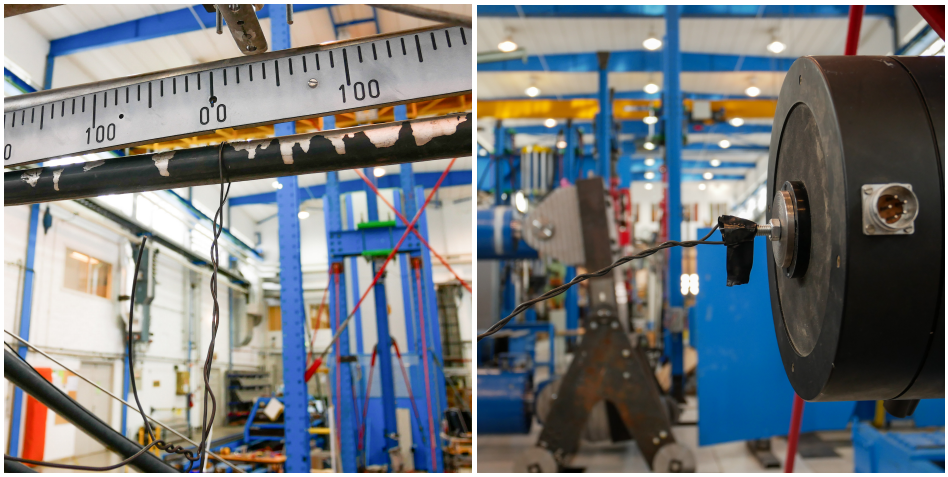

(a) Wire on pantograph **(b)** Wire on magnet

Figure 9.1: Wire attaching magnet to pantograph

9.1.3 Attachment and placing of accelerometers

With the accelerometers mounted on the elements of the pantograph with the x-axis pointing along the tube, the center of the accelerometer is offset from the center of the cross-sections. As a result, torsion of the cross-section will be read as translation by the accelerometers in the y-axis. A possible solution to solve this would be to place one accelerometer on the top, and one underneath the cross-section and averaging the two. This was not prioritized in any of the setups since it requires additional accelerometers and ADC channels. The polar moment of inertia is assumed to be higher than the second moment of area, and bending is assumed to occur before torsion in the cross-sections. Another possible error in the recordings is that bending of the cross-section will result in output in the x-axis of the accelerometer, if it is pointing in the longitudinal direction of the tube.

The weight of accelerometers mounted on the structure was 47 grams with the supports, without cable ties and cables. As mass is increased, the natural frequency will decrease. Effects of the added mass will be presented and discussed in the analysis of data using ARTeMIS in chapter 11, and by analysis of the Abaqus model in chapter 12. For all tests performed the accelerometers were attached using magnets with support brackets and cable ties except for the head where electrical tape has been used since the head tube is made out of aluminum, thus making the magnets insufficient.

9.1.4 Excitation method

Due to the limitations in the number of accelerometers and ADC's in the CompactRIO, the measurements have been performed part by part, and for the upper arm in separate directions. All the series presented in this chapter are swept with a frequency ramp of 5 octaves/min. For all the sweeps the start frequency was 2Hz, as it's the lowest possible with the controller, up to 195Hz, and then down again until the controller hit the power threshold and stopped. The servo controller tried to adjust the power of the output to reach the target acceleration and displacement, but hit the power threshold around 5Hz for most of the series. The manual of the controller was unavailable, and by tweaking the values, it was impossible to get it down to 2Hz again. It is assumed that the integral component of the PID-controller became too large on the way down. The assumed cause is too little resonance in the range 20-40Hz. Thus, a small amplitude of the magnet leads to a large error being integrated over time in the controller and then it reaches the power ceiling. Ultimately, stopping the sweep.

9.1.5 Contact force and test series

The forces presented in Table 9.1 is not the direct contact force. This is because the force was measured before running the test by lifting the magnet and allowing the pantograph head to rest against the load cell. After the force was registered the magnet was placed back down on the ground, and the tests were run. The forces were low when doing these tests compared to the standard Norwegian force of $55N \pm 10\%$, [Jernbaneverket, 2007]. This is because the magnet had to constrain the pantograph in the vertical direction and the rubber holding the core of the magnet in place was limiting the amount of force during magnet operation, see Figure 9.1b.

Part	Ref	Series	Direction	Force	Sweep [Hz]	# sensors
Head	A	2018-05-11-15-28-24	Multiple	33,5N	2-195-4.8	7
Upper arm	B	2018-05-10-15-37-40	Lateral	38,0N	2-195-7.8	9
Upper arm	C	2018-05-10-14-33-26	Vertical	38.8N	2-195-5.4	9
Lower arm	D	2018-05-12-13-41-15	Multiple	32,2N	2-195-4.9	7
Upper rod	E	2018-05-12-14-43-02	Multiple	29.6N	2-195-4.8	5
Lower rod	F	2018-05-12-16-37-39	Multiple	31,2N	2-195-5	4

Table 9.1: Series used in Artemis

9.1.6 Global coordinate system

The global coordinate system (GCYC) of the pantograph is defined as shown in Figure 9.2. The axis is shifted to the right in the Figure to illustrate the direction of X and Z better. The Origin is in the middle of the rear frame member and coincides with the GCYC used in the Abaqus model and ARTeMIS analysis.

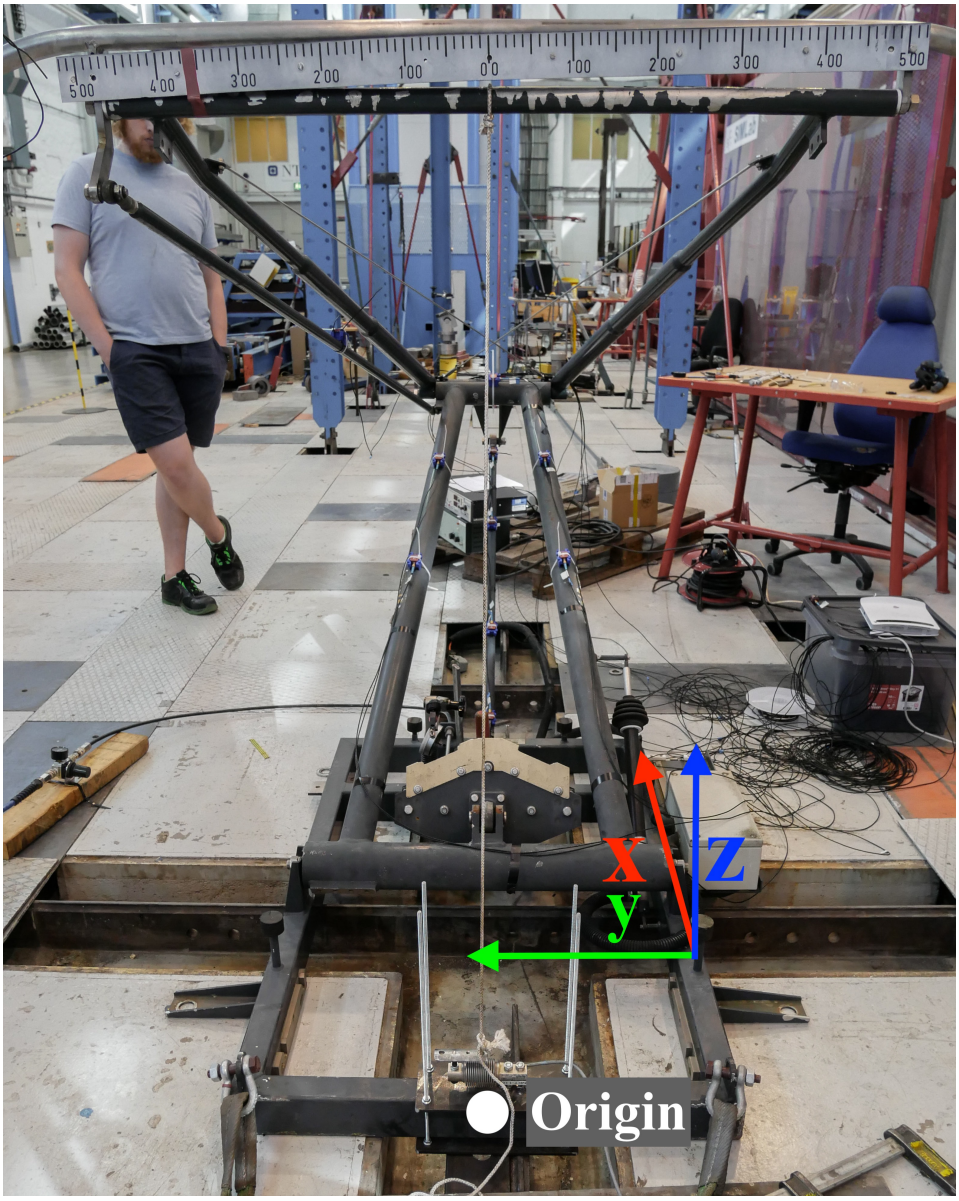

Figure 9.2: Global CYC

9.2 Setup, Head

The setup of the accelerometers on the head can be seen in Figure 9.3. In the Figure, the axis recorded by the accelerometers are shown. The z'-axis is the axis pointing perpendicular to the tube in the y-z plane. The other axis coincide with those of the GCYC.

The points measuring in x-direction out on the tubes were chosen to measure the tube swinging in phase and out of phase. The x-direction, recorded in the middle of the head, was selected to record any possible higher order modes of the center tube in the x-direction. The y-direction in the center was selected to record the lateral swinging of the head caused by global and element modes further down in the system.

The position measuring in the z-direction at the connection to the upper arm was chosen to detect any rocking of the upper arm and as a reference to the movement of the outer tubes and center in the z-direction. The z'-direction was chosen to help determine the vertical modes in combination with the outer z-direction accelerometers, as well as give an indication of the movement in the y-direction at the point.

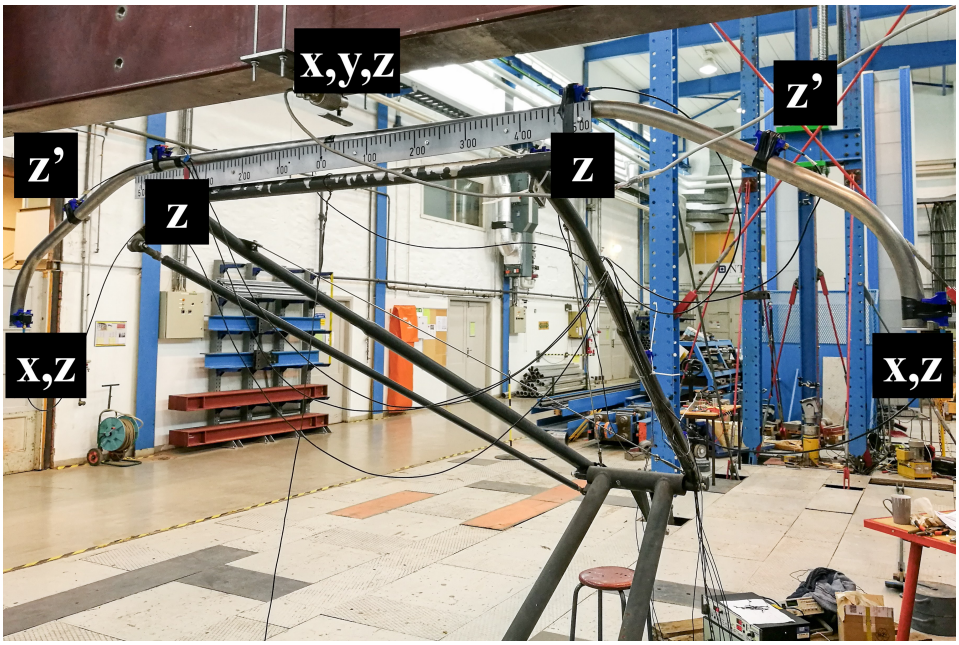

Figure 9.3: The head with accelerometers and recorded axis

9.3 Setup, Upper arm

The measurements of the upper arm were performed in two steps. The first setup was used to record the response in the vertical direction, and the second in the lateral direction. The z'-axis denoted in Figure 9.4 and 9.5 are perpendicular to the longitudinal direction of the tubes and the global y-direction. The apostrophe is dropped in the y-direction notation due to this differ ± 5 degrees depending on the side. This is taken into account in the later analysis. The last accelerometer was measuring the z'-direction of the upper rod. The two setups had the accelerometers attached at the same points and two of the accelerometers measured in two directions in both setups to be used as a reference to compare results.

The accelerometers were spread out on both arms to record the global twisting of the upper arm and the phase of the bending modes of the two beams running in the global x-direction. Additional accelerometers were attached to the left arm to provide a better estimation of the mode shape of the tube since the cross-section varies along the length. Note, the tube on the right-hand side is equal to the left one and is assumed to have the same behavior. Measurements in the x-direction have been prioritized since they are assumed linked to the movement of the lower arm and very little axial strain in the component compared to bending.

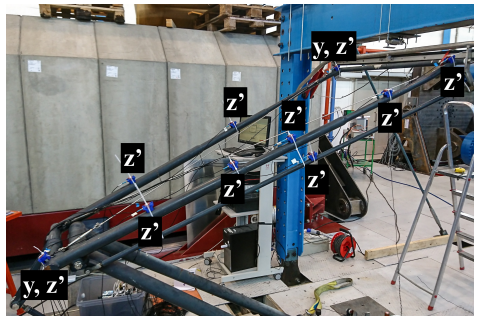

Figure 9.4: Upper arm with accelerometers and recording in z-direction

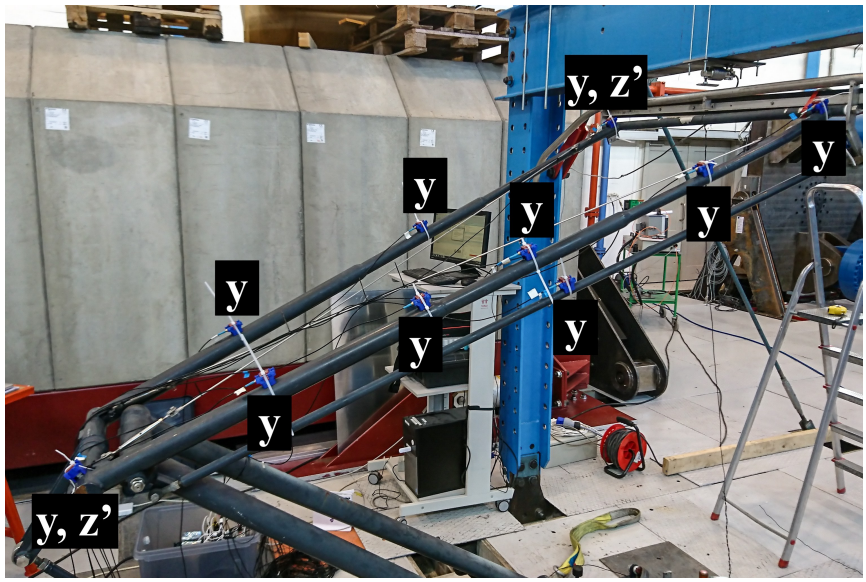

Figure 9.5: Upper arm with accelerometers and recording in y-direction

9.4 Setup, Lower arm

The z'-axis is perpendicular to the tubes and the global y-direction. The accelerometer mounted to the lateral tube was oriented after the element, the local x-axis of the accelerometer then corresponds to the global y-axis. On the tubes, the y-direction is not denoted by apostrophe since they are ± 7 degrees depending on the side.
The accelerometer setup was chosen with an equal number of accelerometers on each tube. This was done to catch the phase between the two beams in the arm and because higher order modes requiring more than 3 sensors along the arm are expected to be out of the measured frequency range. Measurements in the x-direction were dropped due to the lower arm being connected directly to the frame and the deflection in the vertical beams on the frame holding the lower arm is assumed to be very low.

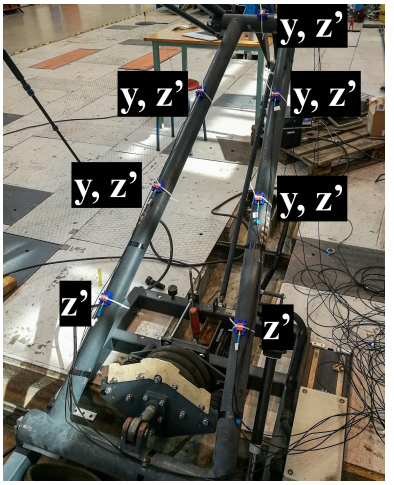

Figure 9.6: Lower arm with z'-axis perpendicular to the arm, y in global CYC

9.5 Setup, Upper rod

On the upper rod the x'-axis is running parallel to the longitudinal axis of the rod. The z'-axis is perpendicular to the tubes in the vertical plane, and the y-direction is as previously very close to the global CYC y-direction. The accelerometers at the ends of the rod were chosen to have a reference to calculate the natural frequencies of the rod because the global modes excite the rod since it is placed far out in the system with respect to the fixture. The measurements of the x'-direction at the ends were chosen to see how the modes of the rod influence the connection between the head and lower arm with respect to translation.

Three accelerometers are placed between the endpoints to calculate higher order modes since the stiffness of the rod is low. Note, adding five accelerometers to the rod that is relatively light might create a shift in the natural frequencies of the rod.

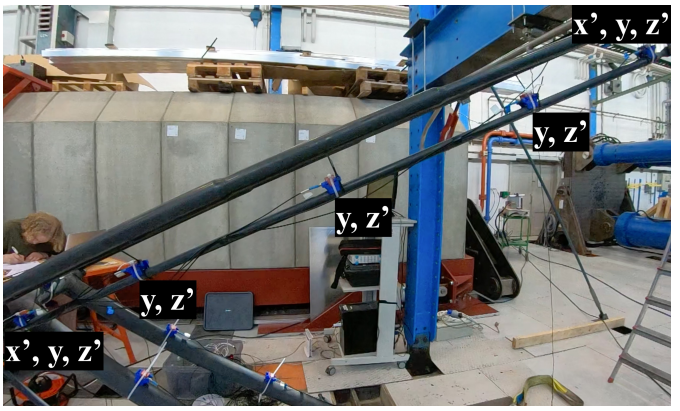

Figure 9.7: Upper rod with x' longitudinal and z' perpendicular to the rod

9.6 Setup, Lower rod

For the lower rod the x'-axis is running parallel to the longitudinal axis of the rod. The y-axis is the global y-axis. The z'-axis is perpendicular to the tube and y-axis.

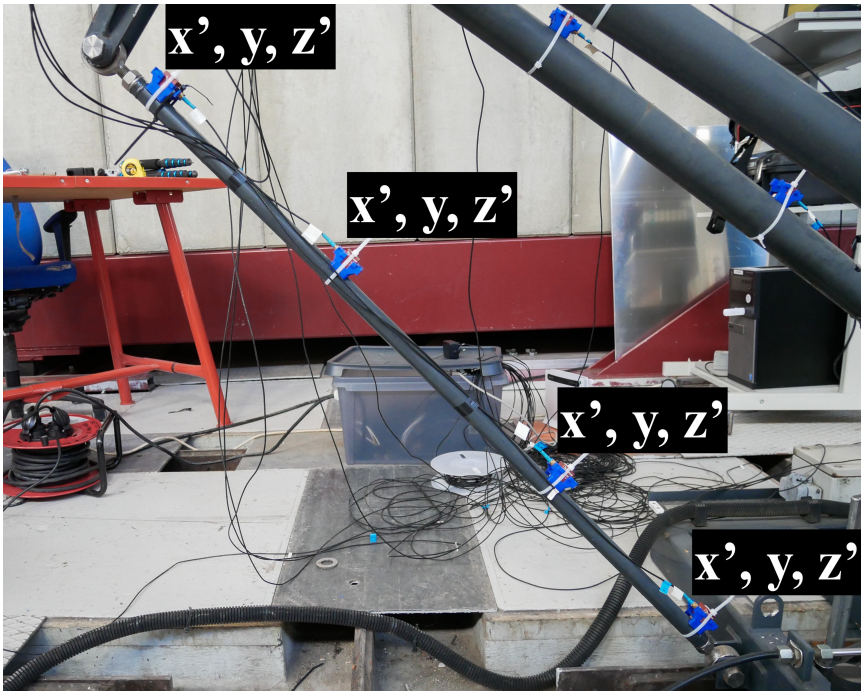

Figure 9.8: Lower rod with x' longitudinal and z' perpendicular to the rod

9.7 Discussion

The process of using the servo controller was time-consuming. As mentioned in the subsection 9.1.4, the controller hit the effect threshold and the fault led lit up as it stopped. The requested displacement and acceleration of the input accelerometer were adjusted in combination with the octaves/min. It was possible to get it down to 2Hz again by turning up the octaves, but then the sweep was very quick over the high-frequencies. It was therefore chosen to lower the octaves and lose the 3 lowest Hz on the way down since the behavior has been studied in case study 5, chapter 10, section 10.1.5.

9.8 Observed response

In this section, the observed response of the system will be presented. The response has been filmed with a GoPro Hero 6 at 120/240Fps. The contact force was 30.5N. The video files are handed in with the scripts, and any reader without these at hand may contact either us, the writers or the university to get them. In this section, pictures from Abaqus and ARTeMIS will be used to present the modes observed as it is easier to display the deformation and undeformed shape with an overlay plot instead of frames from the video. The observed first modes will be used to compare and discuss the responses found by analysis in ARTeMIS and case study 4 in MATLAB.

9.8.1 RBM bellow mode, 2.6Hz

The bellow is acting as a spring in this mode, and the lower arm is swinging up and down. The lower arm and upper arm moves in phase in the vertical direction. The observed frequency of 2.6Hz is not necessarily the correct peak, as this mode is highly damped and therefore the response occurs in a large frequency domain.

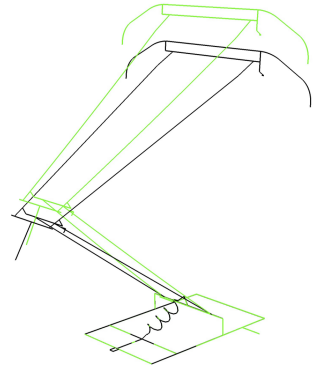

(a) RBM bellow mode

9.8.2 Upper arm lateral swing mode, 6.4Hz

The Upper Arm and the Head are swinging in the lateral direction.

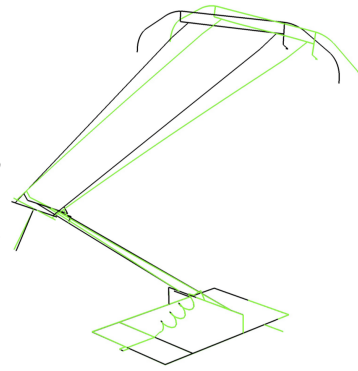

(a) Upper Arm lateral swing mode

9.8.3 Knee bending mode, 8.9Hz

The bearings in the knee, i.e. the connection between the Lower Arm and Upper Arm, is rotating. The Lower Arm and Upper Arm are moving in counter phase in the vertical direction. As the Lower Arm goes up, the head is on the way down and causes the Upper Arm to bend down. The lower arm moves rigidly, and the dynamic behavior is a contribution from the bellow.

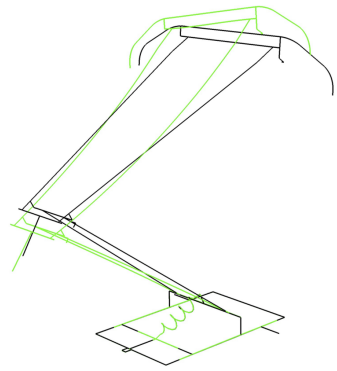

(a) Knee bending mode

9.8.4 Upper arm twisting mode, 11.6Hz

The upper arm is twisting about the longitudinal axis. As the right arm deflects down, the left deflects up causing the head to rotate about the global x-axis.

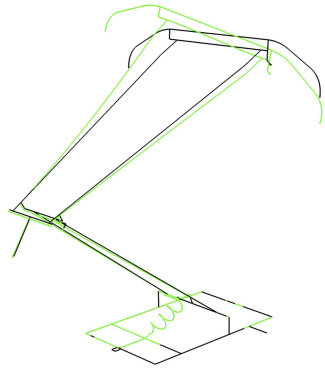

(a) Upper Arm twisting mode

9.8.5 Upper rod bending mode, 17.73Hz

At 17.18Hz the Upper Rod has its first bending mode. The whole rod vibrates up and down with a half sine shape. This introduces twisting in the Upper Arm and Head similar but smaller than the 11.719Hz twisting mode.

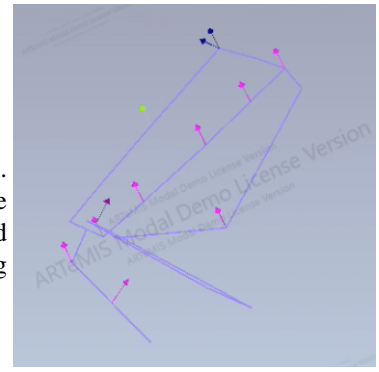

(a) Upper Arm twisting mode

10 — Studies targeted at specific behaviour

This chapter presents multiple studies performed with scripts written in MATLAB. The first study looks at the effect of windowing in Welch's method, and how this helps to clean up the spectrums for further analysis. The second study looks at the variance between multiple recorded responses performed with the same test setup. This was done to check the variation between the series since only one series was used in the ARTeMIS analysis per part. The third study looks at the transfer function of the wire, and its dependencies of the contact force. This information is useful when evaluating and interpreting the results obtained in other analysis. The fourth study determines the behavior of the upper arm by peak-picking and operational mode shape estimation with the focus on the rigid body modes and the first natural frequencies of the upper arm. The fifth study looks at the effect of changing the pressure in the bellow and how it influences the dynamic properties. The theory applied in the code is presented in the chapter of signal processing, 3.

In case study 4, only one part was analyzed using the MATLAB script. This was due to the time-consuming process and certain limitations in the results obtained. This will be elaborated in the results and discussion at the end of this chapter.

10.1 Method

Several different data sets were used in the studies below. Study 1, 2 and 4 were all performed on data recorded with test setup C described in Chapter 9. Setup C describes only the second data series of the three series that were used here. The series used were 2018-05-10-14-28-59_cut.mat, 2018-05-10-14-33-26_cut.mat and 2018-05-10-14-37-37.mat. The analysis was performed with the MATLAB script
Upper_Arm_Z_direction_sweep.m, and the contact force in setup C was 38.8N. The time series, ending on "-37-37.mat" was swept from 2-195 Hz and not down again as the two other. The first and second series were therefore cut to match the third series. They were cut at the beginning to match the start point of the third series, and then the end was cut such that the same amount of sampling points were used in all three series.

Case study 3 and 5 have been performed with specific data sets recorded for only those analysis, and they are described more in detail in their sections. All series have been processed without any filters applied. The setup used in case study 3 and 5 are is presented in section 10.1.7.

10.1.1 Case study 1, Windowing

For practical reasons windowing have been used in the process of analyzing the series. It is required that the process windowing is applied to should be stationary, which was not the case for the system since the frequency of the force was different in all the windows. The use of windowing still proved useful to clean up the ripple effects and maximum value

peaks in the spectrums. Figure 10.6 in the results shows the effect of varying number of Welch windows. From the results obtained by this study, the spectrums calculated in study 2 and 4 both use 10 Welch windows providing a resolution of the frequency axis of 0.1Hz. The data sets in study 3 and 5 vary in length, and are therefore processed with a different number of windows.

10.1.2 Case study 2, Variation between multiple series recorded with the same setup

In ARTeMIS only one series was used to analyze the response of each part. This was due to the time limitation of the license to the software. It is therefore desired to check the variation between multiple series recorded with the same setup. The series was as mentioned introductorily cut to match in length since one of the series was shorter than the other two. All three series were swept with a frequency ramp of 5 octaves per minute from 2Hz to 195Hz and with the same displacement and acceleration request on the servo controller. As a result, the content in the series should be equal since the start of the series are matched, and they are of equal length.

10.1.3 Case study 3, Transfer function of the wire

In order to analyze the dynamic behavior of the pantograph, it is handy to have information about the dynamic response of the wire used to connect the magnet to the pantograph. In this study, a transfer function of the wire was established using the spectrum of the input recorded on the magnet to divide the spectrum obtained at the wire attachment point of the upper arm. The theory is presented in chapter 3, section 3.1. The system was tested with two different contact forces, one test with 25.7N and the other with 43.2N. Two different sweeps were performed for each contact force, one from 2Hz up to 16Hz and back down again twice, 2-16-2-16-2Hz, and the other from 2Hz to 195Hz back down to 6.4Hz, 2-195-6.4Hz. The servo controller stopped at 6.4Hz on the way down due to control problem mentioned in chapter 9, section 9.1.

The calculations were performed using 8 Welch windows, providing a resolution on the frequency axis of 0.0488Hz. The natural frequencies of the wire have not been calculated analytically because, at the ends, the wire was twisted around itself causing a higher local stiffness. The focus has instead been to get some data about the behavior, and have this in mind when analyzing the behavior of the pantograph.

10.1.4 Case study 4, Determining resonance frequencies and responses

The dynamic response to the parts of the pantograph can be divided into two categories, rigid body modes caused by global mechanisms or introduced from resonance in other parts of the system, and the parts own resonance modes.

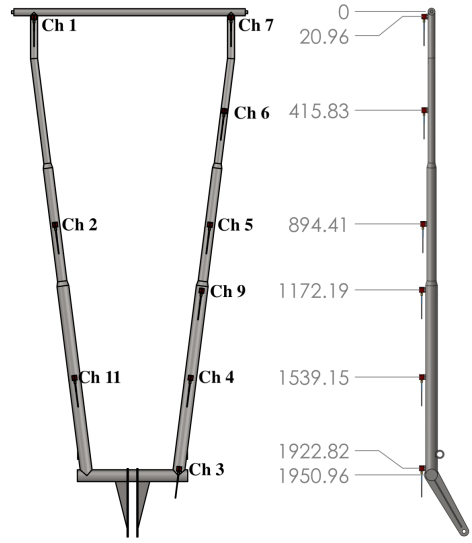

Figure 10.1: Setup of sensors on the upper arm in setup C, top view, left-hand tube is the right-hand tube in the Figure

The response of the upper arm have has calculated twice. Once with the original time series, then with the time series generated after removing the rigid body mode contribution. From the channels along the left beam element of the upper arm, the spectrums have been plotted, and the peaks have been picked. The frequencies are sorted after how many of the channels they appeared in, and in ascending order. The modes have been calculated using operational shape identification according to section 3.10. It was assumed that the frequencies found on the left-hand side also occurs on the right-hand side of the pantograph, and were therefore used in the process of comparing responses of the two sides.

Remove Rigid Body Motion (RBM)

In an attempt of determining the mode shapes of the upper arm, the rigid body motion was removed from the acceleration data. This was done utilizing the accelerometers on the end of the element to calculate the translation and rotation of the part. For the upper arm channel 3 and 7 in Figure 10.1 were used. The weakness of this approach is that the response is assumed to be a sine function with zero value at each end. If the true response is a half sine with a cantilever end, i.e., the 0 point is at 0 and 0.8 of the length, this approach will give the response the shape of a half sine instead. The solid black line in Figure 10.2 illustrates the shape at resonance, the dotted line illustrates the undeformed shape. The red line in Figure 10.2b shows the new estimated rigid body movement the shape is calculated from.

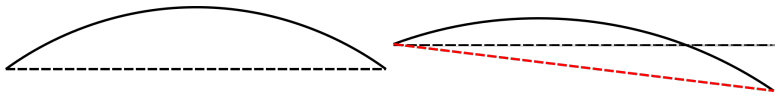

(a) Deformed half sine shape **(b)** Wrongly estimated mode shape

Figure 10.2: Incorrect shape estimation

The rigid body components of the response are calculated as follows.

$$z_m(t) = \frac{z_0(t) + z_L(t)}{2} \tag{10.1}$$

$$\theta(t) = \frac{z_0(t) - z_L(t)}{L} \tag{10.2}$$

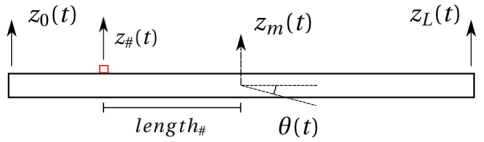

Figure 10.3: Beam element displaying equations 10.1 and 10.2, and sensor calculation.

Each sensor along the length of the element are then recalculated as follows.

$$z_\#(t) = z_\#(t) - z_m(t) - \theta(t) \cdot length_\# \tag{10.3}$$

10.1.5 Case study 5, Relationship between the dynamic properties and the contact force

Observations were done while playing around using the function generator showed that the frequency at where the largest amplitude of the first rigid body mode appeared changed in relation to the contact force. This study was therefore conducted, investigating the low-frequency modes dependency of the contact force.

The sweeps were performed from 2Hz up to 16Hz and down again to 16Hz. Three different contact forces were tested, 24N, 36.5N and 42.5N. For the 24N and 36.5N tests this was done twice in each series, i.e., 2-16-2-16-2 Hz with 5 octaves per min in frequency ramp. For the 42.5N test, this sweep was not possible due to the excitement of the structure being too low, and the servo controller stopped. The test with 42.5N was therefore performed as a 2-16-2 Hz sweep with 5 octaves per min. As a result, the spectrums of the first two series are calculated using 8 windows in the Welch function, while the third is calculating using 5. This is to have a resolution of 0.0488Hz in all the three spectrums and at the same time obtain as much smoothening as possible.

10.1.6 Brief code description, Upper_Arm_Z_direction_sweep.m

Study 3 and 5 were performed with customized versions of the script. This description is for the basic script. The code takes in the acceleration data recorded by the sensors. The values are converted from mV/g to g ($9.81m/2^2$). The acceleration time series are plotted, and corresponding power spectral densities are calculated. The acceleration series can be filtered with either a lowpass or highpass filter if desired before calculating the spectrums. The code also has the possibility to remove the rigid body modes based on the equation (10.3) in the acceleration time series before calculating the spectrums. By manual analysis of the spectrums, the peaks are picked and entered into the code to estimate the mode shapes at resonance frequencies. A more detailed description can be found in the code in Appendix A, A.4.

10.1.7 Setup used in case study 3 and 5

The tests were performed with the magnet placed on the ground right behind the frame and connected to the pantograph with the wire strapped around the middle of the upper arm's lateral 30mm member. The force was measured using the rope solution used in chapter 7, when measuring the contact force, with the load cell attached to the frame of the structure and the rope being tied and untied at the same location where the wire is attached. The results of the contact force measurement in chapter 7, showed that lowering the pantograph increased the force, and it was therefore empathized to perform the measurement at the same height that the pantograph would have when connected to the magnet.

The accelerometers were primarily placed on the bellow assembly and the lower arm. Two accelerometers were placed on the plate of the bellow facing the lower arm, and one accelerometer was placed on the lower arm's lever arm, Figure 10.4b. In case study 3 one magnet was attached to the upper lateral tube right next to the wire, Figure 10.5a. In study 5, this sensor was attached to the frame feature securing the bellow to the frame, Figure 10.4c. One accelerometer was placed on the vertical beam members of the frame, holding the lower arm, Figure 10.4d. In study 3, two sensors were used on the magnet, one to give feedback to the servo controller and one was recorded with the CompactRIO, while in study 5 only one was used to provide feedback to the servo controller. In study 5, the 4 remaining sensors plus the one used on the magnet in study 3, were placed on the lower arm, Figure 10.4e. Note, in study 3 the top middle was not present.

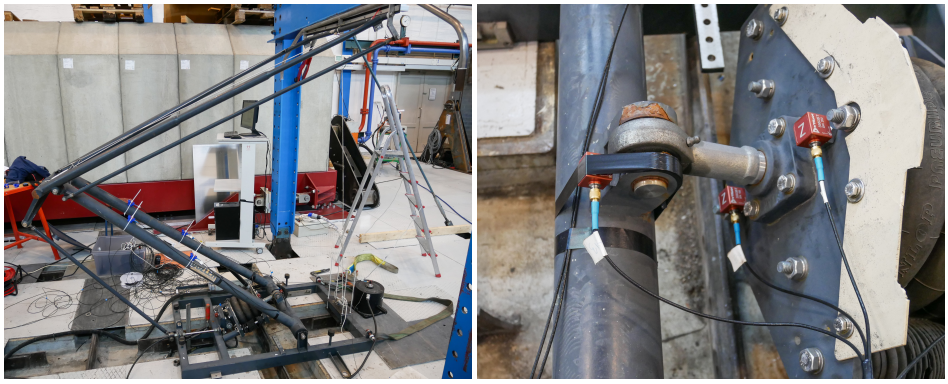

(a) General Setup **(b)** Bellow and the lower arm's lever arm

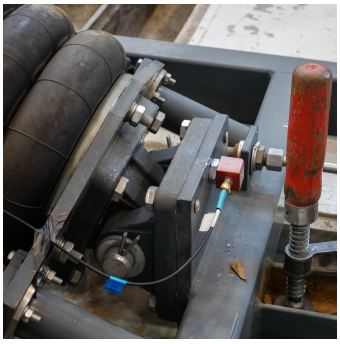

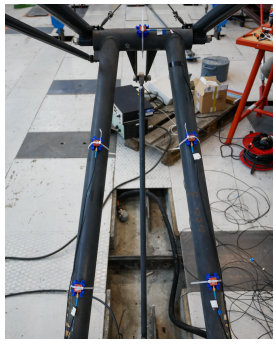

(c) Study 5, bellow attachment **(d)** Vertical frame beam **(e)** Lower Arm

Figure 10.4: Accelerometer attachment points

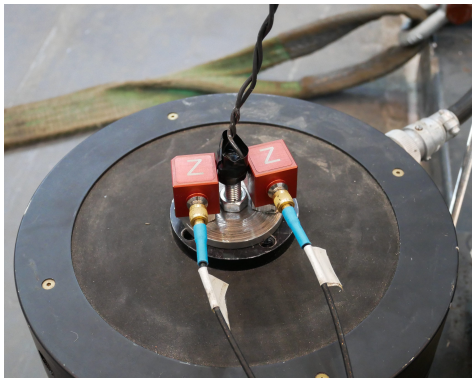

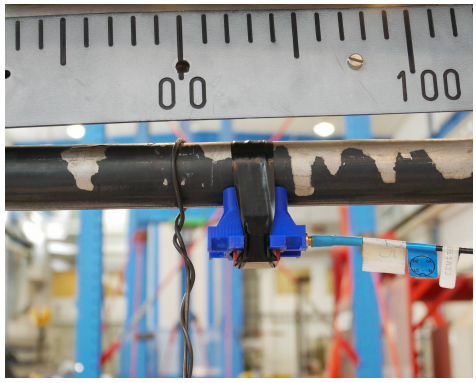

(a) 2 Accelerometers on magnet **(b)** Accelerometer at wire attachment

Figure 10.5: Study 4, accelerometer placement

10.2 Results

10.2.1 Case study 1, Effect of windowing

Figure 10.6 show that the ripples disappear from the low frequencies in the spectrum as the number of Welch windows are increased. As the spectrum is smoothened, the extreme values of the peaks diminish. The result is that using several Welch windows enhances readability, and 10 windows provide a good compromise between resolution in the frequency domain and readability. With 10 windows the frequency resolution is 0.1Hz. One thing to note is that the estimation of mode shapes becomes more resilient to comparing peaks as the extreme values are smoothened, and the ripples with extreme values and valleys are removed.

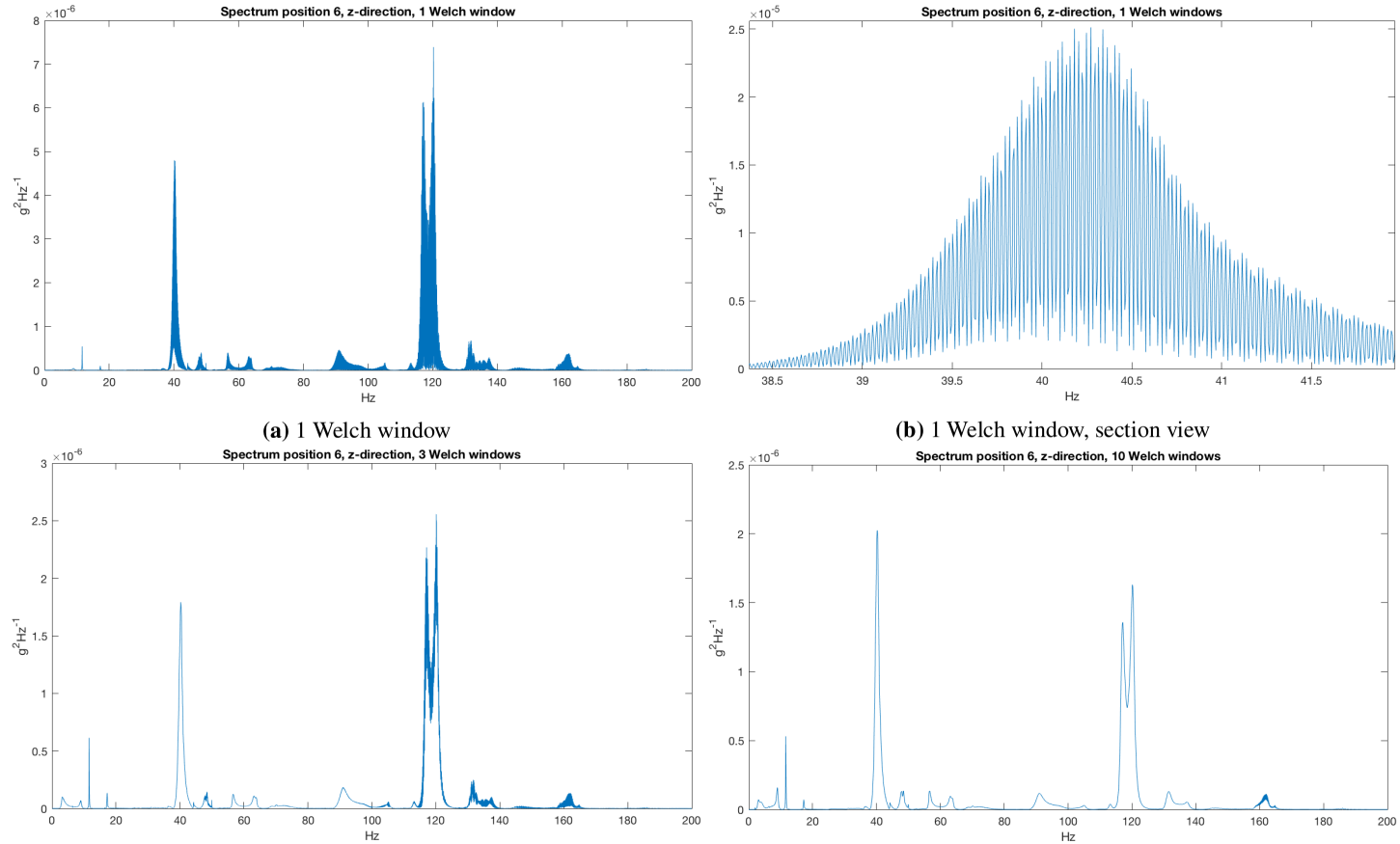

(a) 1 Welch window

(b) 1 Welch window, section view

(c) 3 Welch windows

(d) 10 Welch windows

Figure 10.6: Change in spectrum depending on number of Welch windows chosen

10.2.2 Case study 2, Variance in test series

Figure 10.7 show that the responses in the time domain are equal in all three data series. It is hard to distinguish the three time series except from a small shift along the time axis. The spectrums coincide in Figure 10.8a and the section view in Figure 10.8b is required to separate the series. The fact that all spectrums coincide indicates that the energy in all frequencies is equal in all three series.

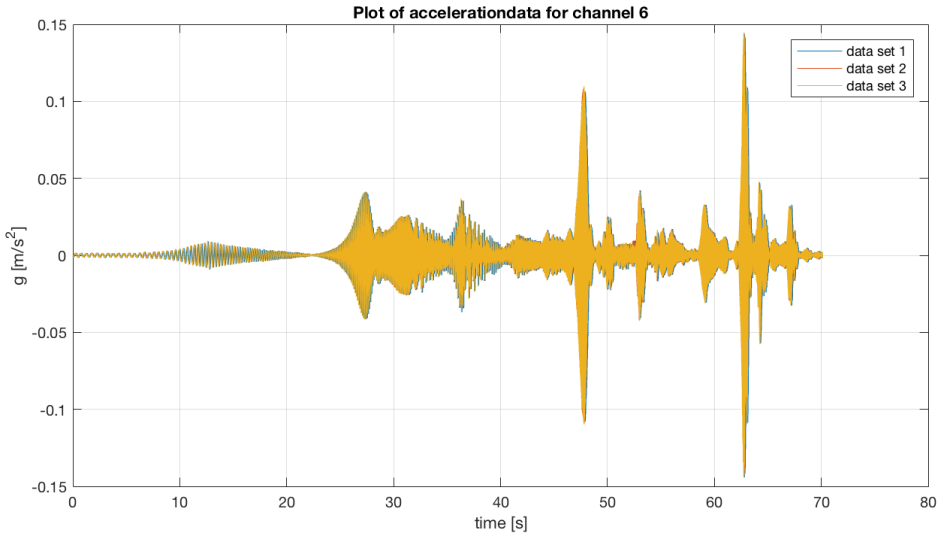

(a) Time series of channel 6

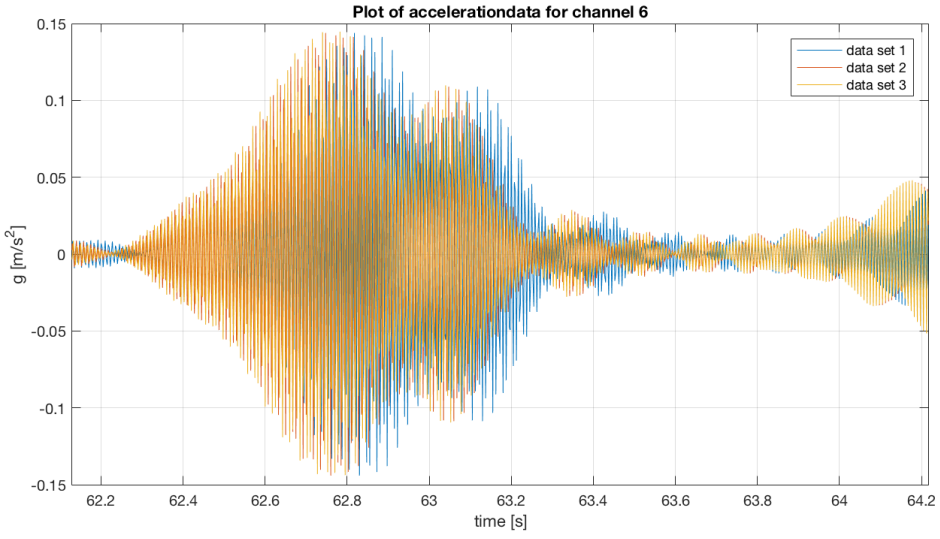

(b) Section of the time series of channel 6

Figure 10.7: The 3 time series of channel 6 plotted together

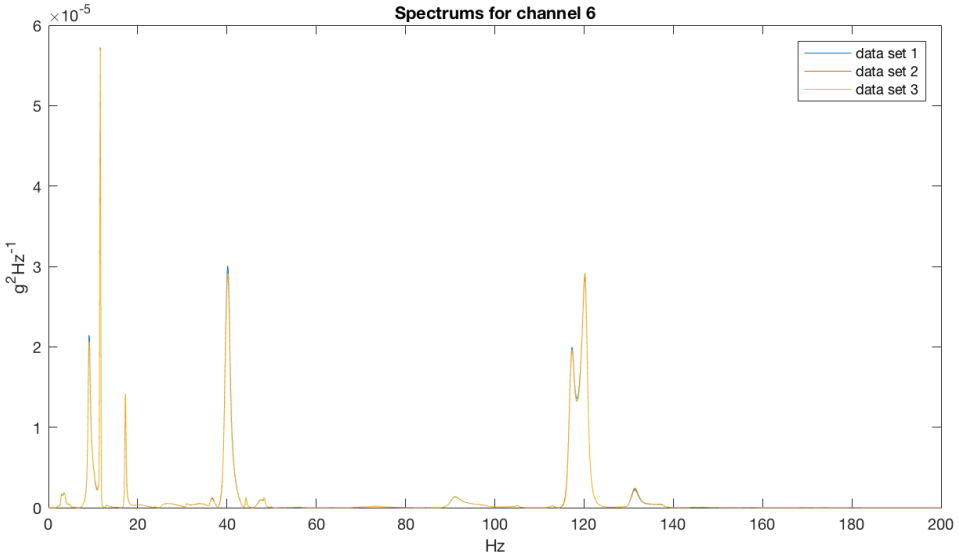

(a) Spectrum of channel 6

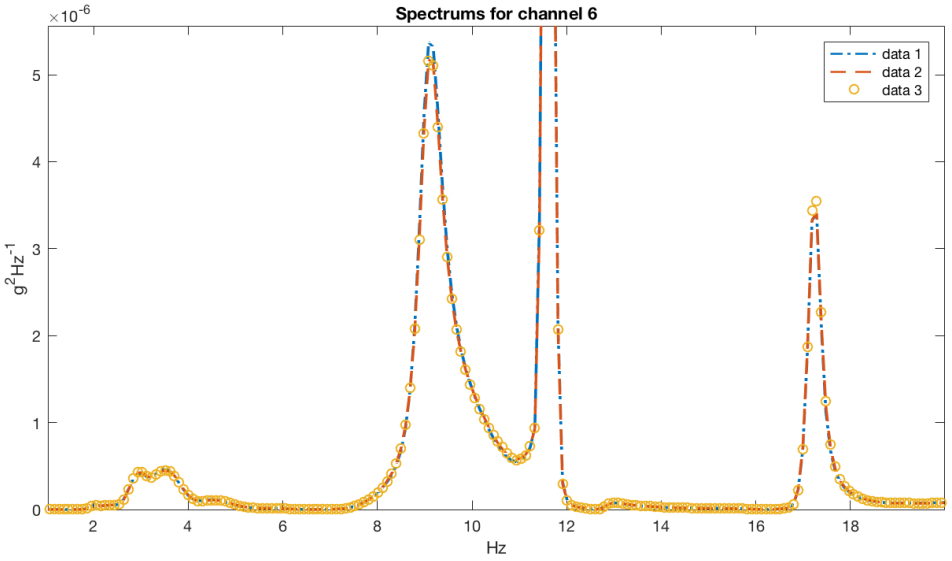

(b) Section of the spectrum of channel 6

Figure 10.8: The 3 spectrums of channel 6 plotted together

10.2.3 Case study 3, Transfer function of the wire

Figure 10.9 shows the transfer function of the wire between 0 and 20Hz for the two different contact forces and different sweeps. In Figure 10.9a to 10.9b the first peak has shifted up in frequency from 3.995Hz to 4.883Hz and the second peak has shifted from 9.375Hz to 9.814Hz. The third has only shifted 0.05Hz, which corresponds to one increment in the matrix since the resolution is 0.0488Hz.

In Figure 10.9c and 10.9d with a contact force of 43.2N, the peaks are not shifted in the same extent as with 25.7N. The first peak is shifted down one resolution unit, in the 2-195-6.4Hz sweep compared to the 2-16-2-16-2Hz sweep. The three other peaks are shifted up one resolution unit.

Comparing the change of peaks with respect to the force it can be seen that all of the peaks shifts when the force is increased in addition to new ones arising. It is therefore likely that this is the non-linear stiffness contribution from stretching the wire, and that the peaks observed are the wire and not the pantograph system.

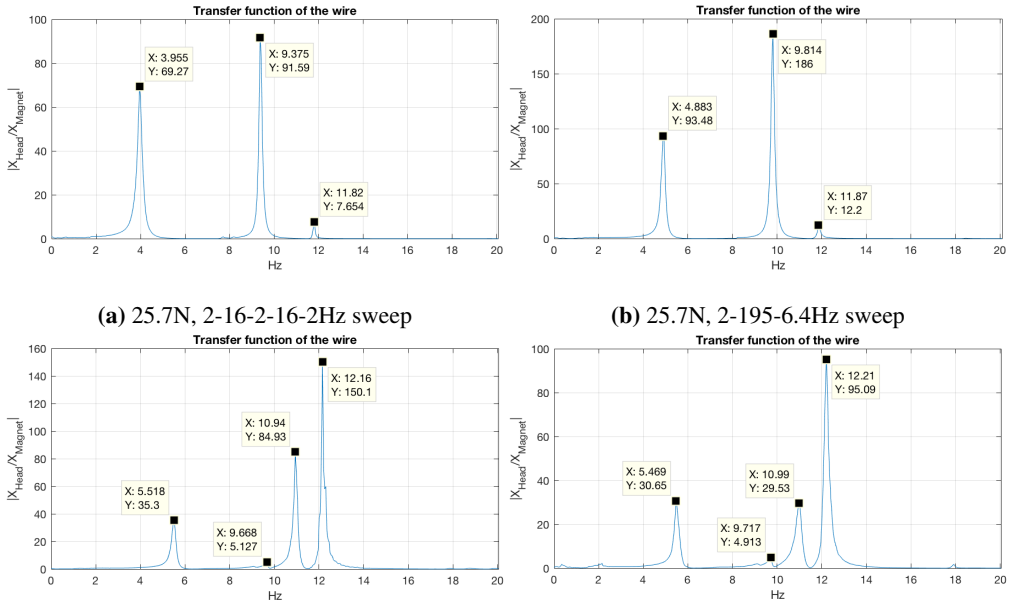

(a) 25.7N, 2-16-2-16-2Hz sweep

(b) 25.7N, 2-195-6.4Hz sweep

(c) 43.2N, 2-16-2-16-2Hz sweep

(d) 43.2N, 2-195-6.4Hz sweep

Figure 10.9: Transfer functions for the wire at varying contact force

10.2.4 Case study 4

Picking peaks in the original spectrums

Table 10.1 show the frequencies found by peak-picking and is sorted with the frequencies found in all 6 channels at the top in ascending order, followed by the ones found in 5 channels etc. The horizontal lines separate frequencies found in all 6 channels, 5 of them and four etc. The peaks for channel 5, 6 and 9 can be viewed in Figure 10.10. The spectrum for 3, 4 and 7 can be found in Appendix A, A.8.

Frequency [Hz]	channel 3	ch 4	ch 5	ch 6	ch 7	ch 9
3.516	x	x	x	x	x	x
11.62	x	x	x	x	x	x
9.082	x	x	x	x	x	
17.29		x	x	x	x	x
40.23		x	x	x	x	x
56.63	x	x	x		x	x
117.3	x	x		x	x	x
63.09		x	x		x	x
120.5	x	x		x		x
48.34		x	x			x
131.4		x		x		x
90.72	x	x				
68.26	x					
72.85					x	
105.2	x					
113.3	x					
142.7	x					

Table 10.1: Peaks picked from the channels without RBM filtering

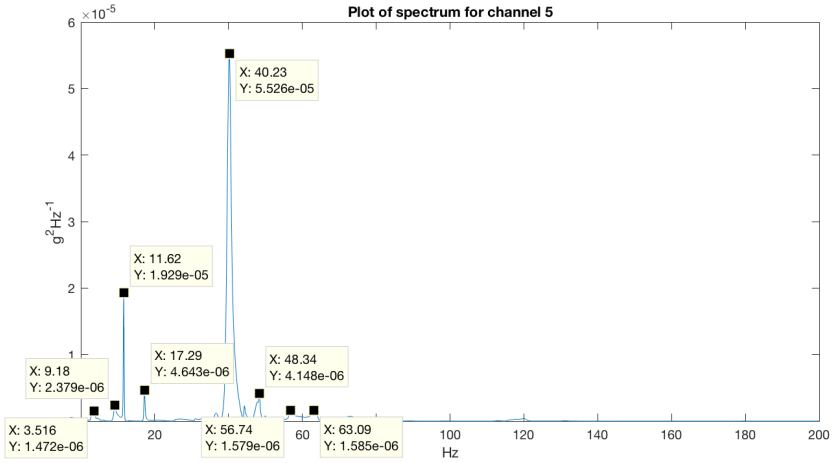

(a) Spectrum channel 5

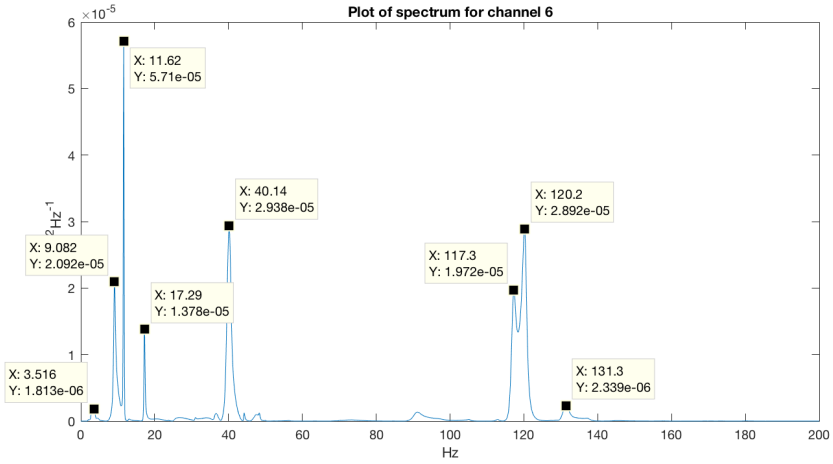

(b) Spectrum channel 6

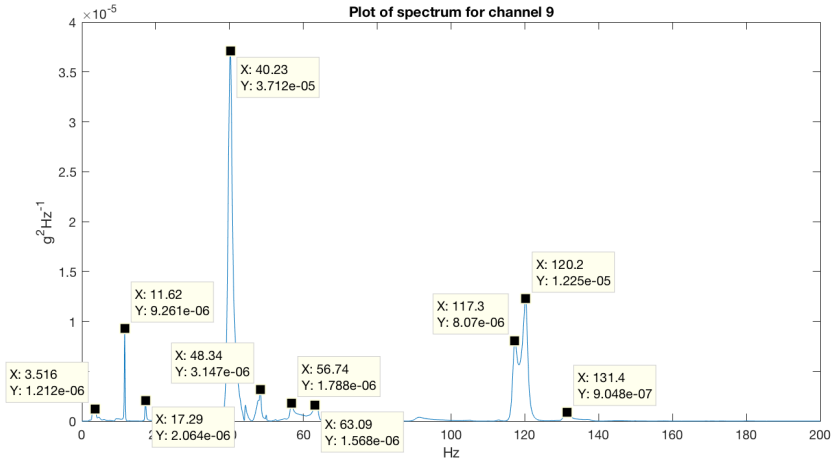

(c) Spectrum channel 9

Figure 10.10: Selection of averaged spectrums for the upper arm

The frequencies in Table 10.1 are used to calculate the mode shapes in Figure 10.11. The mode shapes are sorted in the same order as the Table. Note, the modes are normalized between 0 and 1.

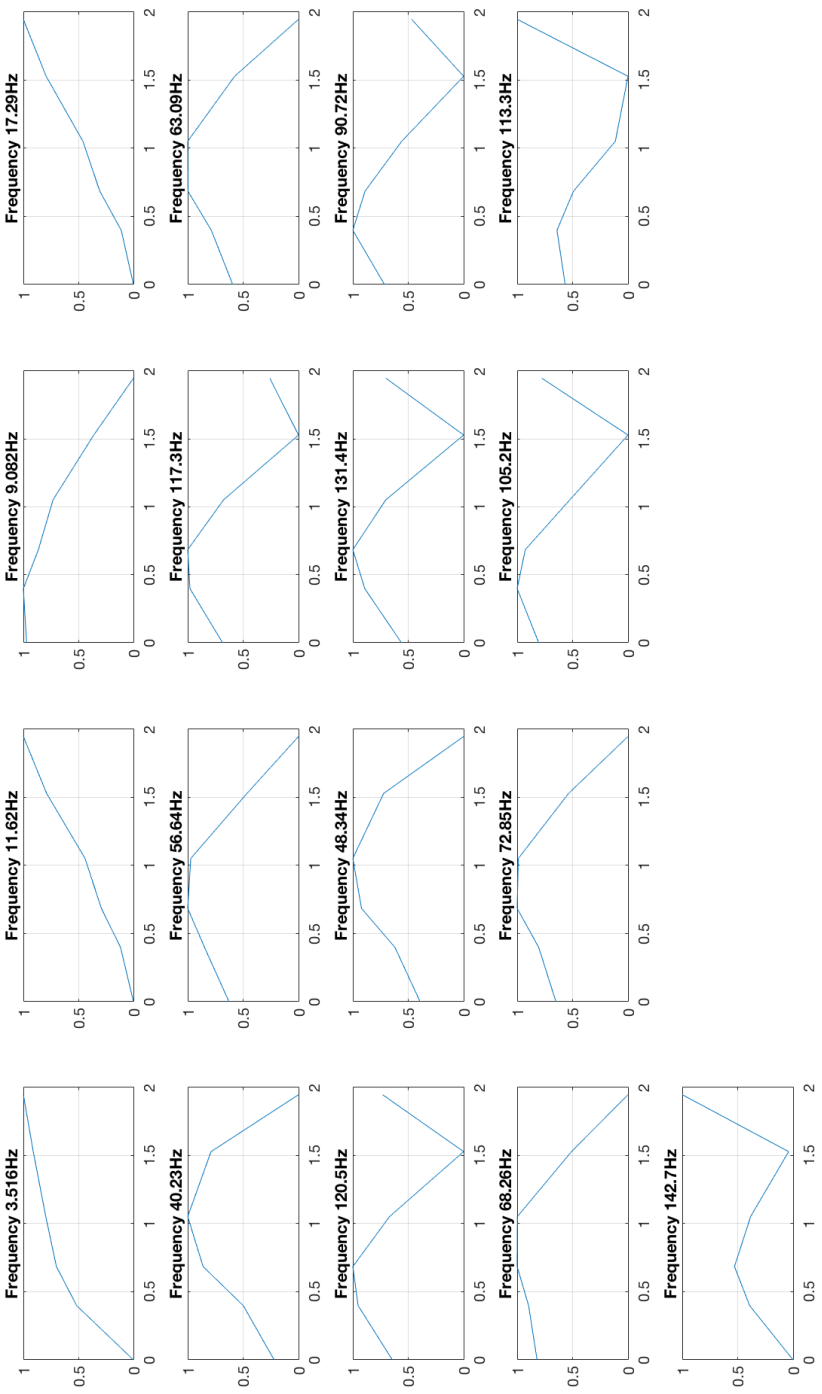

Figure 10.11: Mode shapes without RBM filtering

The right tube has only three accelerometers attached. As a result, it limits the mode shapes possible to represent. In the comparison plot in Figure 10.12 the rigid body modes and first bending modes of the tubes are presented. The plots of the right tube are not representative as for the deflection shape, but information about the phase between the right and left tube can be established. At 3.516Hz and 9.082Hz the tubes move in phase and at 11.62Hz and 17.29Hz out of phase. The first large bending mode of the upper arm occur at 40.23Hz with the two tubes in phase, and at 63.09Hz with the tubes out of phase.

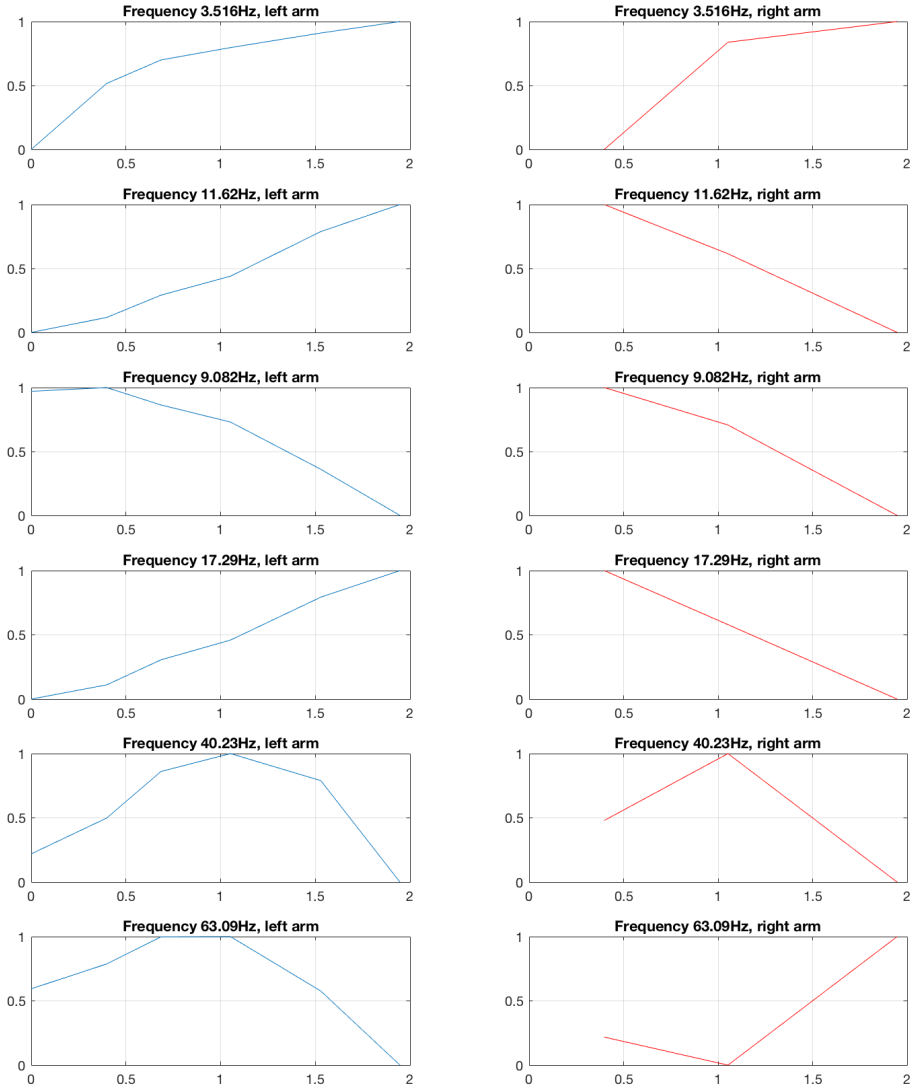

Figure 10.12: Comparison of the left and right arm

Picking peaks after RBM are filtered out

Figure 10.13 show the spectrum of channel 7, i.e. the channel on the end of the upper arm at the head, when the rigid body movement are filtered out. The energy in the spectrum is to the power of 10^{-37}, and the displacement in the channel is therefore considered removed. Table 10.2 contains the frequencies picked from the RBM-filtered spectrums and are sorted in the same order as Table 10.1, for the original time series. Figure 10.14 shows the spectrums for channel 5, 6 and 9 with the RBM-filtered out. The spectrums for channel 3, 4 and 7 can be found in Appendix A, A.9. Figure 10.15 shows the mode shapes calculated at the frequencies in Table 10.2.

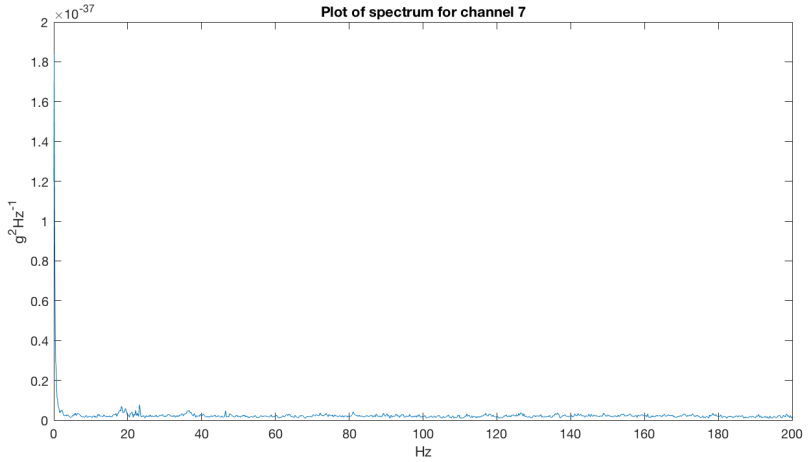

Figure 10.13: Spectrum channel 7

Frequency [Hz]	channel 3	ch 4	ch 5	ch 6	ch 7	ch 9
9,082		x	x	x		x
40,23		x	x	x		x
48,34		x	x	x		x
63,09		x	x	x		x
117,3		x	x	x		x
56,74		x	x			x
72,85		x	x			x
120,1		x		x		x
131,3		x		x		
91,21		x				

Table 10.2: Peaks picked from the channels with RBM filtering

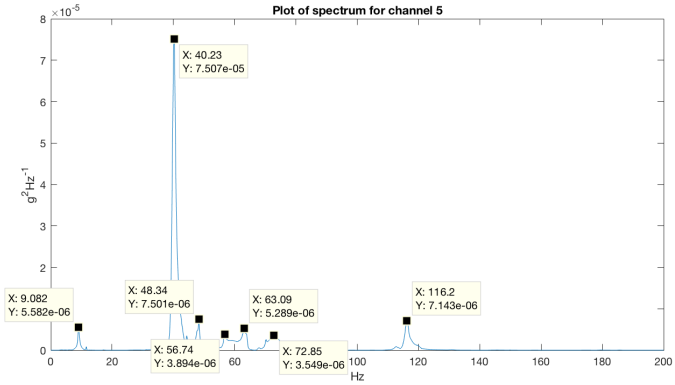

(a) Spectrum channel 5

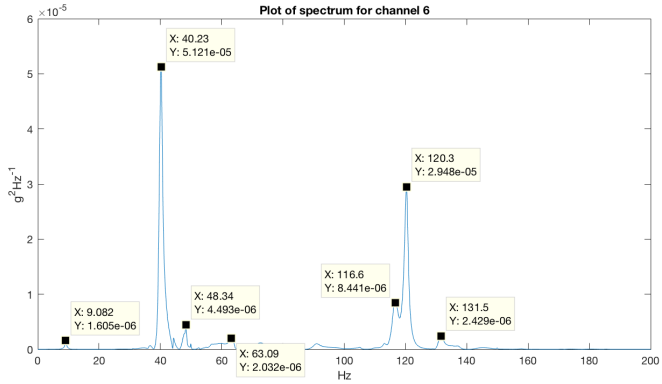

(b) Spectrum channel 6

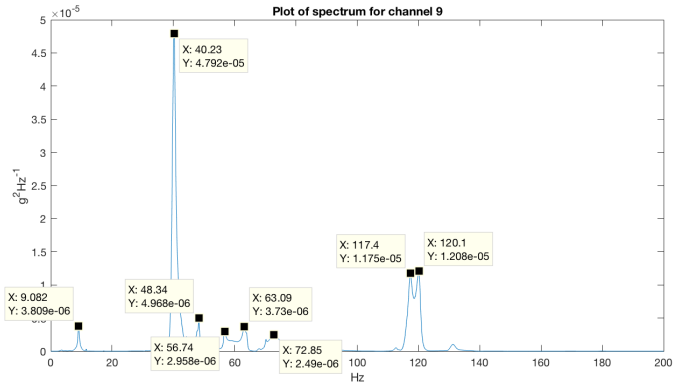

(c) Spectrum channel 9

Figure 10.14: Selection of averaged spectrums for the upper arm when RBM are removed

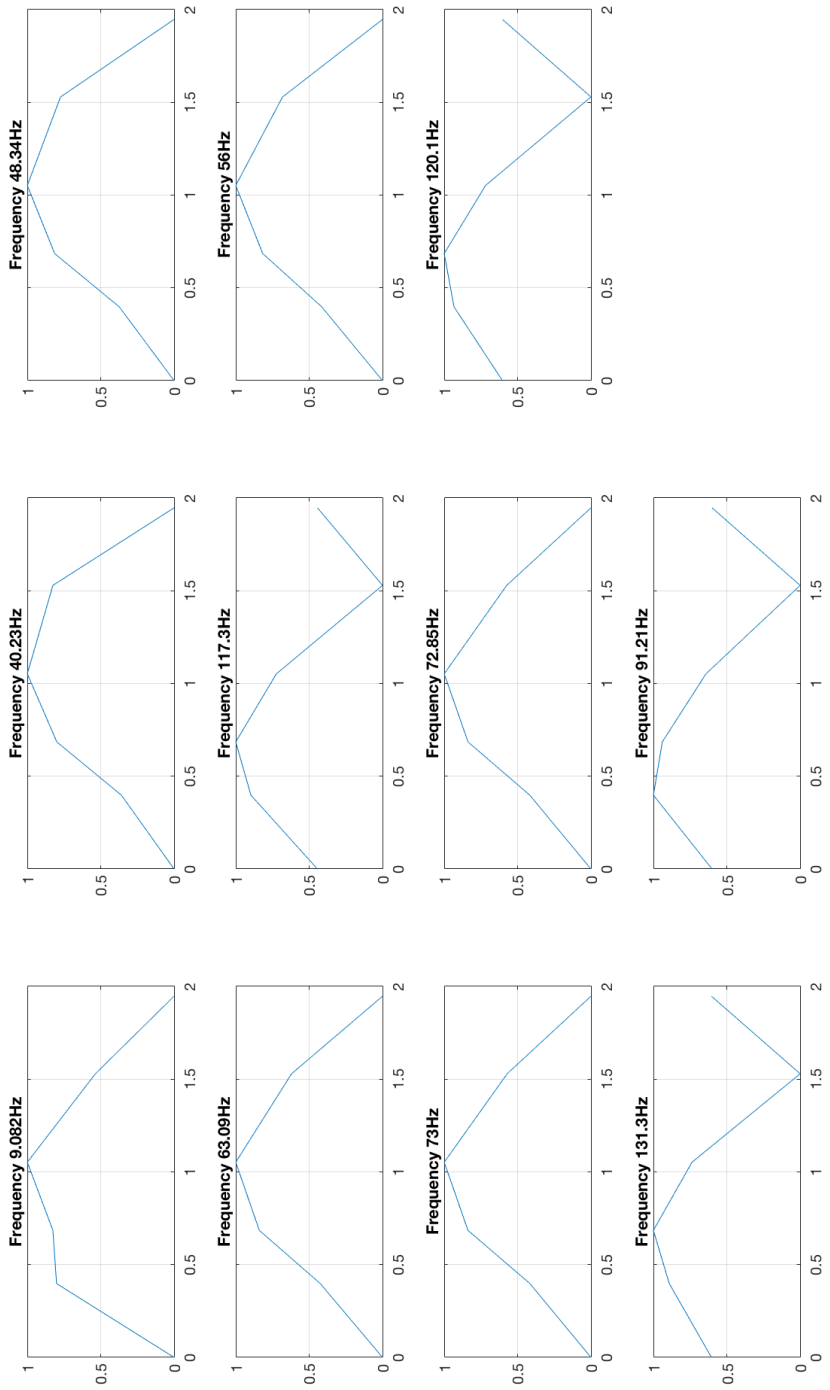

Figure 10.15: Mode shapes with RBM filtered out

Comparing the shapes estimated with and without RBM filtered out

Figure 10.16 and 10.17 show the comparison between the mode shapes calculated from the original series and the RBM-filtered ones. In the plots of the original shapes, a red line is plotted from the left-hand side to the right one illustrating the rigid body movement in the mode.

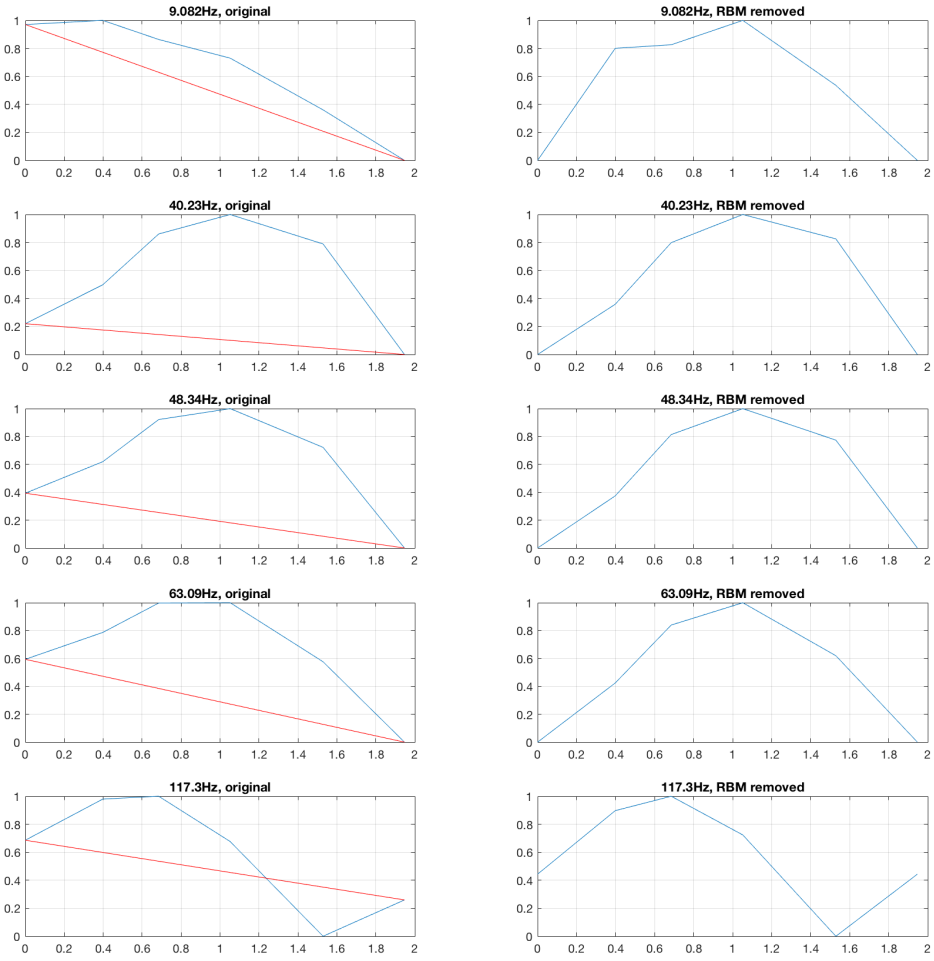

Figure 10.16: Comparison of modes estimated with and without RBM filtered out, part 1

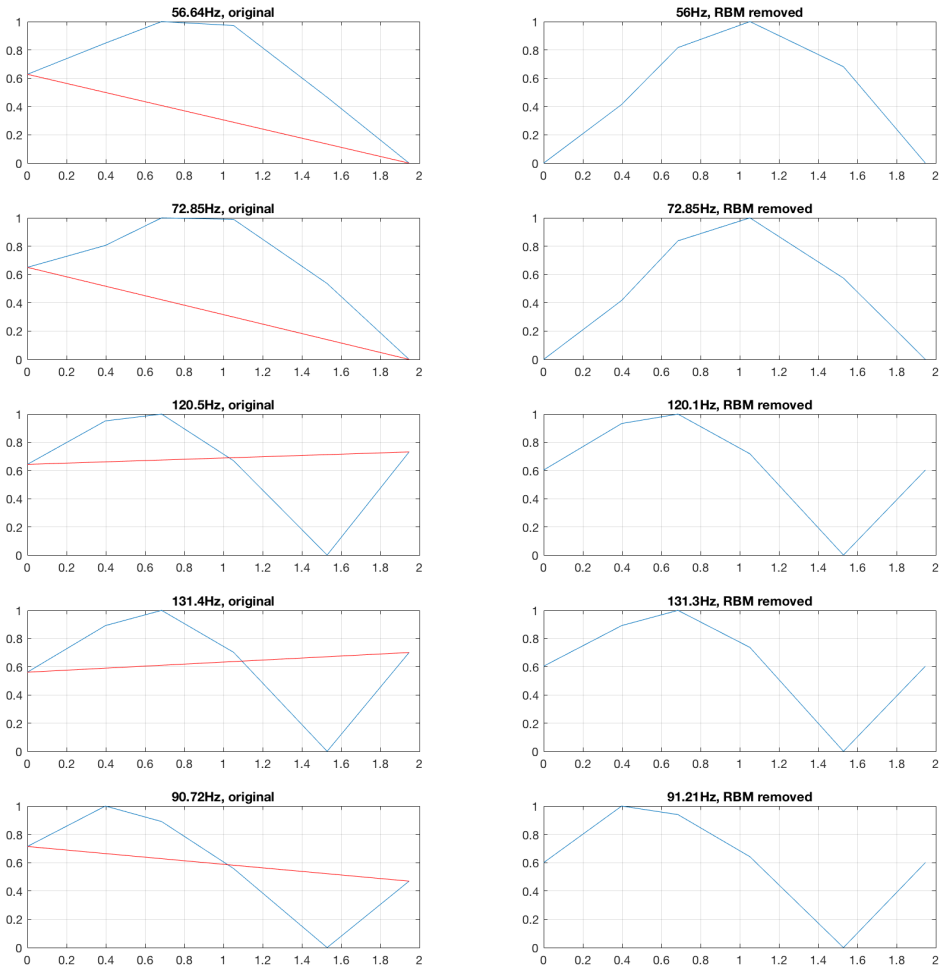

Figure 10.17: Comparison of modes estimated with and without RBM filtered out, part 2

10.2.5 Case study 5, Change in dynamic properties depending on the contact force

The natural frequency of the first rigid body mode at around 3Hz, where the whole structure is moving vertically, shifts when the pressure in the bellow is increased. With the bellow pressure at a level resulting in a contact force of 24N, the natural frequency of the first mode was 2.979Hz, see Figure 10.18a. Increasing the pressure, obtaining a contact force of 36.5N the natural frequency was increased to 3.174Hz, Figure 10.18b, and the whole way up to 3.857Hz when the contact force was increased to 42.5N, Figure 10.18c.

Another effect of increasing the contact force was the knee bending mode at around 9Hz was separated into two peaks. With a contact force of 24N, the peak was at 8.984Hz before it splits up into two dominant peaks with a small peak in between with a contact force of

36.5N. With 42.5N the left of the two peaks was shifted to a frequency of 9.277Hz and the right peak all the way to 10.16Hz. From the three spectrums presented, the natural frequencies of the modes increases as the pressure increases and in addition a peak at 7.129Hz appears between the modes with the contact force of 42.5N.

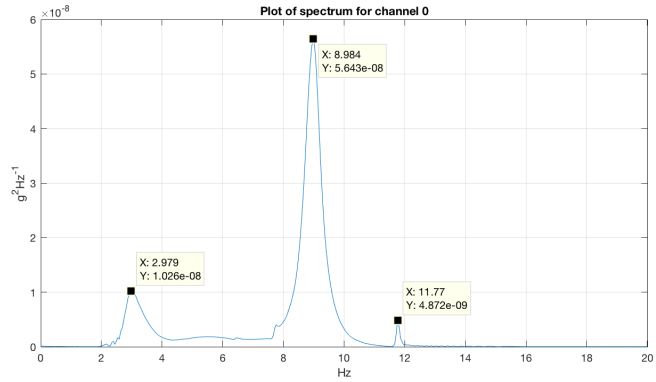

(a) Spectrum with a contact force of 24N

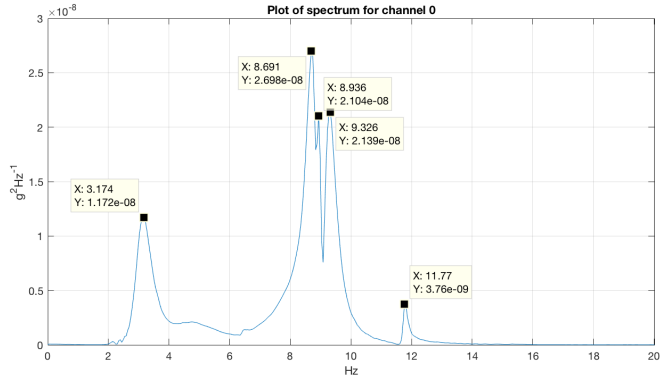

(b) Spectrum with a contact force of 36.5N

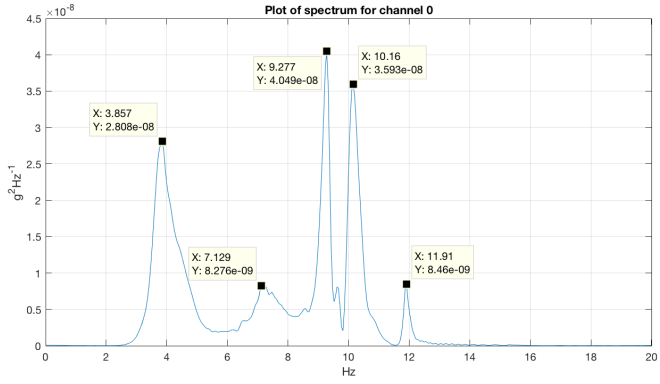

(c) Spectrum with a contact force of 42.5N

Figure 10.18: Spectrums for the bellow mode with varying contact force

10.3 Discussion

10.3.1 Case study 1

When applying windowing, the extreme values was reduced. The effect of this when comparing peak amplitude in the operational shape identification is assumed to be correct and in addition more resilient to small frequency deviations in the numerical arrays. The different channels can have small shift and the peak be at the next index. If the spectrums then contain ripples, it is possible to compare a peak from one spectrum with the valley of another and get large errors.

10.3.2 Case study 2

With the series cut to match in length, the fact that they coincide so well that they do is a bit surprising but a very pleasant one. From case study 3 the effect of altering the wire in the experiment is an uncertainty, and if this is the cause of altering the natural frequency observed for the first peak or not is unknown. On the other hand, multiple series recorded with the same setup provides the exact same response. The lab setup has a good repeatability when the boundary conditions are the same, but the effect of altering the boundary conditions when installing the test setup, primary with respect to the wire interaction and its properties, should be further investigated.

10.3.3 Case study 3

When the contact force was measured with the rope, the wire to the magnet was still attached. It was hard to ensure that the wire did not transfer any forces. When bending it, it caused the force to vary with up to 5N. So the forces recorded could deviate some from the actual forces applied by the bellow on the system.

The wire has multiple defined peaks in the range from 0-12Hz. Above 12 Hz there is no response until suddenly at 110Hz there are some resonances again. This has not been included since the focus of the dynamic analysis performed have primarily been on the response in the range from 0 to 70Hz.

The observed shift of the first natural mode with a contact force of 24.7N in Figure 10.9 could be caused by the wire being straightened when doing a control measure of the contact force between the 2-16 sweep and the 2-195 sweep. By bending the wire, the local stiffness at the ends, and bends along the span could possibly shift the natural frequency of the wire.

The peak appearing at roughly 9.7Hz in Figure 10.9c and 10.9d could be the bending knee mode of the pantograph. The peak of the bending knee mode can be seen in Figure 10.18c, where the peak right above 9Hz has split up into two clearly defined peaks. As pointed out, the force in this experiment could be higher than recorded, thus moving the peak observed at 9.277Hz for the bending knee mode in Figure 10.18c up to 9.7Hz.

10.3.4 Case study 4

With the observations described in chapter 9, section 9.8, the response found can be evaluated. The first rigid body movement caused by the bellow is found at 3.516 Hz. Both the longitudinal tubes of the upper arm are moving in phase, Figure 10.12. Using the RBM-filter on the acceleration data this frequency disappears from the spectrums. This

coincides with the observations of the first mode observed for the structure. The fact that the frequency is higher than the one specified under in section 9.8.1 is discussed under case study 5.

The mode at 9.082Hz is a combined mode. As observed in section 9.8.3 the lower arm and the upper arm are both moving in the vertical direction but in counter phase. From the mode shapes estimated in Figure 10.12 the mode consists of a rigid body mode combined with a deformation along the tube element. When applying RBM-filtering the mode still exist in the spectrums, Figure 10.14, and the mode shape is curved, see Figure 10.16. The response is therefore interpreted as the rigid body mode combined with a deflection mode of the upper arm.

In Figure 10.12, at 11.62Hz the two tubes are in counter phase. This corresponds to the twisting mode observed at 11.5Hz in section 9.8.4. When applying the RBM-filter this frequency disappears from the spectrums. The mode is therefore considered a rigid body mode of the upper arm like the first mode.

At 17.29Hz the upper rod hits its first natural frequency and starts to vibrate violently as observed in section 9.8.5. This is transferred to the upper arm as a RBM-mode with the same characteristics as the 11.62Hz mode. When applying filtering the mode is removed from the spectrums like the mode at 11.62Hz.

The mode observed at 40.23Hz is not a perfect sine shape as expected for a beam. There are multiple reasons why this may be the case. At the top end of the tubes, the head is attached acting like a lumped mass on the tip of the beam. In addition is the upper rod is connected to the head and could introduce some resistance in this mode. Lastly is the change of cross section along the tubes and a change in angle of the 30mm tube. The curvature seems to tighten towards the right in the plot, where the 30mm tube is, this is to be expected as the stiffness is lower there compared to the thicker profiles the left-hand side in the plot. The mode at 63.09Hz have a similar shape to that of the tube at 40.23Hz, but the right tube is negatively correlated to the left arm this frequency.

Generally, for the mode shapes estimated with this method, it is hard to conclude with any of the modes other than those observed for the structure in chapter 9, section 9.8. This method finds many peaks in the structure, and they are not necessarily very closely spaced, but the shapes are close to identical. Examples of this is in Figure 10.16 and 10.17, The mode shape estimated for the structure at 117.3Hz and 120.5Hz is similar. What sets them apart is the original series having a positive or negative RBM-contribution. What causes the two modes to have the same shape, but two distinct peaks can be multiple things. Since the cross-section being a tube, the axis the response occurs in is hard to predict. The responses at 117.3Hz and 120.5Hz can be in two different planes, rotated about the tube. The stiffness can be different in the two planes. Thus the response will be seen in the two different directions at different frequencies. The chance of both the responses giving a contribution in the z-direction is high, and both will then have the same shape. As the whole structure uses circular cross sections, the measurements should ideally be performed in two axes, and the amplitudes of the responses should be calculated such that they can be compared. The method of operational shape identification defines one of the cross-correlations to be unity, to estimate the rest as a ratio of this.

The method of removing the RBM contribution in the time domain translates well into the frequency domain, and the mode shapes of the structure are the same in the two plots, only straightened up. The method successfully removed the 3.516Hz, 11.62, and 17.29Hz frequencies from the spectrums. The problem is to say with certainty the frequency of the upper arms bending modes and their shapes.

10.3.5 Case study 5

From the spectrums for the bellow with the varying contact force in Figure 10.18 it is clear to see that the peaks are shifting up in frequency as the force increases in the bellow. The first natural frequency corresponding to the RBM bellow mode is shifting up without any special effects while the bending knee mode splits up into two peaks. This could be two modes in the structure that separates with respect to frequency as the bellow force is increased.

10.4 Conclusion

10.4.1 Case study 1

Windowing works and give the wanted benefits. It is therefore used in the other studies.

10.4.2 Case study 2

The series recorded are equal in both time and frequency domain. It is concluded that performing the analysis in ARTeMIS with only one series is fine.

10.4.3 Case study 3

The wire has its own natural frequencies. These shift as the force is increased and can amplify the response of the structure if these coincide. The response of the structure at given forces must, therefore, be seen reviewed with the natural frequencies of the wire in the back of the mind.

10.4.4 Case study 4

The first modes observed and filmed in chapter 9 can be found, and the response coincides with the observations performed. The responses of the upper arm above this frequencies are difficult to prove with high certainty. The highest mode we can establish with any degree of certainty is the bending in counter phase at 63Hz.

10.4.5 Case study 5

The bellow and the first mode of the structure, as well as the bending knee mode are highly dependable on the pressure in the bellow. As this acts as a spring in the system, an increased pressure resulting in a higher stiffness increases the natural frequency of the modes. Ideally, the pantograph should be tested with a force of 55N to find the natural frequency under normal operation.

10.4.6 Future work

As future work, the cause of the separation of peaks in the spectrum in case study 5, where the bending knee mode is separated, should be investigated. Further, a test setup allowing for testing with higher contact forces should be found. The dependency of the contact force in these studies implies that this is crucial to obtain the correct system response.

11 — Modal Analysis in ARTeMIS Modal

In this chapter, the method, results and conclusions from a modal analysis of the pantograph using the ARTeMIS Modal software are presented. The theory behind the calculations used during the modal analysis is presented in chapter 3. First, the methods used during the processing in the software and arguments connected to the test setup will be presented. Second, a short analysis of the pantograph based on a coarse measurement mesh is presented. Third, the results from the modal analysis based on part by part calculations will be presented. Fourth, the most crucial modes will be evaluated. Fifth, a discussion about the validity of calculations, results, sources of error and estimators used. Finally, the conclusions are drawn from the analyzing process and the results of the modal analysis.

11.1 Method

ARTeMIS Modal Pro has been used to process the measurement data from frequency sweeps performed in the lab. This section presents the procedure followed in the signal processing performed with the software. To set up the estimations, it is required to establish the measurement geometry, detrending of the measurement data and setting parameters to be followed in the calculation before using the different estimators available in the software. Validation is done using methods available in the software in addition to validating what modes corresponds between the different part by part test setups. The measured time series of the acceleration, are recorded during a sweep from 2Hz up to 195Hz then down towards 2Hz again. However, as mentioned in 9 most of the sweeps stopped at about 5Hz. To evaluate the sweeps, the frequency content is shown with a short Fourier transform plot of a selected measurement channel for each setup.

11.1.1 Establishing geometry of measurement nodes

The nodal coordinates and vectors of the measurement directions used in ARTeMIS were collected from the Solid Works model of the pantograph. In each part by part analysis performed the number of nodal coordinates utilized is limited to the measurement points of the setup and nodes crucial to present the geometry of the entire part. The sparse nodal geometry leads to simplified geometrical shapes but assures representation of the measured data in most visible nodes.

11.1.2 Preparation of measurement data

Before importing the time-series to ARTeMIS they have been transformed to gravitational acceleration from the raw data delivered by the CompactRIO. When importing the measurement data one simply defines the sampling frequency and unit. Then the measurements are assigned to the nodal coordinates along with the directional vectors of the accelerometers. A tabular presentation of measurement directions relation to the global axis and figures with nodes are presented for each part. If some of the measurement data of the

particulate setup does not correspond with the part of the pantograph being analyzed, it is deleted.

11.1.3 Setting up the data processing

When setting up the calculations in the data processing one needs to choose the appropriate modal order of the parametric estimation techniques. This is done to ensure that the algorithm is comprehensive enough to capture the parameters of the system. Another option is to decrease the considered frequency domain of the parametric estimation. This is done in deciding the decimation considered during the calculations. Hence, reducing the effective Nyquist frequency. Modes at higher frequencies was mainly estimated using FDD techniques, because these modes were assumed to be lightly damped. Making enhanced FDD estimation sufficient.

11.1.4 Modal estimation

Estimations of the modes have been done both using automatic techniques with given criteria, such as maximum damping or complexity present in the modes or uncertainty of the estimates, and manual peak-picking with following manual consideration of mode shape and estimated properties. The estimations from ARTeMIS is either based on FDD techniques or SSI techniques, of which only the FDD techniques allow adding modes through peak-picking. Which means the only way of changing the estimation of the SSI techniques is to alter the acceptance criteria for stable modes in the analysis. This was done in post-processing, when targeting the highly damped modes at low frequencies.

11.1.5 Modal Validation

To validate the different estimates MAC is used both between modes established from the same estimator to ensure they are separated and to compare modes estimated from two different estimators. The second way the modes have been validated within the ARTeMIS software is through visual inspection of the mode shapes. There has also been performed manual validation of which modes from each setup correspond with each other based on the coarse mesh analysis.

11.2 Results

The results of a coarse mesh analysis are presented initially. Then the main results of the modal analysis will be presented part by part. Before the most prominent modes estimated form the analysis are given in the mode by mode section.

11.2.1 Coarse Mesh Analysis

Initially, a coarse mesh analysis was performed to establish the global modes, and give some perspective as to where local modes originate. This gave crucial information as to what to investigate further. The initial estimates from these test are only used to connect the modes, further investigated in the part by part estimations. The results from this analysis are presented in attached files. However, when reading these results note that the estimators have not been managed properly, and therefore give poor damping estimations, and in some cases, the modal vectors might be effected by nearby modes. This is because some of the modes occurring in the pantograph require measurements in multiple directions to be properly separated. Modes found in this initial analysis are shown in Table 11.1. The measurement nodes and directions during this analysis are indicated in Figure 11.1.

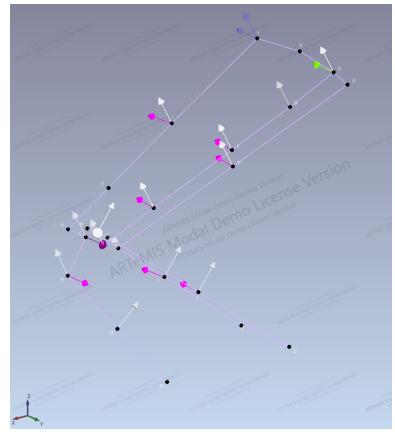

Figure 11.1: Coarse mesh geometry with measurement directions

As the results from this analysis are only used to connect further investigated behaviour the quality of the measurements has not been assessed. Therefore the results should only be interpreted in connection with the further analysis presented in the following section 11.2.2.

Figures of some mode shapes based on this analysis will be shown in the section 11.2.3. However, the further estimation for each mode is done using data from the setups form the individual parts. Since, further description of the dynamic behaviour requires a finer mesh.

Figure 11.2 shows a MAC plot from the coarse mesh estimation of a measurement series performed with a contact force of 40N and a sweep from 0 to 20Hz. Other mac calculations have been used during the analysis to arrive at the interpretations in the next section. The mode present at 13.2 was later assessed to be a false mode, and the mode present at 16.4Hz is believed to be mode in the wire connecting the pantograph and the magnet used for excitation.

Table 11.1: Modes found using a coarse mesh and multiple time series with the enhanced FDD technique

Dominating part, motion description	Frequency [Hz]	Damping [%]	Complexity [%]
RBM, bellow	3.532	12.012	3.567
UA, lateral	6.445	0	41.188
Knee, vertical	8.893	3.137	2.095
UA, twist	11.608	1.401	0.95
UR, firts mode	17.188	0	0.157
Knee, lateral	22.039	0.528	28.684
UA, vertikal bending phase	40.614	2.064	0.913
UA, lateral bending c-phase	48.828	0	1.485
UA, bending tuned mass	62.924	0.802	23.799
Ua, bending tuned mass	67.328	0.503	21.382
Unidentified	70.194	0.291	73.795
UA, bending uncertain plane	113.584	0.689	75.329
UA, bending uncertain plane	117.379	0.335	71.679
UA, higher order bending lateral	132.439	0.348	57.559
UR	154.319	0.982	9.065
Unidentified	176.367	0	29.541
Unidentified	181.055	0	57.643
Unidentified	199.709	1.909	3.12

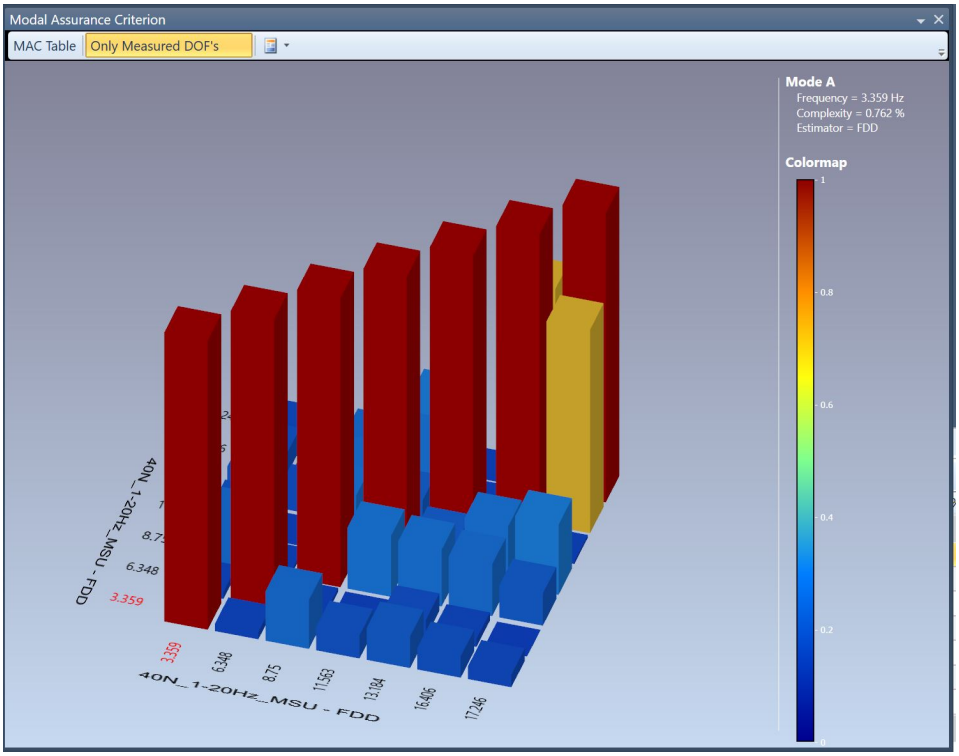

Figure 11.2: MAC values for the modes detected in the coarse mesh analysis below 20Hz

11.2.2 Part by part Calculations

To be able to determine the dynamic properties of the pantograph on a detailed level the final measurements have been performed part by part. In addition to enabling deduction of mode shapes and to determine if modes are locally conditioned. The presentation of these results will focus on the time series used, the spectral densities estimated, the modes estimated and the properties estimated from SSI-techniques. In reading the results keep in mind that, due to some change in the contact forces delivered by the system during testing and the alteration of mass distribution in the system due to the weight of the sensors, the different setups measures incrementally different systems.

Head (H)

Figure 11.3 shows the first head mode at 25.9 Hz occurring in the pantograph and Figure 11.5 a table describing the measurement directions and locations on the pantograph head. Unfortunately, channel 5 only recorded noise, this is the channel measuring movement in x-dir in the middle of the head. Figure 11.4 shows the accelerations series for channel 1-4. From closer inspection of the acceleration plots, it is clear that the movement on the tip of the head has about the same magnitude in both vertical and x-direction. The plot of channel 4 shows the vertical accelerations close to the head supports giving information about the rigid head motions.

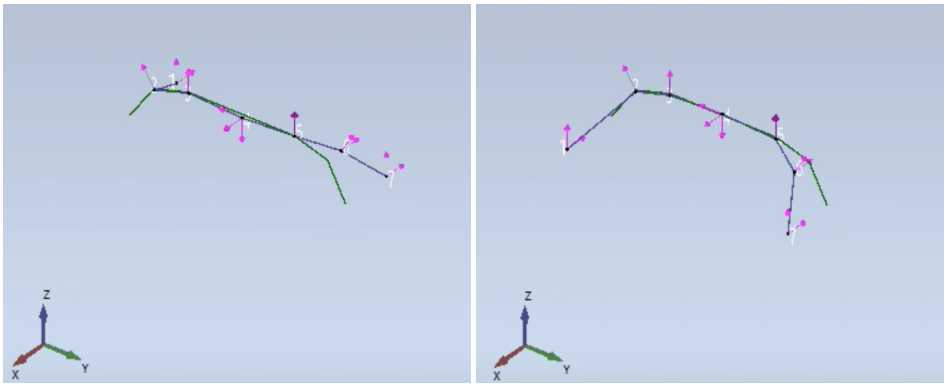

(a) Head mode estimated at 25.97Hz, with node numbering

(b) Head mode estimated at 25.9Hz, with node numbering

Figure 11.3: First head mode detected at 25.9Hz

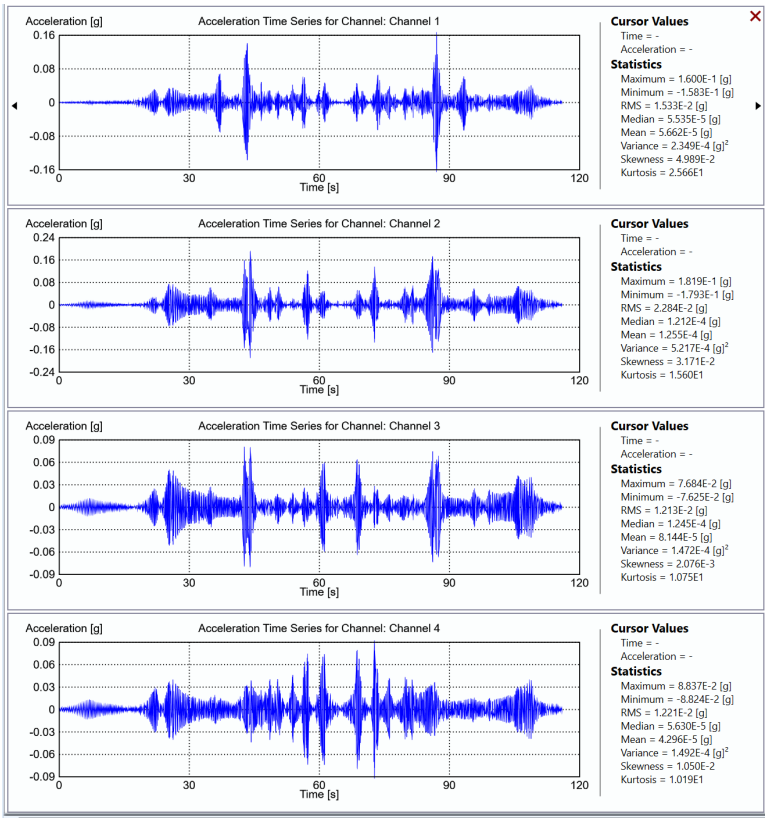

Figure 11.4: Selected time series from the head setup

From the plot of the short Fourier transform of channel 1 in Figure 11.6, three head modes can be identified. The previously mentioned mode at 25.9 Hz, one just below 40 and one at 104 Hz. The short Fourier transform plot also gives some idea of the sweep during the time sample and indicates that the measurement setup is able to transfer most of the frequencies.

Head	Node nr.	X	Y	Z
Ch 1	1	-1	0	0
Ch 2	1	0	0	1
Ch 3	2	0	-0.53	0.848
Ch 4	3	0	0	1
Ch 5	4	1	0	0
Ch 6	4	0	0	-1
Ch 7	4	0	-1	0
Ch 8	5	0	0	1
Ch 9	6	0	0.53	0.848
Ch 10	7	-1	0	0
Ch 11	7	0	0	1
Ch 12	6	-1	0	0

Figure 11.5: The Table shows measurement channels relation to geometrical nodes in the head setup

In the singular values of the spectral densities plot shown in Figure 11.7 it is clear that the second and even more so in the third singular value line the effects of, what is assumed to be, noise from the channel without measurements to some degree compromise their value when interpreting the spectral densities. Luckily the first singular value line seems to contain the important parts of the spectral densities. The first five peaks of the first singular value correspond well with the first five modes of the system. Higher resolution plots are found in the data for the upper arm. Additionally, it is somewhat clear that there are at least three modes present at about 40Hz. The remaining peaks are connected with modal behaviour originating in other parts of the pantograph.

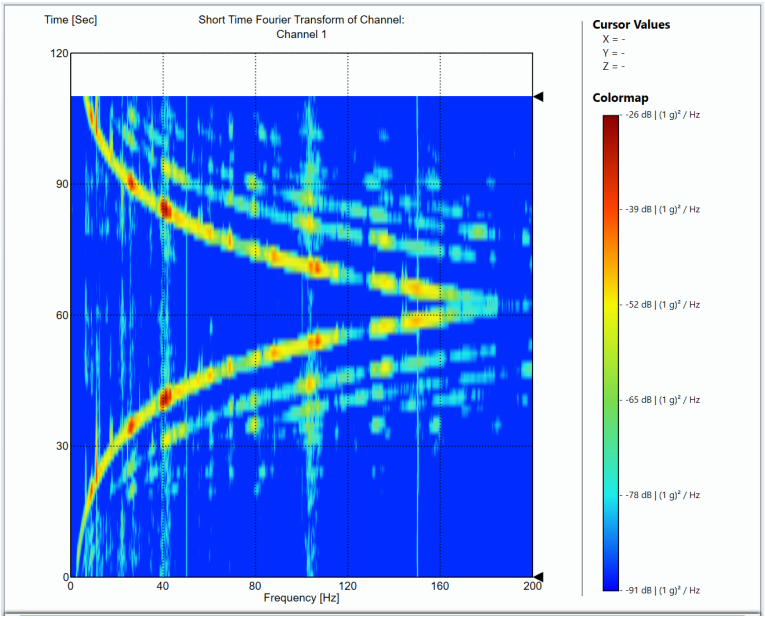

Figure 11.6: Short Fourier Transform plot for channel 1 from the head setup

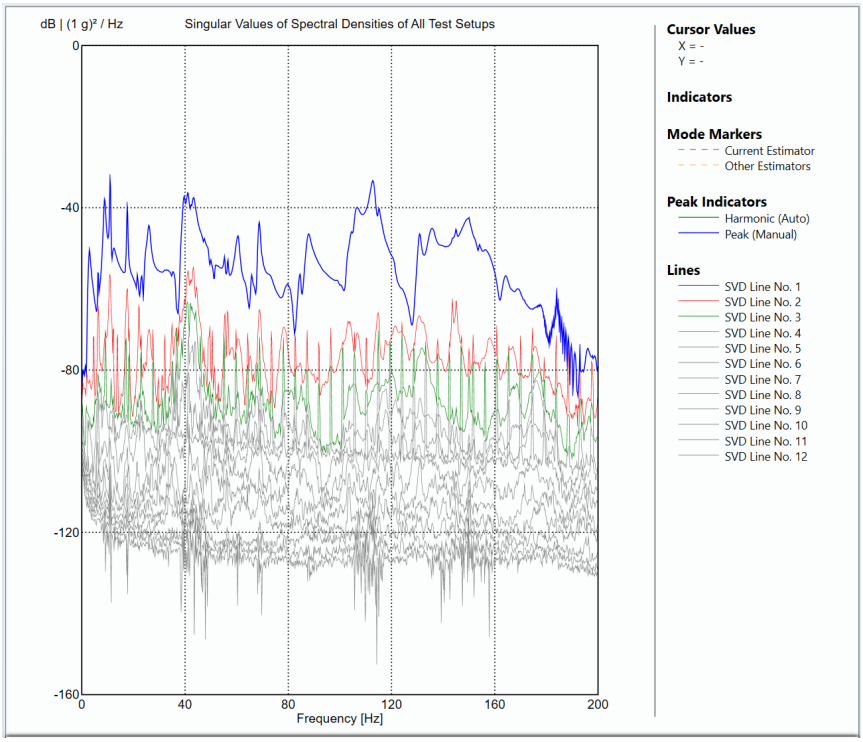

Figure 11.7: Singular Values of Spectral Densities of Head setup

Table 11.2 show the modes found in the pantograph head. In reading these results keep in mind that some of the dynamic properties of the pantograph head itself, in this particular setup, are very sensitive to the added mass of the sensors, supports and wires.

Dominating part, motion description	Frequency	Damping	Estimator	File name
RBM, bellow	3.088 Hz	12.21%	CFDD	3Hz.avi
UA, lateral swing	6.305 Hz	7.115%	SSI-UPC	6.25.avi
Knee, vertical	9.057 Hz	5.7%	SSI-UPCX	8.8.avi
UA, twist	10.979 Hz	1.07%	SSI-UPCX	11Hz.avi
UR, local natural frequency	17.7 Hz	0.555%	SSI-UPCX	17.5Hz.avi
Head, ends x-dir, phase	25.939 Hz	1.756%	SSI-UPCX	26Hz.avi
Head mode Lower Arm	39.636 Hz	1.925%	SSI-UPC	39.6Hz.avi
Head Lower Arm	42.125 Hz	2.375%	SSI-PC	43.4Hz.avi
Head mode Lower Arm	46.743 Hz	4.07%	SSI-UPCX	46.8Hz.avi

Table 11.2: Modes found in the Head setup, the mode shape animations are calculated used basic FDD

Higher modes suspected to be present in the head, than the ones presented in table 11.2, have not been sufficiently identified.

Upper Arm (UA)

The estimations of the upper arm are done on the basis of two different measurements series, one measuring mainly vertical accelerations and one measuring mainly lateral accelerations. The upper arm is the part of the pantograph requiring most measurements to accurately describe the local dynamic behaviour, as it has a relatively complicated design.

Table 11.3 shows the node assignment in the vertical setup, Table 11.4 shows the node assignment in the horizontal setup and Figure 11.8 shows a local upper arm mode at 48Hz with the node numbering used in the upper arm.

Upper Arm, vertical	Node nr.	X	Y	Z
Ch 1	6	0	-1	0
Ch 2	6	0.469	0	0.883
Ch 3	4	0.469	0	0.883
Ch 4	9	0.469	0	0.883
Ch 5	3	0.469	0	0.883
Ch 6	5	0.469	0	0.883
Ch 7	10	0.469	0	0.883
Ch 8	7	0.469	0	0.883
Ch 10	11	0.469	0	0.883
Ch 11	9	0	1	0
Ch 12	2	0.469	0	0.883

Table 11.3: Node assignment of the vertical setup in the upper arm

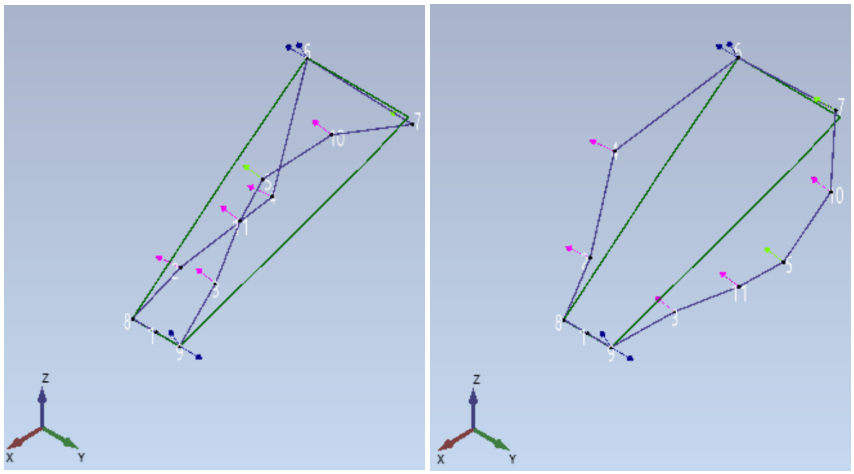

(a) **(b)**

Figure 11.8: Upper arm mode at 48Hz, with node numbering

Upper Arm, lateral	Node nr.	X	Y	Z
Ch 1	6	0.469	0	0.883
Ch 2	6	0	-1	0
Ch 3	4	0.126	-0.992	0
Ch 4	9	0	1	0
Ch 5	3	-0.126	-0.992	0
Ch 6	5	-0.126	-0.992	0
Ch 7	10	-0.126	-0.992	0
Ch 8	7	0	-1	0
Ch 10	11	-0.126	-0.992	0
Ch 11	9	0.469	0	0.883
Ch 12	2	0.126	-0.992	0

Table 11.4: Node assignment of the lateral setup in the upper arm

From the time series in Figure 11.10 the decay of the twisting mode at 11.5Hz is clearly visible after the mode is triggered at about 25 seconds. The same observation cannot be done in when sweeping downwards, suggesting that the decay may be influenced by closely spaced modes.

The short Fourier transform of channel 2 in the vertical test setup is presented in Figure 11.9. The most significant observation to be made is the bleeding at 11.5Hz after the sweep has passed, indicating that the mode still affects the dynamic motion.

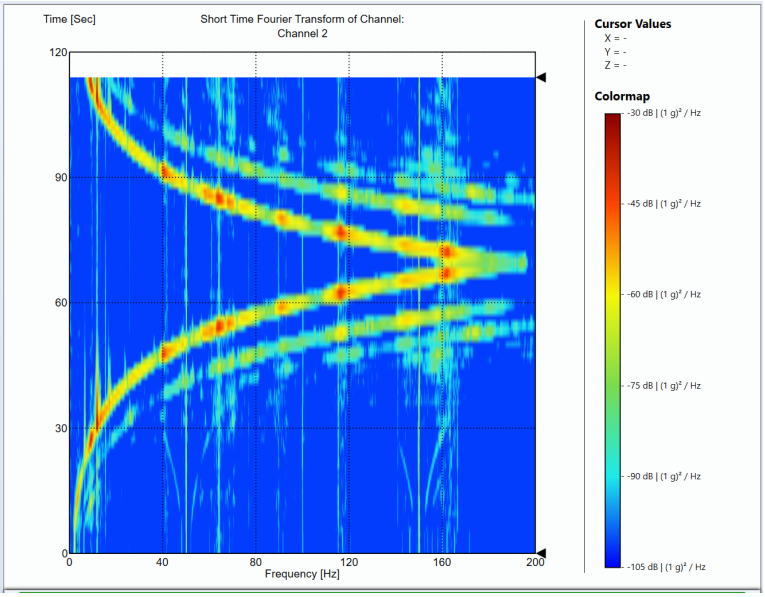

Figure 11.9: Short Fourier transform of channel 2 in the vertical upper arm setup

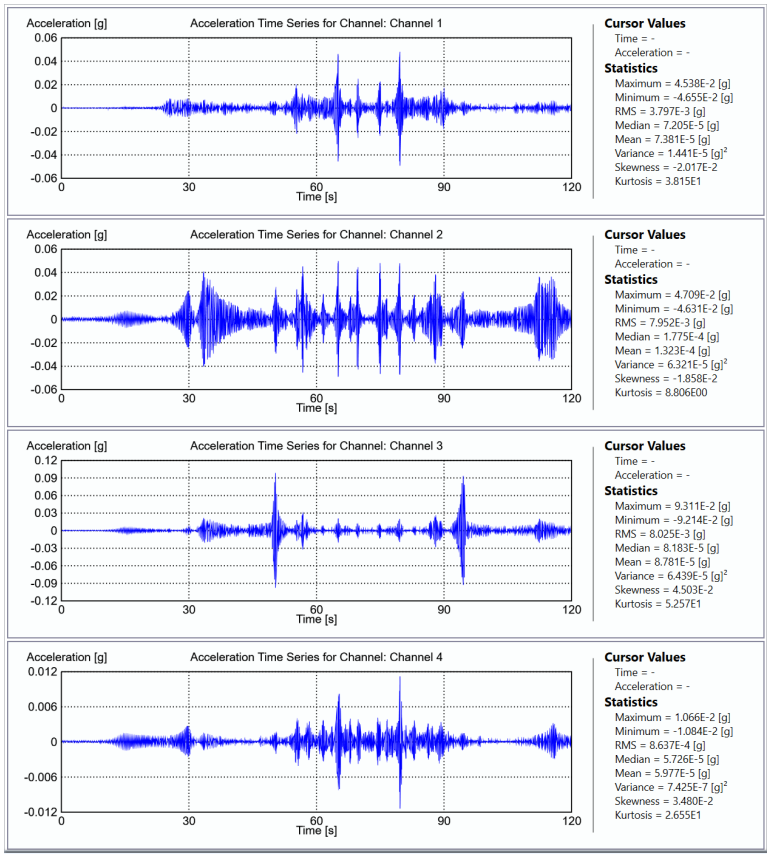

Figure 11.10: Acceleration time series from the vertical test setup

In Figure 11.11 the SVD-Plots displayed the spectral densities of the two test setups for the upper arm. The Plot in Figure 11.11a shows the spectral densities based on the combined setup, this is dominated by the motion from the vertical setup. Therefore the Spectral densities from the lateral setup are shown in Figure 11.11b in this plot the modes dominating in the lateral direction have more defined peaks at 6.4 Hz, 56 Hz and 132 Hz. Two more detailed plots for the vertical and lateral are displayed in Figure 11.11c and Figure 11.11d correspondingly.

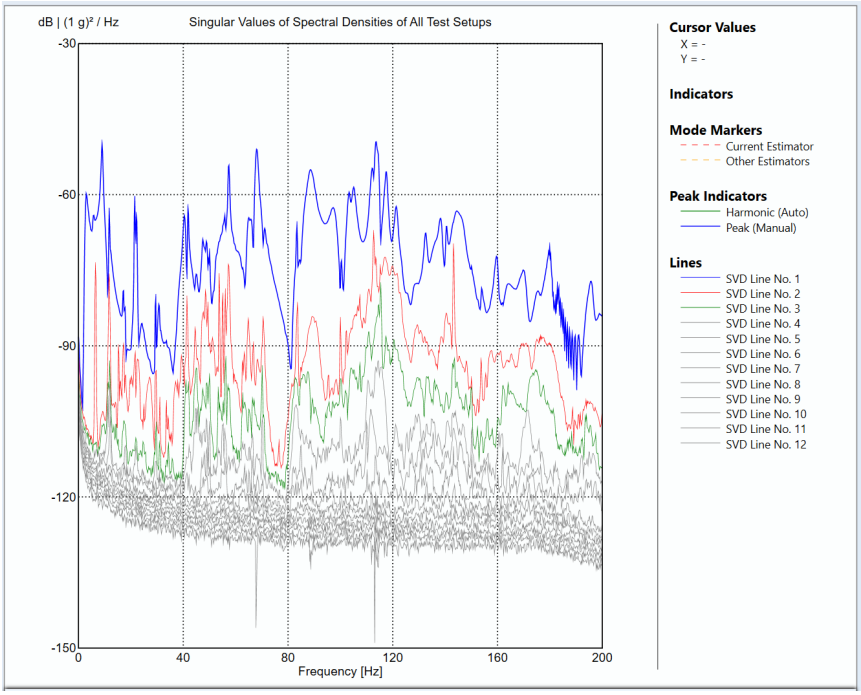

(a) Singular Value Lines for the combination of the Vertical and Lateral of the Upper Arm setup, Vertical setup dominating the plot

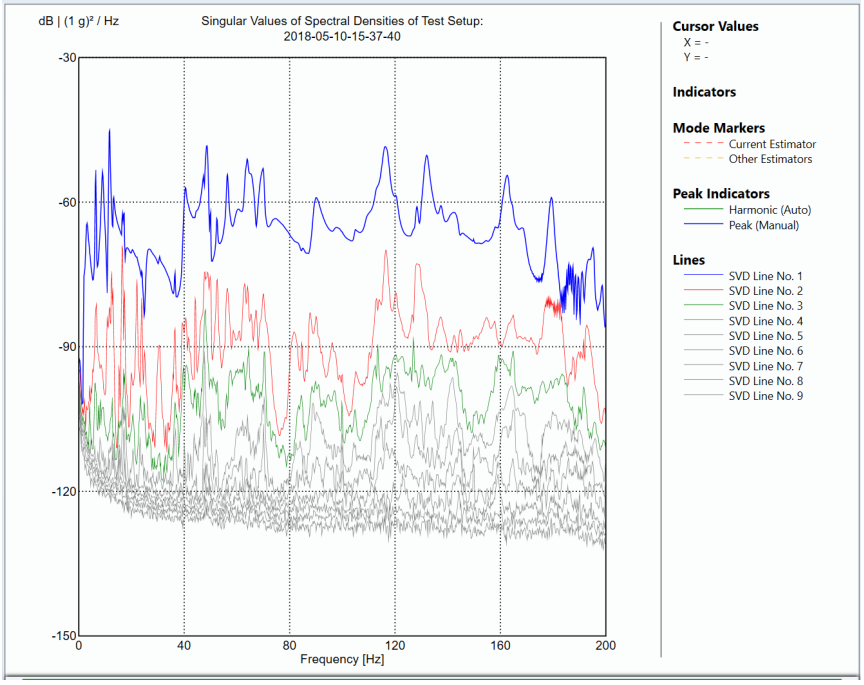

(b) Singular Value Lines for the Lateral setup of the Upper Arm

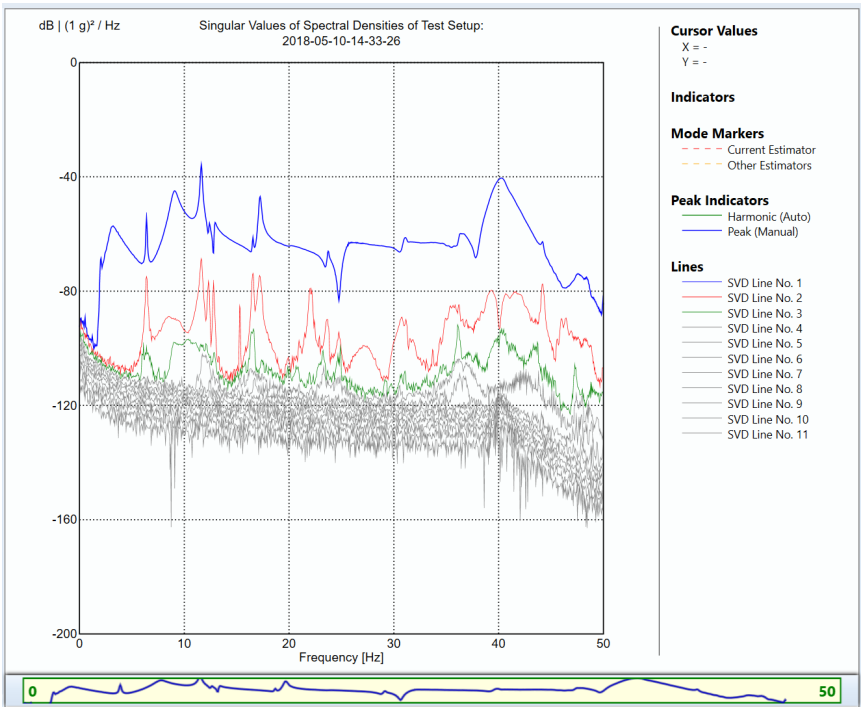

(c) Singular Value Lines for the Vertical setup of the Upper Arm from 0-50Hz

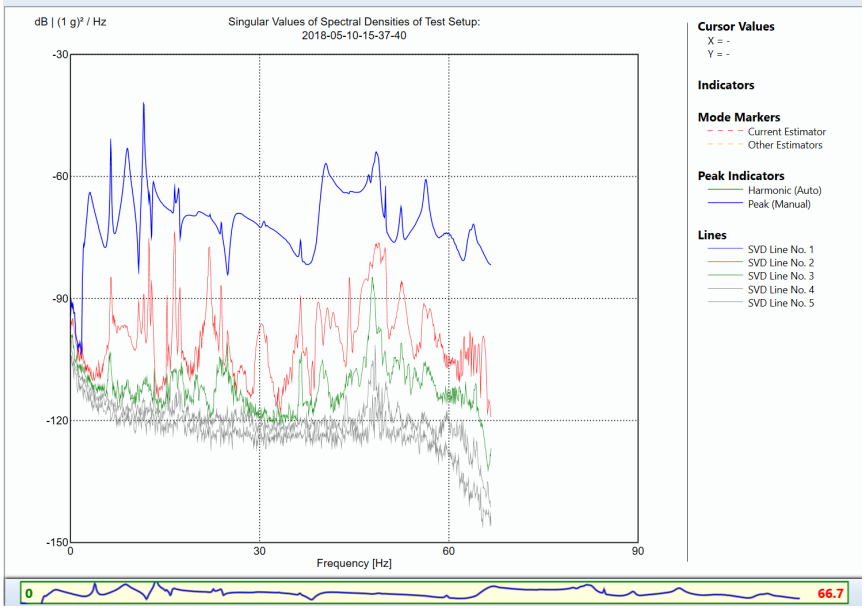

(d) Singular Value Lines for the Lateral setup of the Upper Arm from 0-66Hz

Figure 11.11: Plots of Singular Value Lines from testing of Upper Arm

Table 11.5 displays the modes found in the vertical test setup of the upper arm below 50Hz.

Table 11.5: Modes estimated in the vertical setup using SSI-UPCX up to 50Hz

Dominating part, Motion description	Freq. [Hz]	Std. Freq. [Hz]	Damp. [%]	Std. Damp. [%]	Compl. [%]
Bellow, RBM	3.79	0.89	46.541	16.644	1.504
UA, lateral motion	6.391	0.056	2.349	1.006	0.662
Knee, vertical	9.093	0.198	3.92	1.669	0.481
UA, twist	11.614	0.032	0.582	0.355	0.921
UR, 1st natural frequency	17.278	0.096	1.087	0.718	0.21
UA, bending vertical phase	40.14	0.342	0.814	0.254	0.43
No accurate description	41.351	1.048	2.527	2.141	6.245

Table 11.6 displays the modes found in the lateral test setup of the upper arm between 0-66Hz using SSI techniques. The quite broad acceptance conditions for modes required to estimate the bellow mode results in two modes that are assumed to not be significant in the estimation of the pantograph at 15.1Hz and 25.79Hz.

Table 11.6: Modes estimated in the lateral setup using SSI-UPCX up to 66Hz

Dominating part, Motion description	Freq. [Hz]	Std. Freq. [Hz]	Damp. [%]	Std. Damp. [%]	Compl. [%]
Bellow, RBM	3.723	0.444	46.126	23.416	1.346
UA, lateral motion	6.404	0.014	0.592	0.389	0.034
Knee, vertical	9.058	0.3	7.961	4.546	1.269
UA, twist	11.631	0.059	1.464	0.447	0.006
Suspected noise mode	15.138	1.124	9.851	6.646	31.75
UR,	16.543	0.302	2.978	1.15	15.744
Suspected noise mode	25.786	0.829	4.49	2.822	17.151
UA, bending vertical phase	40.472	0.167	0.884	0.235	6.306
No accurate description	42.756	0.816	2.606	1.219	9.082
No accurate description	46.488	1.146	4.029	2.344	31.218
UA, bending lateral c-phase	48.652	0.125	0.454	0.137	0.245
No accurate description	52.423	0.138	0.563	0.081	7.326
UA, lateral motion	56.386	0.083	0.439	0.158	0.261
UA, tuned mass bending	63.319	1.331	2.758	4.661	22.199

Additional modal beavhoir found in the upper arm at higher frequencies are observed at 113Hz in the vertical setup, and at 117 and 132Hz in both setups. However, efforts to precisely predict their properties have not been successful.

Lower Arm (LA)

Figure 11.12 shows the mode present in the lower arm at 68Hz, and table /ref relating the measurements channels to nodes and global directions. It is worth noticing that channel 3, the only one out of the four channels plotted, measuring in the lateral directions,

measures as expected significantly lower accelerations when sweeping through the lower frequencies. Further, the for the response at higher frequencies, where structural modes are dominating, the amplitude of the responses are more similar. In the short Fourier plot of channel 4 in Figure 11.14 the modes connected directly to the lower arm at 68Hz, 83Hz, 88Hz and the modes with rigid body motions at lower frequencies are clearly visible.

Table 11.7: Node assignment of setup for the lower arm

Lower Arm	Node nr.	X	Y	Z
Ch 1	1	-0.591	0	0.807
Ch 2	2	-0.591	0	0.807
Ch 3	3	-0.089	0.996	0
Ch 4	3	-0.591	0	0.807
Ch 5	4	0.089	0.996	0
Ch 6	4	-0.591	0	0.807
Ch 7	5	-0.089	0.996	0
Ch 8	5	-0.591	0	0.807
Ch 9	6	0.089	0.996	0
Ch 10	6	-0.591	0	0.807
Ch 11	7	0	0.996	0
Ch 12	7	-0.591	0	0.807

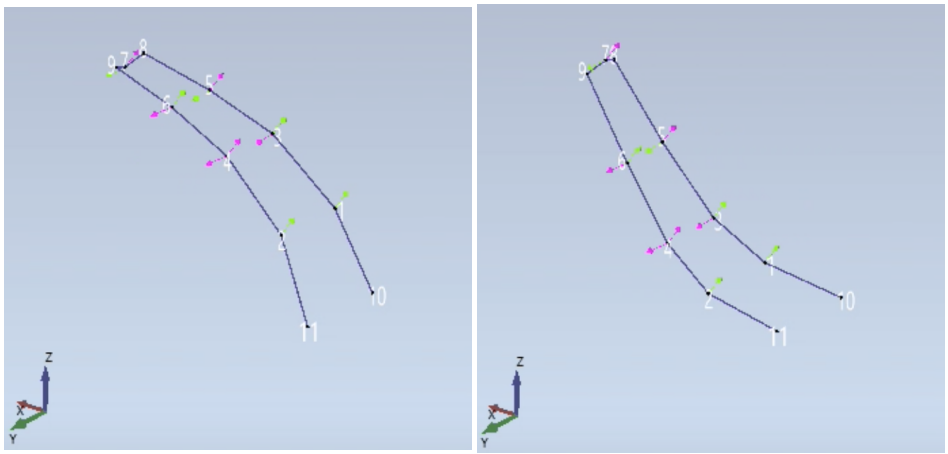

(a) **(b)**

Figure 11.12: The lower arm mode estimated at 68Hz, with node numbering for the lower arm

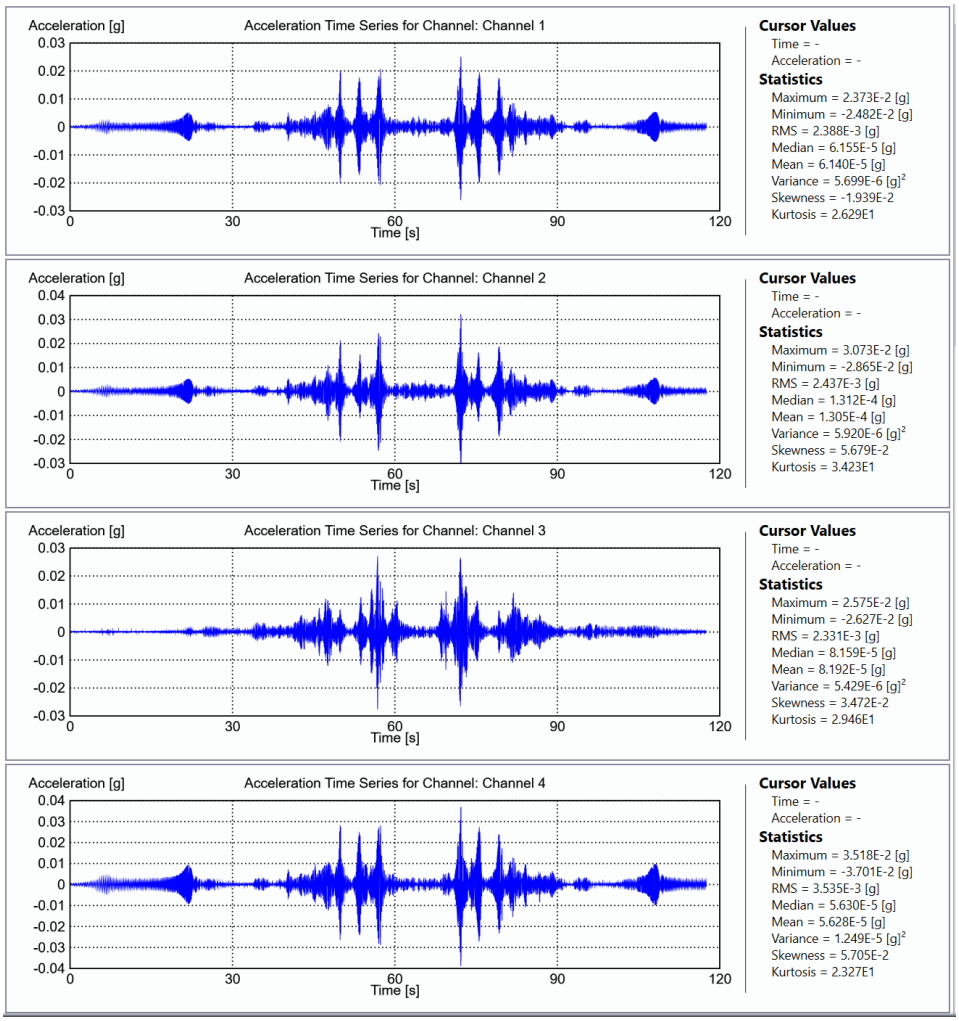

Figure 11.13: Acceleration time series of lower arm setup

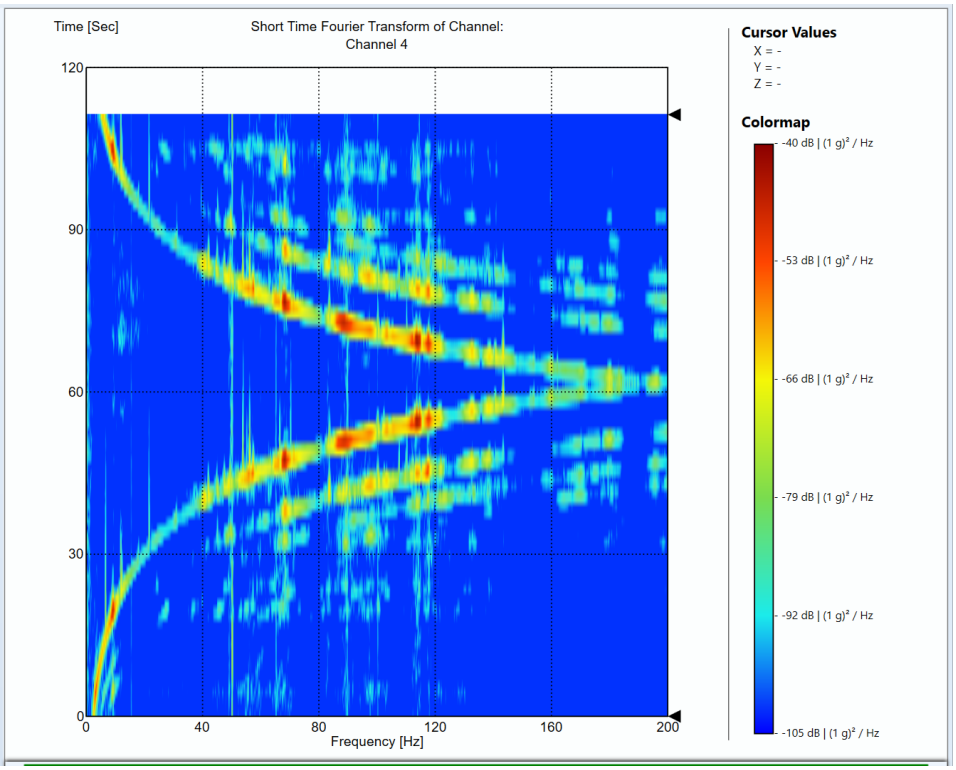

Figure 11.14: Short Fourier Transform for channel 4 in lower arm setup

From the singular value lines of the spectral densities of the lower arm in Figure 11.15 a few additional modes are clearly visible. The second singular value line shows quite clearly the presence of the lateral mode at about 6.4Hz. The mode with lateral knee movement at about 22Hz can be recognized in the first singular value line. Attempts to distinguish the dynamic behaviour between the two peaks close to this mode have not been successful. However, as mentioned in the chapter 9 the two wires stabilizing the upper arm is in resonance close to this frequency. The peak at about 30 Hz is suspected to be in connection with the first head mode, see the section about the upper rod.

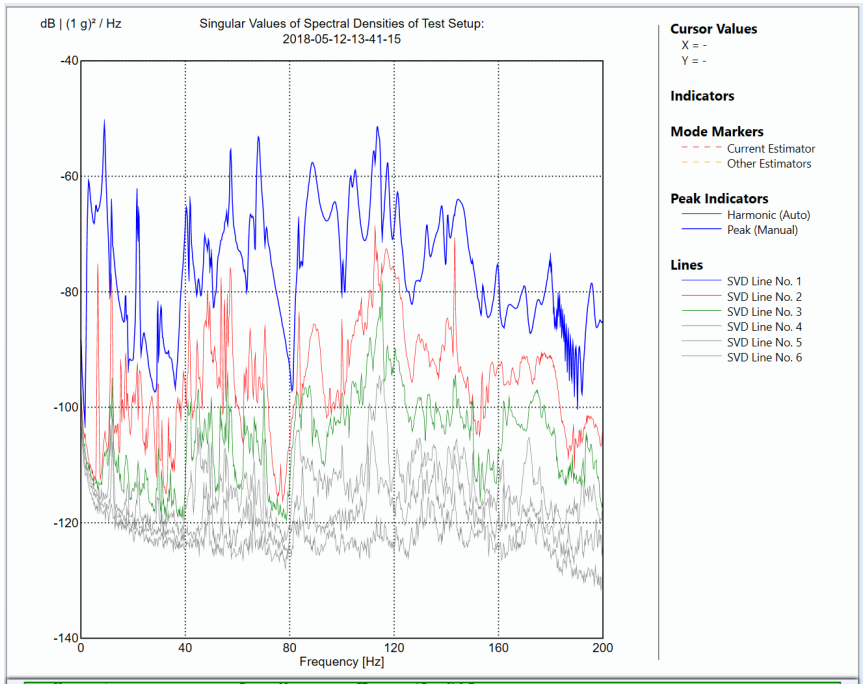

(a) Singular Value Lines for Lower Arm setup from 0-200Hz

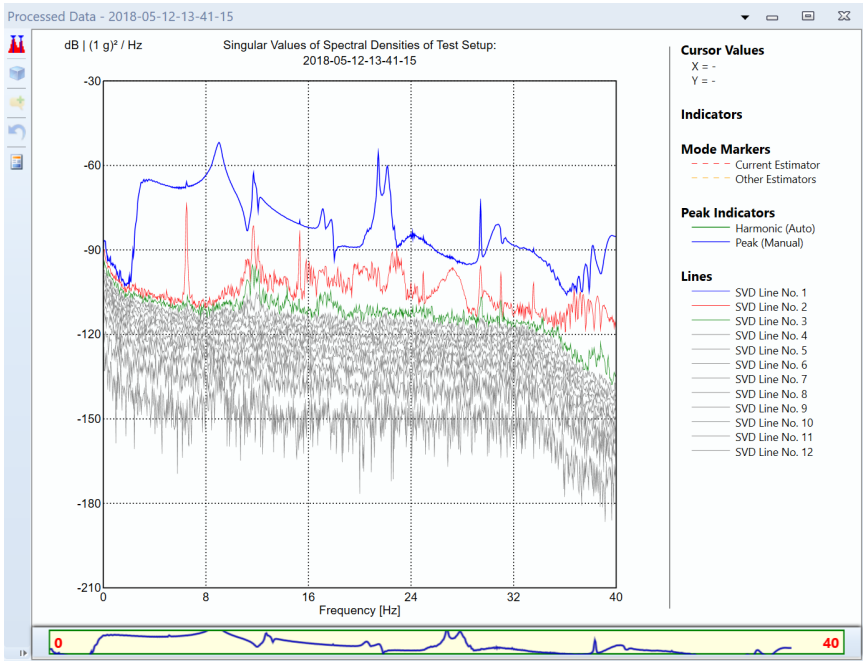

(b) Singular Value Lines for Lower Arm setup from 0-40Hz

Figure 11.15: Plots of Singular Value Lines of the spectral densities for the Lower Arm setup

Table 11.8 shows the modes estimated in the lower arm using SSI-UPCX for the modes below 30Hz and enhanced FDD for the remaining modes. It is worth noticing that the mean damping estimate for the mode at 6.4Hz is far larger than estimated in other parts. The plot of the second singular value of the spectral densities shows a narrow peak for this mode, suggesting that the damping is quite low.

Table 11.8: Modes found in the lower arm using SSI-UPCX and enhanced FDD, the mode shape animations are based on basic FDD

Dominating part, motion description	Freq. [Hz]	Std. Freq. [Hz]	Damp. [%]	Std. Damp. [%]	Compl. [%]	File-name
Bellow, RBM	3.97	0.761	41.408	10.112	0.212	2.9.avi
UA, lateral	6.406	0.532	11.625	14.434	25.328	6.4.avi
Knee, Vertical	9.119	0.163	3.248	0.928	0.023	8.9.avi
UA, twist	11.937	0.129	1.164	0.565	1.467	11.7.avi
Knee, lateral	21.521	0.14	0.368	0.159	0.15	22.avi
UA, bending vertical	40.394	N/A	0.518	N/A	3.296	40.4.avi
Unidentified	41.852	N/A	0.206	N/A	1.562	41.8.avi
UA, bending lateral phase	57.363	N/A	0.408	N/A	2.605	57.4.avi
LA, bending vertical	68.03	N/A	0.547	N/A	0.664	67.9.avi
LA, bending out of phase	83.372	N/A	0.257	N/A	38.851	83.4.avi
LA, bending out of phase	88.839	N/A	1.164	N/A	58.581	88.8.avi
Unidentified	97.07	N/A	N/A	N/A	13.387	96.7.avi
LA, bending lateral c-phase	104.948	N/A	0.639	N/A	34.741	104.8.avi

Upper Rod (UR)

The short Fourier transforms through the measurement series of the upper rod is plotted in Figure 11.17. From this the first natural frequency of the upper rod is quite easy to detect at 17 Hz. The third natural frequency is somewhat more difficult to identify, but there is clearly more dynamic motion from 159-175Hz. A consideration of beam theory and the first natural frequency indicates that the third natural frequency should be just below this frequency interval, at $17.2 \cdot 3^2 = 154.8$. Nevertheless, in the plot of the upper rod's singular values of the spectral densities in Figure 11.18 there is a peak, which appears to go through a shift, in the first SVD-line closer to the expected frequency at 154.8Hz. Further, the spectral densities indicate that the dynamic behaviour of the global system is largely present in the upper rod. Particularly modes where the head or lower arm are set in motion, as they are directly connected with the rod. The orientation of sensor in the lower rod setup is given in table 11.9 and the mode shape at 30.4Hz is shown in Figure 11.16. This mode is assumed to be connected with the first head mode.

Table 11.9: Node assignment of the setup of the upper rod

Upper Rod	Node nr.	X	Y	Z
Ch 1	1	-0.15	-0.989	0
Ch 2	1	0.466	0	0.885
Ch 3	2	-0.15	-0.989	0
Ch 4	2	0.466	0	0.885
Ch 5	3	-0.15	-0.989	0
Ch 6	3	0.466	0	0.885
Ch 7	4	-0.15	-0.989	0
Ch 8	4	0.466	0	0.885
Ch 9	5	0.15	0.989	0
Ch 10	5	0.466	0	0.885
Ch 11	1	-0.875	0.133	0.412
Ch 12	5	0.875	-0.133	-0.412

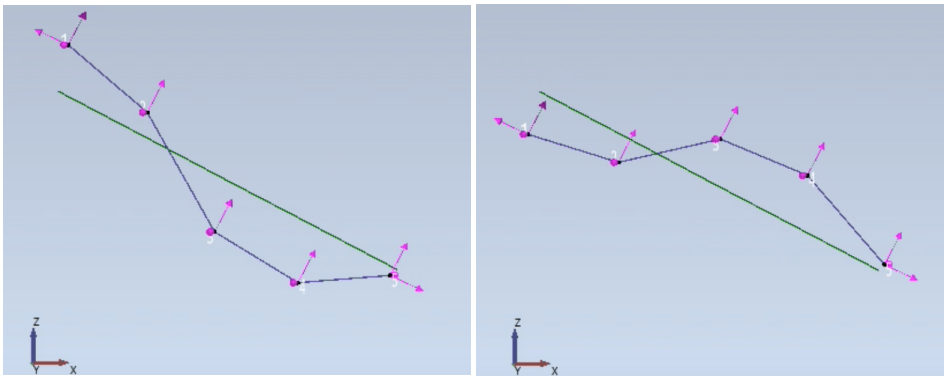

(a) **(b)**

Figure 11.16: Upper rod behavior at 30.5Hz suspected to be caused by the first head mode. Node numbering for the upper rod 1 to 5 from the left.

From the plot of the upper rod's singular values of the spectral densities in Figure 11.18 it is clear that global modes largely affects the dynamic behaviour of the rod itself. Table 11.10 shows the modes estimated in the upper rod setup using the enhanced FDD estimator. It is worth noticing that the damping of the mode at 3.148Hz and 8.914Hz is thought to be too small. However, this estimator was chosen due to the fact that in the upper rod it is most important to identify the structural modes, rather than the bellow modes. Even though it is not recommended to use the complexity present in modes when using FDD, for this setup it is thought that complexity might represent some external motion resulting in compression of the rod.

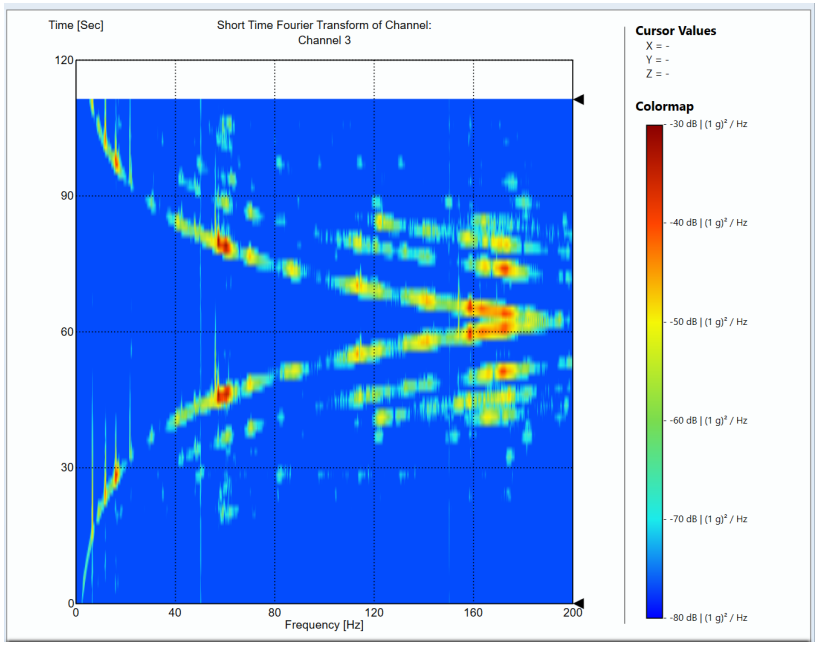

Figure 11.17: Short Fourier Transform form channel 3 in the upper rod setup

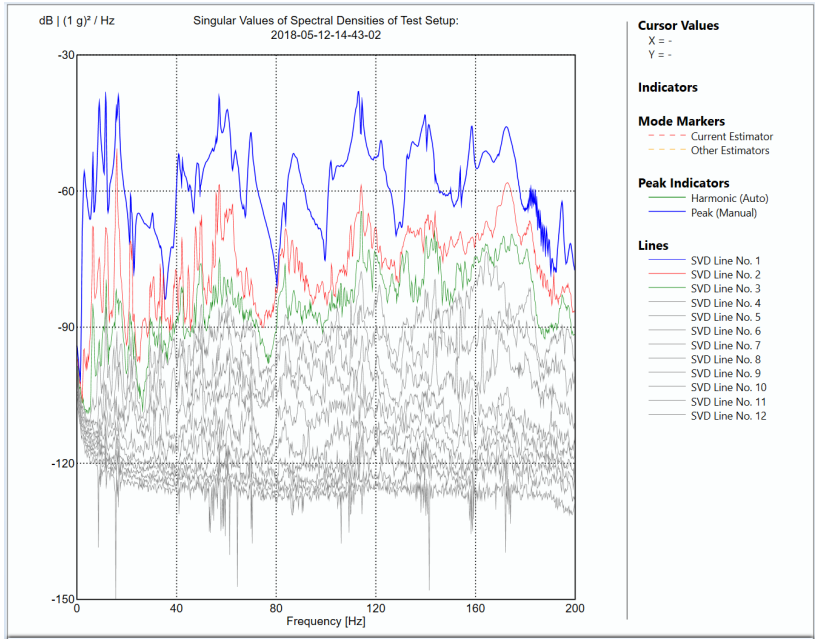

Figure 11.18: Singular Values of Spectral Densities of Upper Rod setup

Table 11.10: Modes found in the upper rod setup with the enhanced FDD method, mode shape animations based on basic FDD

Dominating part, motion description	Frequency [Hz]	Damping [%]	Complexity [%]	File name
RBM, bellow	3.148	15.345	0.115	2.9.avi
UA, lateral	6.408	1.968	2.044	6.4.avi
Knee, vertical	8.914	2.907	0.088	8.9.avi
UA, twist	11.591	1.175	0.049	11.5.avi
UR, first mode	16.623	1.425	4.156	16.6.avi
Knee, lateral	21.577	0.546	0.469	21.4.avi
Head, first head mode*	30.29	0.554	90.151	30.4.avi
UA, vertical bending, phase	40.909	1.372	2.556	40.8.avi
UA, lateral bending, c-phase	48.368	0.781	2.789	48.2.avi
UA, lateral bending, phase	57.032	0.171	20.142	57.avi
UA, vertical bending, c-phase	63.65	0.827	4.99	63.6.avi
UR, second natural frequency	69.752	0.863	0.944	69.9.avi
LA, bending c-phase	83.008	0.426	81.144	83.avi
LA, bending out of phase	87.114	1.042	42.768	86.9.avi
Unidentified	112.956	0.891	0.706	113.avi
Unidentified	139.638	0.976	33.334	139.4.avi
UR, shape as 1.5 sine	158.813	0.879	1.441	158.6.avi
Unidentified	172.282	0.464	2.243	172.6.avi

The modal behaviour found at 30.29Hz, in the upper rod setup, seems to correspond with what is expected from the first head mode found at 25.97Hz, found in the head setup. This result will be further discussed in the Abaqus analysis.

Lower Rod (LR)

The short Fourier transform plot of the lower rod in Figure 11.21 indicates the existence of at least three modes just above 40Hz, a mode at 56.9hz and a few modes from 140Hz and above. Further, peaks at these frequencies are found in the plot of the singular values of the spectral densities of the lower rod in Figure 11.22. It is also worth mentioning the peaks at 22Hz, the two peaks below 120Hz and the two peaks at around 158-164hz. The peaks at 22Hz are assumed to be connected with lateral motion in the knee. The peaks at 158-164Hz have not been sufficiently identified. The sensor orientation is presented in table 11.19 and the first mode of the lower rod in Figure 11.20.

Lower Rod	Node nr.	X	Y	Z
Ch 1	1	0.666	0	0.746
Ch 2	1	0	1	0
Ch 3	1	-0.746	0	0.666
Ch 4	2	-0.666	0	-0.746
Ch 5	2	0	-1	0
Ch 6	2	-0.746	0	0.666
Ch 7	3	-0.666	0	-0.746
Ch 8	3	0	-1	0
Ch 9	3	-0.746	0	0.666
Ch 10	4	-0.666	0	-0.746
Ch 11	4	0	-1	0
Ch 12	4	-0.746	0	0.666

Figure 11.19: Node assignment of the setup of the upper rod

The spectral density plot of the lower rod has multiple peaks around 40Hz this includes the movement of the modes in the upper arm and the first frequency of the lower rod itself. The entire spectrum is highly affected by the global behaviour.

The SSI-UPCX estimated natural frequencies are presented in Table 11.11. Due to the joint design used to connect the lower rod, one might suspect two base natural frequencies. The latter of which was not found.

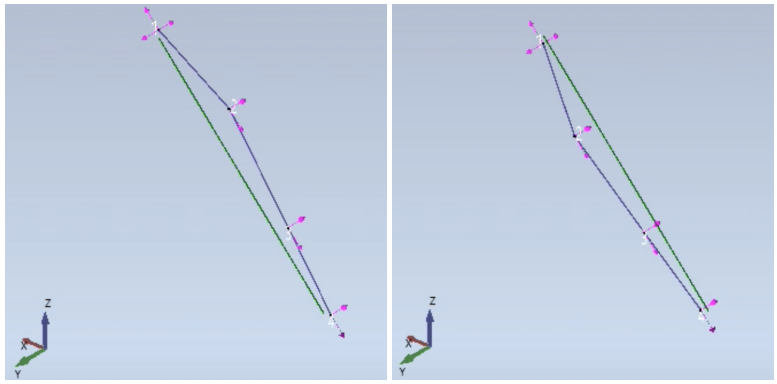

(a) **(b)**

Figure 11.20: Lower rods first mode at 43.2Hz

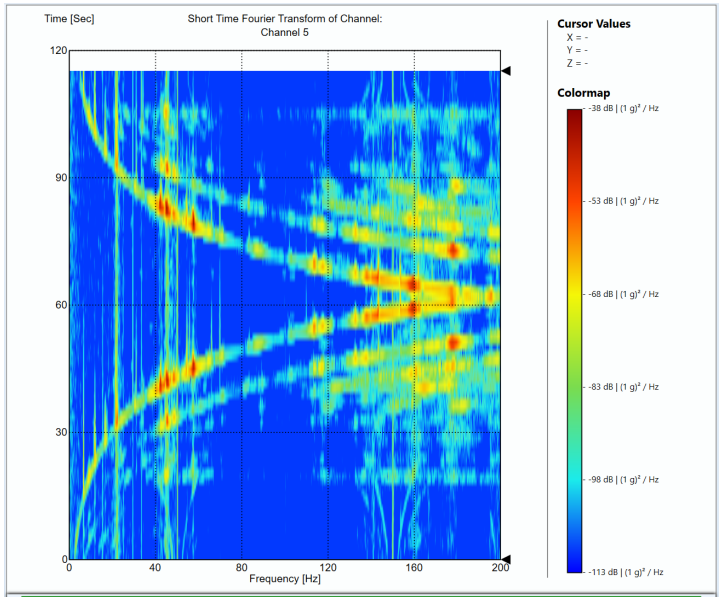

Figure 11.21: Short Fourier Transform of channel 5 in the lower rod setup

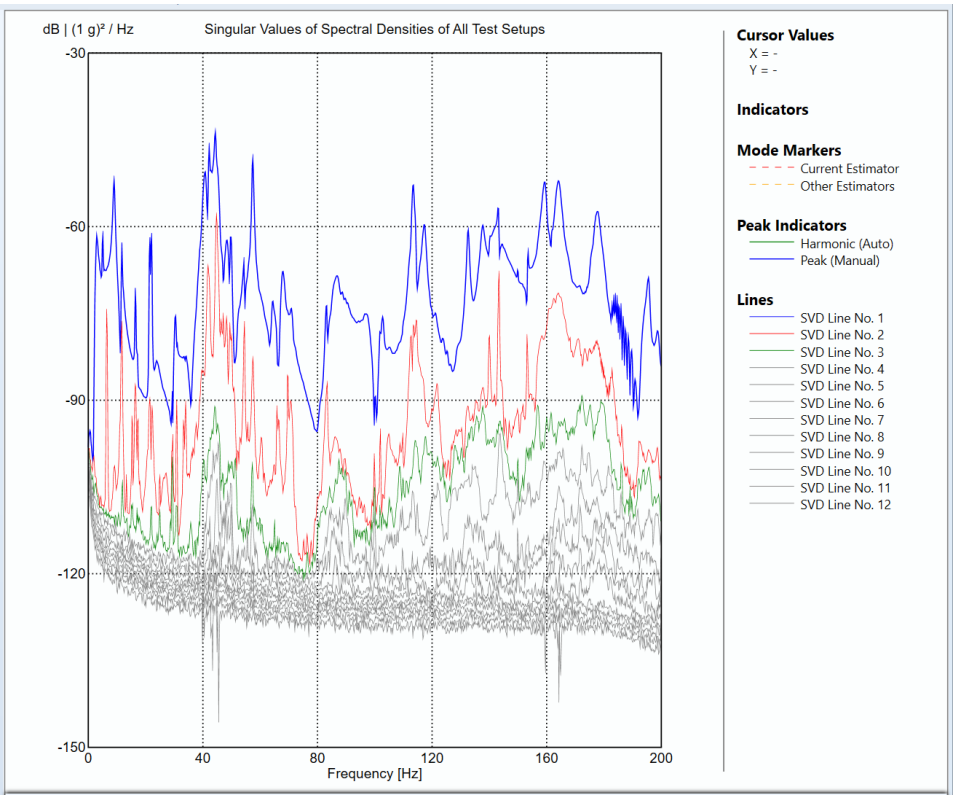

Figure 11.22: Singular Values of Spectral Densities of Lower Rod setup

Table 11.11: Natural frequencies of the lower rod

Dominating part, Motion description	Frequency [Hz]	Std. Freq. [Hz]	Damping [%]	Std. Damp. [%]	Complexity [%]
LR, 1st natural freq.	43.75	0.342	0.859	0.412	2.565
LR, 2nd natural freq	179.124	1.151	2.551	2.113	3.378

11.2.3 Mode by mode Evaluation

In this section the modes present in the pantograph and what may effects their estimates are presented. The modes presented in this section have been evaluated by multiple test setups and estimators. Thus some seemingly contradicting data will be presented. The deviation in estimates done based on different test setups and estimators will be presented, along with an evaluation of what may have caused these deviations.

Rigid Body Mode (RBM)

This mode is dominated by rigid body motion of the lower and upper arm. The stiffness provided to this motion is due to the bellow. Figure 11.23 shows the coarse mesh mode shape estimation. The estimations from the upper and lower arm setup suggest damping between 40 and 50%. However, this is presented with large standard deviations.

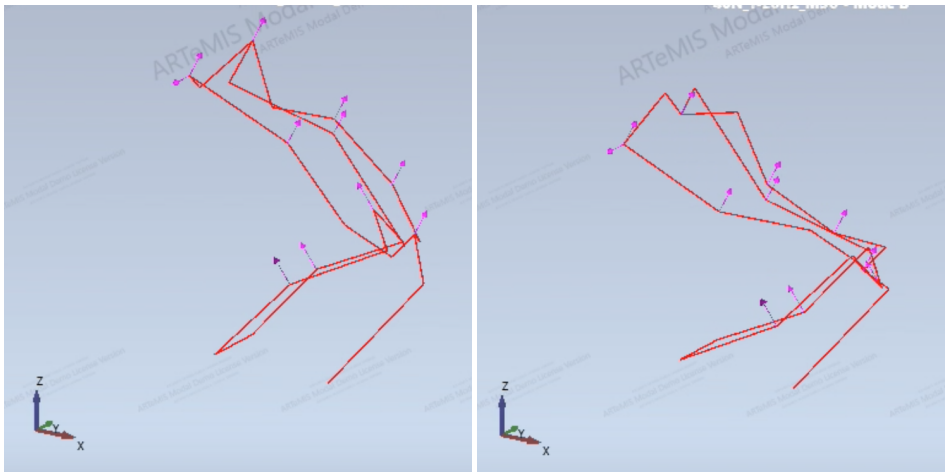

(a) **(b)**

Figure 11.23: Bellow, RBM

Lateral mode with large movement in Upper Arm

The lateral motion in this mode is largely concentrated in the Upper Arm. This result in large lateral motion of the head. The mode is also sensitive towards alteration of the testing setup. This is due to low initial lateral stiffness, that a small change in setup resulting in stiffness in the lateral direction and that the test setup excites the pantograph vertically. The large variation in the estimated damping for this mode is likely due to miss assignment of decay from the nearby vertical modes. Estimations from the enhanced FDD technique have been as low as 0.5%.

Knee, vertical motion

In this mode, the motion in the Upper and Lower Arms are out of phase. The lower arm moves rigidly while the motion in the upper arm has some bending contribution as well as rigid motion. Damping estimated from the lower arm setup and the upper arm setup should be used. However, the standard deviations presented are quite large.

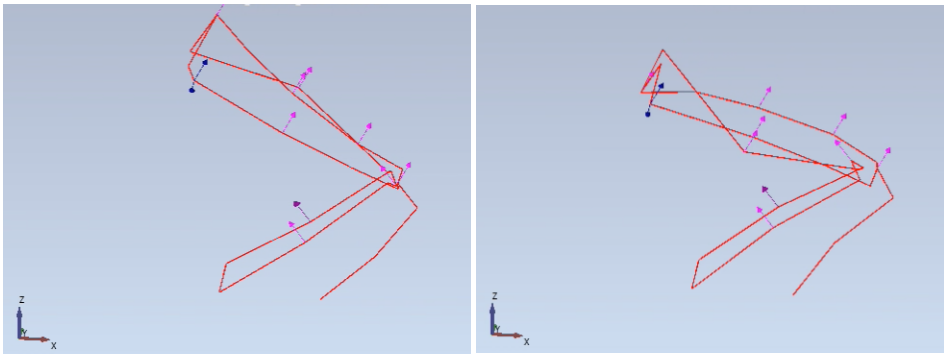

(a) (b)

Figure 11.24: Coarse mesh estimation of the vertical knee mode

Twisting in Upper Arm

In this mode, the upper arm is twisted resulting in a rigid rotation in the YZ-plane of the Head around mid-span. Although, the damping estimations for this mode differs between the two upper arm setups and the lower arm setup it is believed to be in the range 0.5 to 1.5 %.

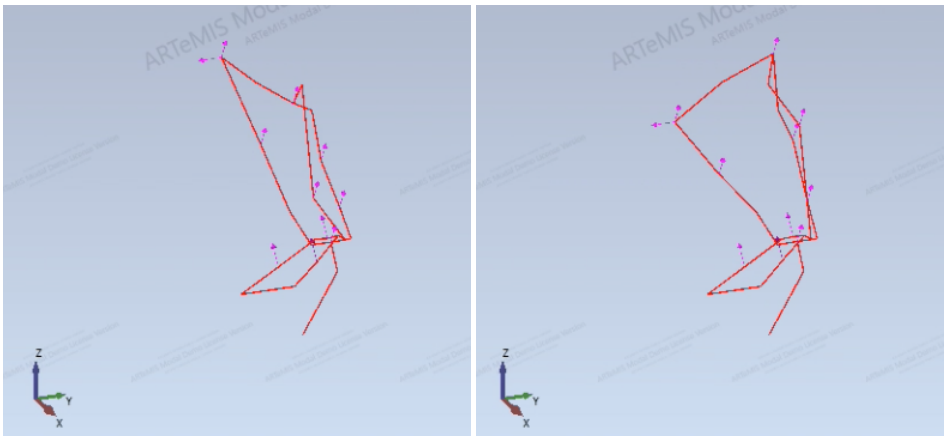

(a) (b)

Figure 11.25: Twisting of the upper arm

Upper Rods First Mode

This mode is dominated by the Upper Rods first mode, the result of this is some unsymmetrical movement in the connected Head and further in the upper arm, while the lower arm connected to the lower joint of the upper rod is seemingly unaffected.

Lateral Knee Movement

In this mode the pantograph knee moves laterally as indicated by the mode shapes in the upper and lower arm shown in Figure 11.26

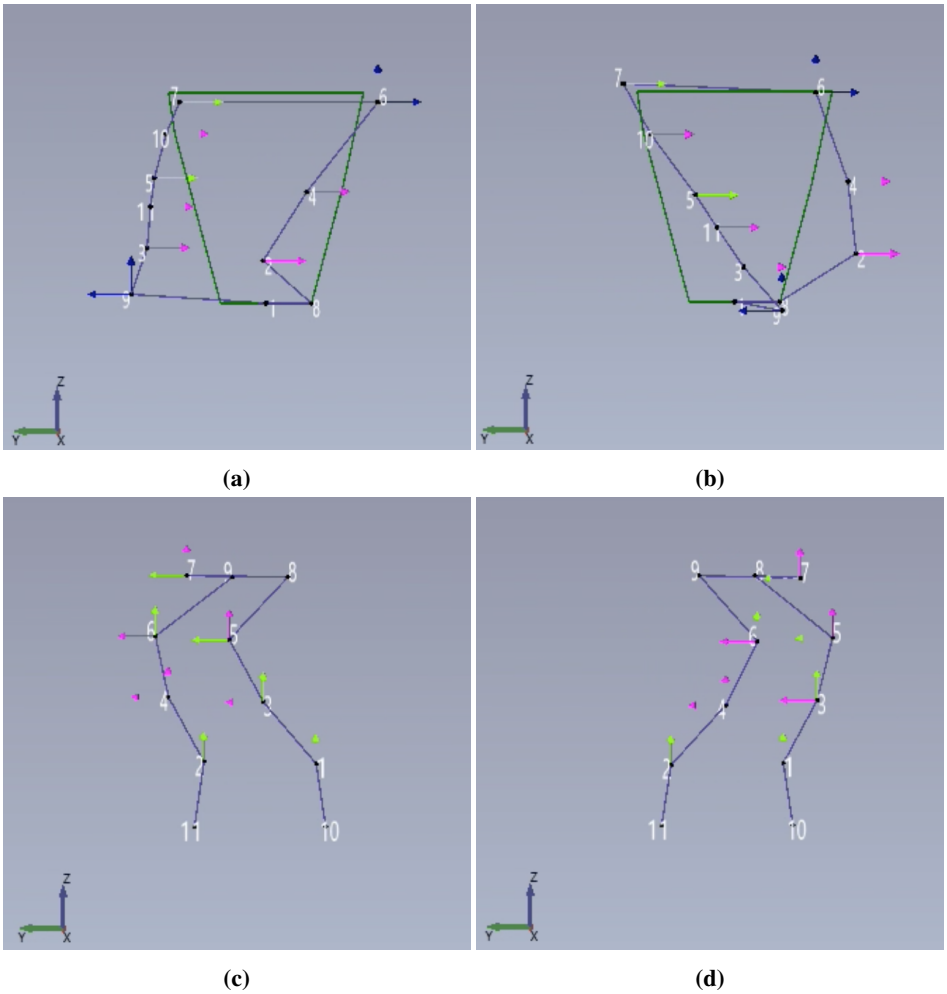

(a) **(b)**

(c) **(d)**

Figure 11.26: Knee lateral motion at 22Hz, is indicated by the motion in the lower and upper arm

Upper Arms First Mode

This is the first bending mode of the upper arm both in and out of phase for the two main beams in the arm. Is suspected to be closely spaced in around the same frequency at 40Hz. However, only the in-phase bending have been properly separated and identified, shown in Figure 11.27.

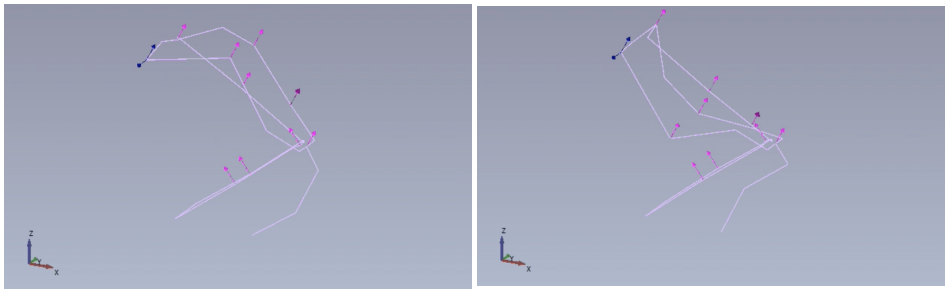

(a) (b)

Figure 11.27: The upper arm in phase vertical bending estimated at 40.8Hz

Lower Rods First Modes

The first mode of the lower rod is found at 43.75Hz. This estimation is difficult to validate as it is suspected that there are closely spaced modes in both the upper and lower arm.

Lower Arm First Mode

This mode is found at 68Hz, the mode is displayed in part by part section of the modal analysis results.

11.3 Discussion

The discussion will initially present the main remarks about the modal analysis, then an evaluation of the estimators used, followed by an evaluation of the measurement setup, before discussing the main findings of the modal analysis.

In conducting and from considering the results from the modal analysis there are six remarks worth mentioning. First, the damping for modes with rigid body motion of the lower arm is larger than usual for civil engineering structures. This might not come as a surprise, but need to be considered in regard to the estimators used and the bandwidth of the modes. Second, there are closely spaced modes present in the tested pantograph at 40Hz. Third, the circular cross-sections present in all the moving parts do not only render closely spaced modes with small differences due to boundary conditions. It also makes it harder to precisely predict, and later measure, which plane these modes will move in. Fourth, the pantograph has a considerable number of structural frequencies connected to the individual parts. Unfortunately, some of these modes occur at similar frequencies. Fifth, the mode with twisting of the upper arm seems particularly unfavourable for a smooth catenary pantograph interaction. Sixth almost all structural modes are found in the head setup, implying that the local modes will affect the catenary pantograph interaction.

The different estimators within the same setup and estimates form different setups results in corresponding frequencies and mode shapes, for modes up to 30Hz. However, the estimation of damping in the first four modes differs largely between estimators. This is probably due to the fact that the FDD techniques are established on the assumption of small damping. Therefore, when evaluating the damping estimates for the first four modes the results of the SSI-methods should be considered more reliable. Given that the estimator is able to identify all the modes in the frequency band characterized by large damping. This makes sure that the energy content is better assigned to the correct modes. In an evaluation of the lightly damped modes the choice of an adequate estimator still relies on the ability to detect the nearby modes. This is easier to achieve with the FDD methods at the higher frequencies since they mainly estimated modes based on local effects in the spectral density. Unlike the SSI-methods which, when unfiltered, and during a single calculation will have challenges in estimating all modes across a large frequency band. At least in cases where measured modal behaviour is similar. As is the case in the considered pantograph.

Damping estimates in operational modal analysis techniques, which have been used to evaluate the measurement series trigger by a sweep, usually require quite long recorded data series to allow the decay of each mode to be measurable. The utilized SSI-method, UPCX, is data-driven which does not provide precise estimations of the estimated uncertainties of highly damped modes. Therefore, statistical analysis using multiple test series should have been used. Since the data driven approach requires long measurement series, and the modes are only exited as the sweep travels past its frequency. Further, estimations specifically targeting these modes are needed. If this should be done using modal analysis is unclear. Since the pantograph has two system dampers, a more direct approach should be considered. Additional, the use of a data-driven estimator to evaluate a recording of a sweep is not optimal. Because to enable the data to drive the estimations the input should be stochastic to some degree.

In further evaluation of this and other pantographs, it would be useful to have test setups with more than 12 measurement channels, especially since each sensor adds mass to the structure. The value of each sensor used during measurements should be maximized. That is, each utilized sensor should perform measurements in all three directions. Then the choice of where to place sensors should also include a consideration of where three measurement directions are most beneficial.

The first six modes found are the most important to identify in the considered pantograph. Since they are believed to dominate the dynamic response and are likely to be present in other pantograph designs. Unlike the structural modes present at higher frequencies, whose behaviour are connected to the specific cross-sections used in the design. Although, structural modes might affect the pantograph catenary interaction. They will need to be evaluated with the specific pantograph design in mind. There has been difficulty in fully separating the modes believed to occur at about 40Hz, on the basis of multiple peaks in the first and second singular value lines of the spectral densities for the lower rod and upper arm.
From the plots of the singular values of the spectral densities presented in the results of the modal analysis. It seems clear that the spectral densities of the system can be described by the first three singular value lines, reducing the vector space from twelve, or in some cases 11, to 3 dimensions. This interpretation render the remaining singular values as noise.

11.4 Conclusion

The modal analysis performed was initiated by a coarse mesh analysis, that provided information about the global behaviour of the pantograph. Then a more detailed modal analysis of the dynamic behaviour of each part was performed. The main estimates used was SSI-UPCX and enhanced FDD, some supporting calculations where done using SSI-PC. The enhanced fdd estimations targeted frequencies up to 195Hz, based on measured acceleration with a sampling frequency of 400Hz. However, the main focus was to identify the dynamic behaviour for frequencies up to 70Hz. This was not achieved as it is assumed that modes not sufficiently characterized occur at about 40 Hz.

The main finding of the modal analysis where the six first modes. The RBM mode due to the bellow stiffness, with a large damping, at about 3.5Hz. The close to rigid lateral motion of the upper arm, at 6.4Hz. The vertical motion of the knee, initiating bending in the upper arm, at 9Hz. The torsional behavior of the upper arm, resulting in large rigid rotations of the head, at 11.6Hz. The first resonance mode in the upper rod, initiating head vibrations, at 17.2Hz. Finally, the lateral knee motion at 22Hz is close to the resonance of the stabilizing wires of the upper arm, which have been discussed in Chapter 9. Preliminary results contain resonance in the individual parts resulting in global vibrations and that damping of modes not connected to bellow movement in large part is small.

Future analysis of pantographs should focus on identifying the damping of the bellow connected modes using the specifications of the dampers in the system. Estimation of damping in structural modes seems to be possible using the applied modal analysis estimators. That will benefit from implementing stricter acceptance criteria when the highly damped modes can be ignored.

12 — Abaqus Model

For analysis Abaqus CAE have been chosen because of the possibility of running linear perturbation frequency calculations of the structure as well as explicit dynamic simulations on the pantograph. The version used is 6.14-4.

In this chapter the model procedure, properties and analysis setups of the model will be presented. Followed by the results obtained from the numerical model and a comparison to the behavior observed and analyzed in the lab experiments.

12.1 The Model

(a) Abaqus model, wire model

(b) Abaqus model, rendered with cross sections

The Abaqus model is made up by multiple bodies created as 3D wire models assembled with connectors and constraints. The dimensions of the pantograph are obtained in the lab with a measuring tape due to lacking documentation. The measurements was performed from centre-centre of the members and where they intersect. This measurements was preferred because the wire features resembles the centre of the cross sections.

The cross sections of the pantograph is unknown and closed, e.i. there is no suitable way to measure the thickness. It is therefore initially guessed and later used as a parameter to tweak the model to match the dynamic behaviour of the physical model in the lab.

12.1.1 Frame

All the beams used in the frame are made out of steel. A box 80mm x 50mm cross section is used for the outer rectangle and the member spanning between in the y-direction. The rear fixture beams and the front one are made out of U-profile similar to the box, but with an open end. The U-profile with a width of 61mm is used for the fixture beams. The horizontal beams used to connect the lower arm are of the 56mm U-profile. The front bracket on the frame, where the lower rod is connected, is modelled with a rectangular 25mm x 25mm profile instead of the flat plates used on the one in the lab. This is done on the Abaqus model to increase the stable time increment in the explicit time analysis.

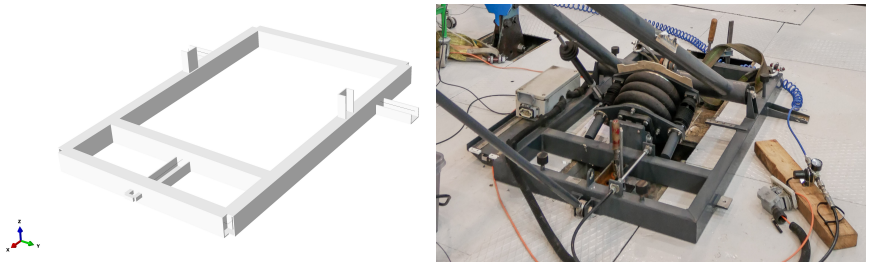

(a) Frame Abaqus

(b) Frame Lab

Part: Frame	Dimensions			
Cross section name	x [mm]	y [mm]	OD [mm]	Thickness t [mm]
Box 50x80	50	80		4
U-profile 61x40	61	40		4
U-profile 56x32	56	32		4
Rectangular 25x25	25	25		

Table 12.1: Frame Cross Sections

12.1.2 Lower Arm

All the members of the lower arm are made out of steel. The tube used to connect the arm to the frame and bellow have an outer diameter (OD) of 90mm. The beam used to connect the bellow to the 90mm tube is simplified as a rectangular cross section of 80mm x 30mm, named bellow connection beam. The top tube, on the left hand side in 12.3a, have an OD of 70mm. The tubes stretching in the longitudinal direction have an OD of 65mm. The feature of plates in Figure 12.3b, used to connect the upper rod to the 65mm tube is substituted with a rectangular box profile with dimensions 25mm x 25mm like on the frame to increase the critical time step.

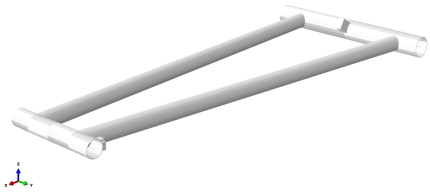

(a) Lower Arm Abaqus

(b) Lower Arm Lab

Part: Lower Arm	Dimensions			
Cross section name	x [mm]	y [mm]	OD [mm]	Thickness t [mm]
Tube 65 mm			65	2
Tube 70 mm			70	2.3
Tube 90 mm			90	2
Bellow conn. beam	80	30		
Rectangular 25x25	25	25		

Table 12.2: Lower Arm Cross Sections

12.1.3 Upper Arm

The upper arm is a mix of two materials. All the members except the horizontal tube on the right hand side in 12.4a are made out of steel, the one on the right is out of aluminum with an outer diameter of 30mm. The beam on the left hand side in 12.4a used to connect the lower rod is simplified to one beam instead of two separate plate features seen in Figure 12.4b. The cross section of 50mm x 25mm is chosen to resemble the physical one with respect to stiffness, called lower rod connection arm. The effect of increasing the total material of the arm will be discussed in the assembly section. The lateral tube this is connected to have an OD of 50mm. The beams running in the longitudinal direction connecting the 50mm tube and 30mm aluminum tube have multiple cross sections. The beam is stepping down two times and goes from 50mm to 40mm, to 30mm from left to right in Figure 12.4a. The first section from the lateral 50mm is 50mm, then stepping down to 40mm, and finally 30mm. In the area where the 30mm section is used the beam changes angle at approximately the position where the wires are connected in Figure 12.4b.

The wires used on the pantograph is not modelled for simplification. The ones on the pantograph are not correctly pretensioned and their contribution to the horizontal stiffness is therefore assumed neglectable.

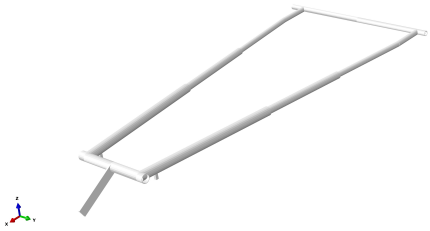

(a) Upper Arm Abaqus

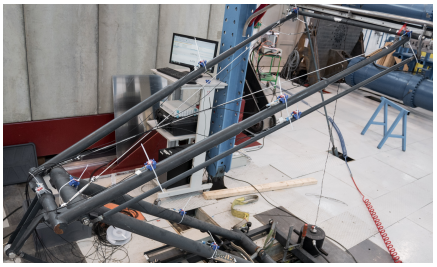

(b) Upper Arm Lab

Part: Upper Arm	Dimensions			
Cross section name	x [mm]	y [mm]	OD [mm]	Thickness t [mm]
Tube 30mm steel			30	2.2
Tube 30mm alu.			30	1.8
Tube 40mm			40	2.2
Tube 50mm			50	2.2
Lower rod connection arm	50	25		
Rectangular 25x25	25	25		

Table 12.3: Upper Arm Cross Sections

12.1.4 Head

The head tube is made out of aluminum with OD of 30mm. The vertical flat bars are made out of steel with a cross section of 25mm x 10mm. The feature attached to the flat bar on the right hand side in 12.5a, used to connect the upper rod are modelled as a round bar with OD 10mm. On the physical model this is a bolted connection attaching the spherical bearing of the rod.

(a) Head Abaqus

(b) Head Lab

Part: Head	Dimensions			
Cross section name	x [mm]	y [mm]	OD [mm]	Thickness t [mm]
Tube 28.5 mm alu.			28.5	2.8
Rod conn. bar			10	-
Flat vertical bar	25	10		

Table 12.4: Head Cross Sections

12.1.5 Comment on change in cross sections

The purpose of the model, in the long run, is to run an explicit analysis with the catenary system. In an effort to optimize the model for this purpose, some of the cross-sections were altered to increase the critical time step. The change of cross section on some parts increases the stable time increment of the explicit analysis. By changing from flat bar with dimensions of 50mm x 4mm to a rectangular bar of 25mm x 25mm the critical time increment increased from 2.69e-7 seconds to 6.67e-7 seconds. The effect of this change on the relative small features is assumed neglectable when it comes to the dynamic properties compared to the gained advantage obtained by decreased simulation time.

12.1.6 Comment on the missing rods in the model

The numerical model is created without the rods. This simplification is done due of the limitations in the functions used to place parts in the assembly module of Abaqus CAE. To properly add in the rods it's required to write in Abaqus Keywords and due to time limitations this step have been omitted and link interactions are instead used. This is described more in detail in the following section.

12.2 Interaction and boundary conditions

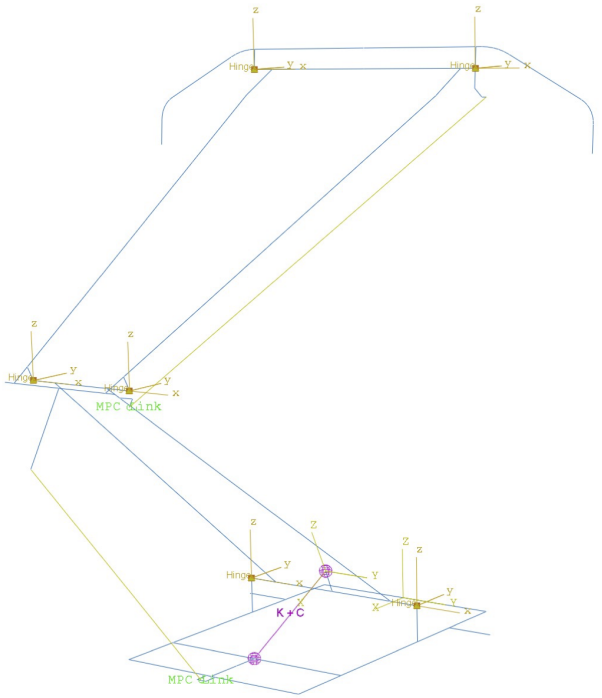

Figure 12.6: Abaqus Model with interactions rendered

The constraints and connectors used between the parts are listed in Table 12.5. Note that for the connectors the local coordinate system is rotated 90 degrees about the z-axis. So the local UR1 freedom in the hinge is in the global y-direction, UR2. The link interaction have been chosen to represent the rods. As a result, the natural frequencies of the rods will be lacking in the numerical model.

Connector/Constraint	Part 1	Part 2	Free DOFs
Hinge	Frame	Lower Arm	UR1
Hinge	Lower Arm	Upper Arm	UR1
Hinge	Upper Arm	Head	UR1
Link	Frame	Upper Arm	UR1, UR2, UR3
Link	Lower Arm	Head	UR1, UR2, UR3
Fixture points	Frame	Environment	None

Table 12.5: Connectors and constraints in model

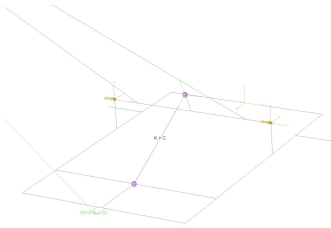

(a) Frame - Lower Arm Hinge

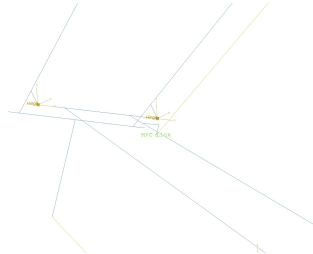

(b) Lower Arm - Upper Arm Hinge

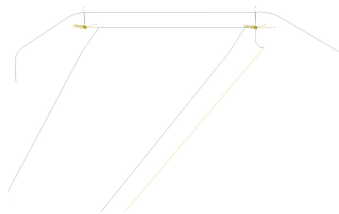

(c) Upper Arm - Head Hinge

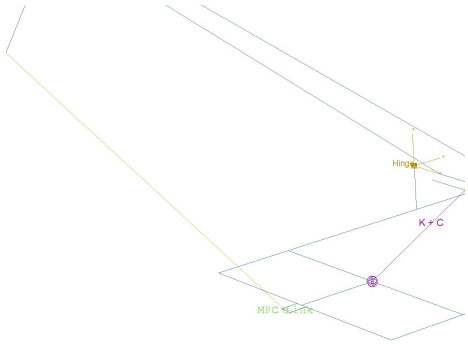

(d) Lower Rod Link

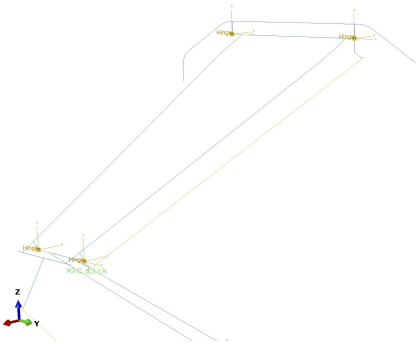

(e) Upper Rod Link

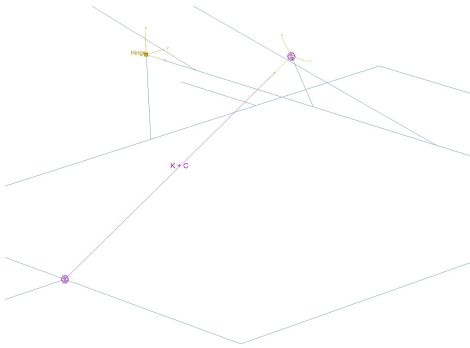

(f) Spring and Dashpot

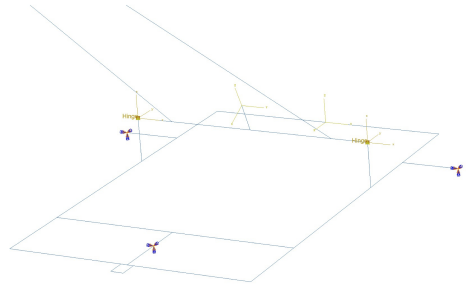

(g) Fixtures of the Frame

Figure 12.7: Interaction features and boundary conditions

12.3 Mesh

The pantograph have been meshed with B31 elements. The B31 element is a 2-node linear beam element with the active DOFS 1, 2, 3, 4, 5, and 6. I.e. translation and rotation in and around x, y and z. The B31 element utilizes lumped mass formulation as well as a default isotropic approximation of the inertia which is calculated from the sectional properties per unit length and are lumped at the nodes [Dassault Systems, 2014, ch. 3.5.5]. The B31 linear element with particle-mass lumping is known underestimate the natural frequencies of the model slightly [Cook et al., 2002, p. 379-380].

The global mesh sizes are as follows for the parts, Frame 0.035m, Lower Arm 0.035m, Upper Arm 0.035m and Head 0.01m. This is assumed sufficient to represent all modes in the frequency range of 0-200Hz without estimation errors due to lack of elements in higher order modes. The curved areas of the head have a mesh size of 0.005m.

12.4 Linear perturbation Frequency Analysis

12.4.1 Running parameters

For the analysis the Lanczos eigensolver is used, the default settings are used in both the step, and job specification. The frequencies from 0-200Hz is calculated.

12.4.2 Lumped mass at the rod connection points

Since the rods are missing in the analysis their weight have been approximated and the mass was lumped at each connection point. This is done to enhance the precision of the large modes, where the mass further out in the system, i.e., the mass on the upper arm and head, is crucial to bring the resonance frequencies down. With a wall thickness of 2mm and an outer diameter of 22mm the upper rod was estimated to be around 2kg including the spherical bearings on the end. This mass was lumped as two 1kg masses at the nodes the links are connected to.

The lower rod was calculated to be 1.5kg including the bearings on the ends when the thickness is assumed to be 2mm. The mass lumped at the node the link is connected to on the upper arm is only 0.4kg, which is lower than half of 1.5kg. This was done to counter the effect of the beam element on the upper arm, that the lower rod link is connected to, being thicker and heavier than on the physical model. A smaller mass was therefore lumped to compensate for this.

12.4.3 Constraints when estimating the head

When analyzing the natural frequencies of the head it's required to change the connection between the upper arm and the head to pinned to reduce the stiffness contribution from the upper arm to the head. This could be due to the physical connection being a simple bolt connection with plastic shims between the parts, thus a very low stiffness for rotation UR2 and UR3. The picture of the connection can be viewed in chapter 5, Figure 5.3f.

The analysis was run multiple times, both with pinned and hinged head constraint, and with and without the lumped masses resembling the accelerometers with supports placed on the head. The results can be viewed in Table 12.6.

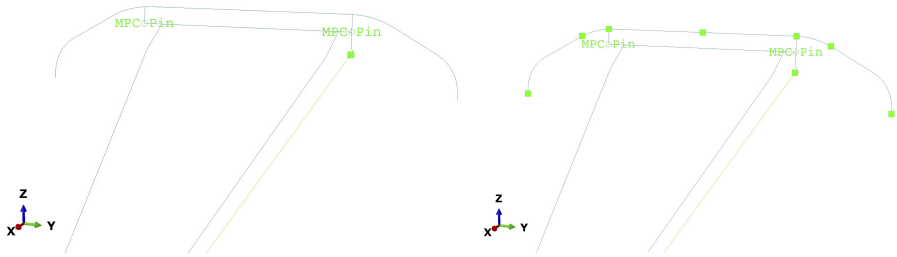

(a) Head without lumped masses **(b)** Head with lumped masses

Figure 12.8: Lumped masses placed on the head to represent the sensors

12.4.4 Constrains when estimating the rest of the system

The upper arm of the pantograph achieved the best results when hinges was used in all connections. For the lower and upper arms the analysis is run with and without the accelerometers that was used in the setups when the parts was analyzed. The green dots in the Figures below indicates the points at where the accelerometers were attached. The bellow has been modeled as a spring, and the spring stiffness has been tuned to match the first rigid body mode of the structure. The damping is from ARTeMIS assumed to be 40% in this mode, and the resonance frequency was 2.93Hz. The corresponding undamped natural frequency is therefore 3.2Hz. To achieve this natural frequency the spring stiffness had to be $4 \cdot 10^7$.

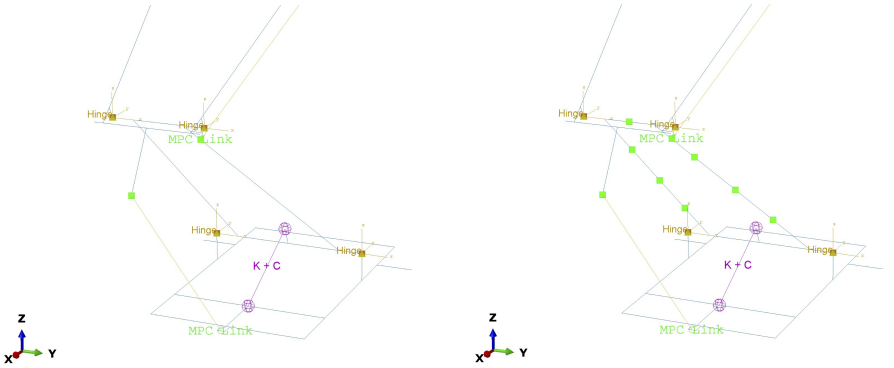

(a) Lower Arm without lumped masses **(b)** Lower Arm with lumped masses

Figure 12.9: Lumped masses placed on the Lower Arm to represent the sensors

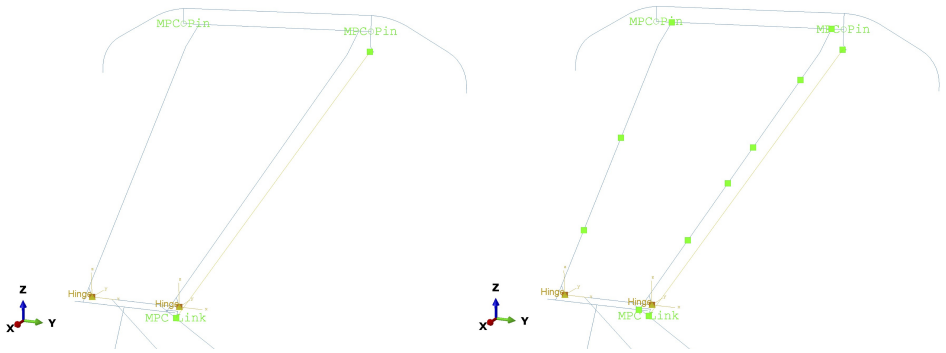

(a) Upper Arm without lumped masses **(b)** Upper Arm with lumped masses

Figure 12.10: Lumped masses placed on the Upper Arm to represent the sensors

12.5 Results

Table 12.6: Frequencies from ABAQUS

Simulation	Hinged, w/o acc.	Hinged, acc. LA	Hinged, acc. UA	Hinged, acc. Head	Pinned, w/o acc.	Pinned, acc. Head
RBM, bellow	3.229	3.224	3.190	3.179	3.228	3.170
UA, lateral swing	5.774	5.774	5.696	5.602	5.750	5.579
Knee, vertical bending	9.467	9.454	9.374	9.265	9.443	9.236
UA, twist	12.572	12.570	12.438	11.775	12.332	11.541
Knee, moving lateral	24.394	24.275	24.264	24.320	24.372	24.295
Head, ends x-dir, phase	38.184	38.185	38.001	32.742	29.966	25.812
LA, twist	41.373	41.355	40.573	40.314	40.269	38.067
UA, bending vertical, phase	43.049	43.044	42.257	42.194	42.370	41.629
UA, bend. vert. c-phase+head	43.869	43.864	43.296	41.686	43.079	41.042
Head, ends x-dir, c-phase	49.501	49.493	49.078	43.516	48.530	43.310
UA, bending lateral, c-phase	51.349	51.345	50.751	50.259	47.054	46.835
Head, ends z-dir, phase	56.620	56.644	56.561	48.557	55.956	48.434
UA, bending vertical, c-phase	67.324	67.311	66.786	59.641	64.362	57.871
LA, bending vertical, phase	74.905	73.699	74.818	74.659	74.852	74.607

Head, ends x-dir, phase: The ends of the head tube are moving in the global x-direction in phase.
LA, twist: The lower arm is twisting and transferring this throughout the upper parts.
UA, bending vertical, phase: The tubes of the upper arm are bending in phase in the vertical direction.
UA, bend. vert. c-phase+head: This is a tricky mode to explain, see the animation from Abauqus.
Head, ends x-dir, c-phase: The ends of the head tube are moving in the global x-direction in counter phase.
UA, bending lateral, c-phase: The tubes of the upper arm are bending in the lateral plane, in opposite directions.
Head, ends z-dir, phase: The ends of the head tube are moving in the global z-direction in phase.
UA, bending vertical, c-phase: The tubes of the upper arm are bending in counter phase in the vertical direction.
LA, bending vertical, phase: The lower arm is bending in the vertical diretion in phase.

Table 12.7: Frequencies from ARTeMIS estimations based on basic FDD

Setup	Head	Upper arm	Lower arm	Upper rod	Lower rod
RBM, bellow	2.930	3.125	2.930	2.930	2.930
UA, lateral swing	6.250	6.445	6.445	6.445	
Knee, vertical	8.789	8.984	8.984	8.90, 9.57	8.984
UA, twist	10.94, 12.5	11.719	11.719	11.523	11.719
Knee, moving lateral	22.070	22.070	22.070		22.070
Head, ends x-dir, phase	25.977	29.492**			
LA, twist					
UA, bending vertical, phase	43.359	40.430	40.430		40.820
UA, bend. vert. c-phase+head					
Head, ends x-dir, c-phase		48.633	47.656		
UA, bending lateral, c-phase	39.648*				
Head, ends z-dir, phase	46.875				
LA, bending vertical, phase		69.922			
UA, bending vertical, c-phase			67.969		

* could be a combination of UA, bend. vert. c-phase+head

** the head is assumed to be shifted up in frequency when the accelerometers are removed.

Table 12.6 show the frequencies of the modes with different head constraints and placement of accelerometers. The video files of the modes are handed in with the thesis and are possible to get hold of from either the university or by contacting the writers.

With bellow stiffness providing what is assumed to be the correct undamped natural frequency of the first mode causes the vertical knee bending mode and the lower arm vertical bending modes also to be overestimated. The knee bending is overestimated by 0.5Hz, and the lower arm bending mode is overestimated by 5Hz compared to the analysis performed in ARTeMIS. The contribution from the dampers in the three modes are unknown, and could possibly get the frequencies to match better in more advanced simulations including damping.

One thing to note is the effect of the weight of accelerometers with supports. For the upper arm, head, and the rods with relatively small masses the effect of adding point masses shifts the resonance frequencies of some modes quite a bit. The weight of the accelerometers with supports is 47grams. The biggest changes can be seen for the first head mode whit the connection changed to pinned from hinged, and when the masses of the accelerometers are applied. The simulation with the hinged connection and without accelerometers have a resonance frequency of 38.184Hz. Changing the connection to pinned brings it down to 29.966Hz, and with accelerometers, it is brought down to 25.812Hz.

The same effect can be seen for the twisting mode of the upper arm. Adding the accelerometers on the head, the modal mass increases with the accelerometers placed far out on the head tube, and as a result, the resonance frequency of the mode is brought down.

12.6 Discussion

The effect of the changing dynamic behavior of the bellow when the pressure is changed is important to notice here as well as the effect of the dampers mounted in the bellow assembly. By assuming a damping of 40% and tuning the first mode up to 3.2Hz, the knee vertical bending mode is overestimated compared to the results obtained in ARTeMIS. From the results in case study 5, in chapter 10, the bellow have multiple modes, still, it is modeled as one spring in the Abaqus model. This could cause the RBM-bellow mode, vertical bending in the knee, and the lower arm bending mode to not be correctly represented in the model. A possible and very likely error is the damping estimate of 40% being too high. The contribution of the damping in the bending knee mode and the bending of the lower arm is unknown.

The sensitivity of the added mass from the accelerometers was an important finding. From the results obtained with the pinned head with and without accelerometers, the large shift in frequency of the first head mode could be identified and later be seen in ARTeMIS. Also for modes such as the twisting of the upper arm, the effect of adding mass far out in the system has a large impact. Because of effects like this, the model must match the measured frequencies with masses applied, for later to remove the masses and have a correct system.

Comparing the modes and corresponding frequencies calculated in Abaqus to those found in ARTeMIS it can be seen that the first mode in Abaqus is overestimated. As mentioned, the damping is not contributing to the Abaqus simulation, and this being the most damped mode in the structure it is assumed to be too high. The second mode is the upper arm swinging in the lateral plane. This is underestimated in the Abaqus model. When the lumped masses of the upper rod was added, this mode was reduced by 1Hz. The lumped mass assumption is possibly one of the causes why this frequency is underestimated.

The vertical bending in the knee is overestimated, just like the bellow mode. It is likely that this is linked to the missing damping in the bellow assembly as this mode excites the bellow and the dampers are active or it might be too little mass model.

The twisting mode of the upper arm seems to have to little modal mass, or a too high stiffness in Abaqus. When the accelerometers are placed on the head the inertia is increased and the frequency is better matched. Also the knee, the connection between the upper- and lower arm, is swinging back and forth in the lateral direction with too high frequency. This could also be due to too high stiffness in the model, errors in the cross-sections or the lumped mass of the upper and lower rod.

The model has not been fine tuned to match the frequencies of those found in the analysis performed perfectly. This was omitted due to the large uncertainties in the measures of the pantograph, both the geometrical measurements and the measurements of the cross-sections. In Abaqus, 6 simulations were run where none of them are ideal to represent the pantograph correctly. Effects such as friction and slack in the joints should be investigated and if found, implemented in the model. The frequencies could possibly be tuned with altering the cross-sections, but effects from lumped rods, possible friction and slack in joints was not prioritized.

12.7 Conclusion

The Abaqus model successfully replicates the behavior of the pantograph in the lab at the first 6 modes and the bending of the upper arm. There is some errors in the frequencies obtained, but the modes are found to be the same. The modes above this have not been estimated for sure and no conclusion can be drawn for them.

12.8 Suggestion to future work on the Abaqus model

For future work, the rods should be added instead of using links and lumped masses. Better documentation of the pantograph analyzed should be obtained, so that the geometrical uncertainties and errors in the modeling of the pantograph is reduced. By manually measuring and modeling the pantograph, an unnecessary amount of uncertainties are introduced.

The connection of the head should be modeled such that both the head modes and the global ones coincide in one single setup without the need of multiple setups.

13 — Discussion

From the lab experiments, there are multiple things to discuss. The tests performed by sweeping from 2-195Hz worked surprisingly well. The frequency content was good and resonance frequencies and shapes have been established for all parts using this method. The servo-controller was at times difficult to adjust such that it would run the whole span, but it worked except the whole way down to 2Hz on some sweeps. What did not work well was the hammer impulse tests with the pantograph resting on the load cell. It introduced several responses when losing contact between the load cell and the pantograph head. As a result, this type of analysis was tricky to analyze with little knowledge about the pantograph behavior. This type of analysis was therefore dropped and sweeping was tested. Other improvements that would be nice to have is live tracking of the contact force used in the tests, and the possibility to test with 55N. The measurement of the contact force should also be improved where the interaction from the wire connected to the magnet is removed. The note on the lab experiments is that it is not required with as many recordings for each setup. The pantograph response is equal in multiple series tested with the same setup and the process of setting up the ARTeMIS analysis makes it very time-consuming to run multiple series of the same tests.

The pantograph used in this study is not directly interesting in the simulation aspect with a catenary system. This is due to the head being a static head without the dynamic characteristics found in an ordinary pantograph head. The regulator was tested in chapter 6, and it is clear that this is a limitation of the system. The time-consuming process of tuning the pressure as well as varying contact force over the height of operation was probably a result of the regulator. The dynamic response and characteristics of the system are assumed independent of the regulator and only the static behavior is assumed influenced by this. Notes on the cross-sections used in the pantograph are that circular cross-sections do not have clearly defined planes of deformation. The measurements performed in the lab is done on the primary axis of the parts, and the planes of deformation could be rotated with respect to the tubes. Ideally, more sensors should be used at the same time, but this requires additional ADC-channels to be able to record.

The sensor supports designed, and produced was essential to be able to get viable results for the system. Chapter 8 clearly showed that the false frequencies recorded without any additional support was removed from the system. The supports are assumed sufficient to transfer all the correct frequencies and not introduce any beneficial ones. Using the supports it is important that the cable ties securing the supports and accelerometers are tensioned adequately.

Measuring the dynamic response of the system the ideal setup would be to record the whole system at once with several accelerometers and channels. Since this was not possible the measurements were performed part wise with great success. The analysis of part for part, before comparing these made it possible to analyze several of the modes of the pantograph. In the selection of the accelerometer placements, some changes could have been made to

get some additional useful information. On the head, it would be nice to also measure the y-direction on the ends of the head tube. Additional ADC-channels would also make it possible to record the motion in the direction of travel for the head. For this pantograph with a static head, it is maybe not that interesting, but the possibility to mount even more accelerometers along the contact surface, where the catenary would be in contact would be beneficial to check for local modes along this span. The disadvantage to this is the effect of adding mass on the head alters the natural frequency to a high degree. This must, therefore, be corrected for in the numerical model with a lumped mass study.

For the upper- and lower arm it desired to measure both planes, or ideally all three axes, for all the accelerometers to determine the plane of deformation of the circular cross-sections. Now the deformation is assumed to occur in one of the primary planes recorded, and the only way to either prove this or disprove this is the two accelerometers measuring in the orthogonal direction in the setups. For the lower arm, the top accelerometer mounted on the 70mm tube should maybe be substituted with two accelerometers, placed on either side, to check for rotation in the knee joint.

The impact of resonance in the upper rod, on the rest of the structure, is large. When the upper rod hits its first resonance frequency the whole structure rocks violently. The sideways rocking on 11.6Hz and 17.5Hz have large amplitudes and the impact on the contact surface of the head is high. The upper rod often appears with two resonance frequencies. One at 16.6Hz and the other at 17.5Hz. This could be in two different planes, additional measurements with multiple axis is required in further studies. Another point to notice in the report is that frequencies of modes change a bit, this is caused by the estimators in the different analysis uses polynomial fit functions, and often shifts some of the peaks. Other times the shift of frequency is due to added mass from the accelerometers or a change in the bellow pressure. The lower rod, on the other hand, does not have any significant impact on the dynamic response of the structure. It is relatively short and stiff and the first resonance frequency have not been determined successfully.

The observed responses are presented in the video files. The files show the response from the lab, ARTeMIS and Abaqus. The worst responses with respect to amplitudes and the contact interface on the head are the first RBM-mode, the bending knee, the twisting of the upper arm, and the first mode of the upper rod. The effect of a head fitted with springs to compensate for high-frequency response would be very interesting with these modes in mind.
Comparing the results from Abaqus and ARTeMIS further, the discovery of several modes right above 40Hz in Abaqus made it clear that there were several closely spaced modes in the data analyzed with ARTeMIS. This was found after the license on ARTeMIS had expired and could therefore not be investigated further and whether or not this is real modes of the pantograph remains unknown.

13.0.1 Relevance of the thesis

The relevance of the thesis must be seen in the light of the pantograph studied. The pantograph is a measurement pantograph used on trains operating at low speed to measure the height of the contact wire. This pantograph, therefore, has less strict demands for dynamic stability compared to operational pantographs. At the same time, the design of

pantographs vary, and characteristics found for this pantograph could possibly be found in other operational pantographs utilizing some of the same principles. The procedures and findings regarding the attachment of the accelerometers and frequency sweeping, to measure the dynamic response are likely to be applicable to wide range of pantographs.

14 — Conclusion

The studies performed and presented in this thesis aimed at investigating the dynamic behavior of a pantograph, and creating a numerical model to resemble the behavior. This to enable better simulation of the pantograph catenary interaction. In order to achieve this a subset of case specific studies were performed, a modal analysis using FDD and SSI techniques were performed in ARTeMIS Modal Pro, and a numerical model of the pantograph was created in Abaqus.
The main finding in this thesis is the estimation of the dynamic response of the modes below 20Hz and the creation of a model resembling this behavior. In addition, the attachment of the sensors, and lab procedures for determining the dynamic characteristics of a pantograph have been studied and determined.

The numerical model has proven to behave in a similar fashion to the pantograph in the lab even with the simplifications and sources of error it has. By using the numerical model the effect of the added mass from the accelerometers could be studied and understood. The most critical effect is the shift of the first head mode, where the resonance frequency shifts with 4Hz. By this finding, it was possible to understand why the frequencies found when measuring on the head, not necessarily appeared in the spectrums for other parts and how sensitive the head was for the added mass.

The modal analysis was based on measurement data recorded with a laboratory setup where the pantograph delivered a contact force between 30N and 42N, and was excited with a frequency sweep from 2 Hz to 195Hz. The dynamic behavior between 0 Hz and 25 Hz is successfully identified. Consisting of six modes, vertical rigid body motion due to the bellow, lateral movement of the upper arm, rigid body movement due to the vertical knee motion, twisting of the upper arm, the first mode of the upper rod and lateral knee movement. The two modes with rigid body motion are significantly more damped than the other modes. Damping estimation was therefore challenging. The most critical modes for the contact surface of the head are the twisting of the upper arm and the first mode of the upper rod. These modes have little damping and the amplitudes are very high, as can be seen in the videos from the lab.

Modal behaviour was observed in the entire frequency domain up to 195 Hz. However, not all observed modal behaviour is sufficiently identified. The main challenge determining the modal behavior of these modes was the lack of measurement channels. Another effect complicating the estimation is to compare and combine the part by part study performed. By adding mass and changing the contact force of the pantograph, some modes shifts. To identify the response in one part, caused by another requires a good understanding of what resonance frequencies the parts in the system have and how they can transfer in the system.

The most important findings of the case specific studies was that the bellow modes shifts with increasing contact force and that due to circular cross-sections in the pantograph there was a need for sensor supports to get good measurements. The development and evaluation

of the sensor supports are also presented and deemed adequate to perform measurements up to 195Hz.

Further studies should consider a operational pantograph head, such that the dynamic behavior of the pantograph catenary interaction can be described. It is reasonable to assume that a operational pantograph head will be able to compensate for some of the twisting motion of the head, and the higher-frequency vertical movement. This effect would be very interesting to study further.

A — Appendix A

A.1 Datasheet Dytran 3583BT

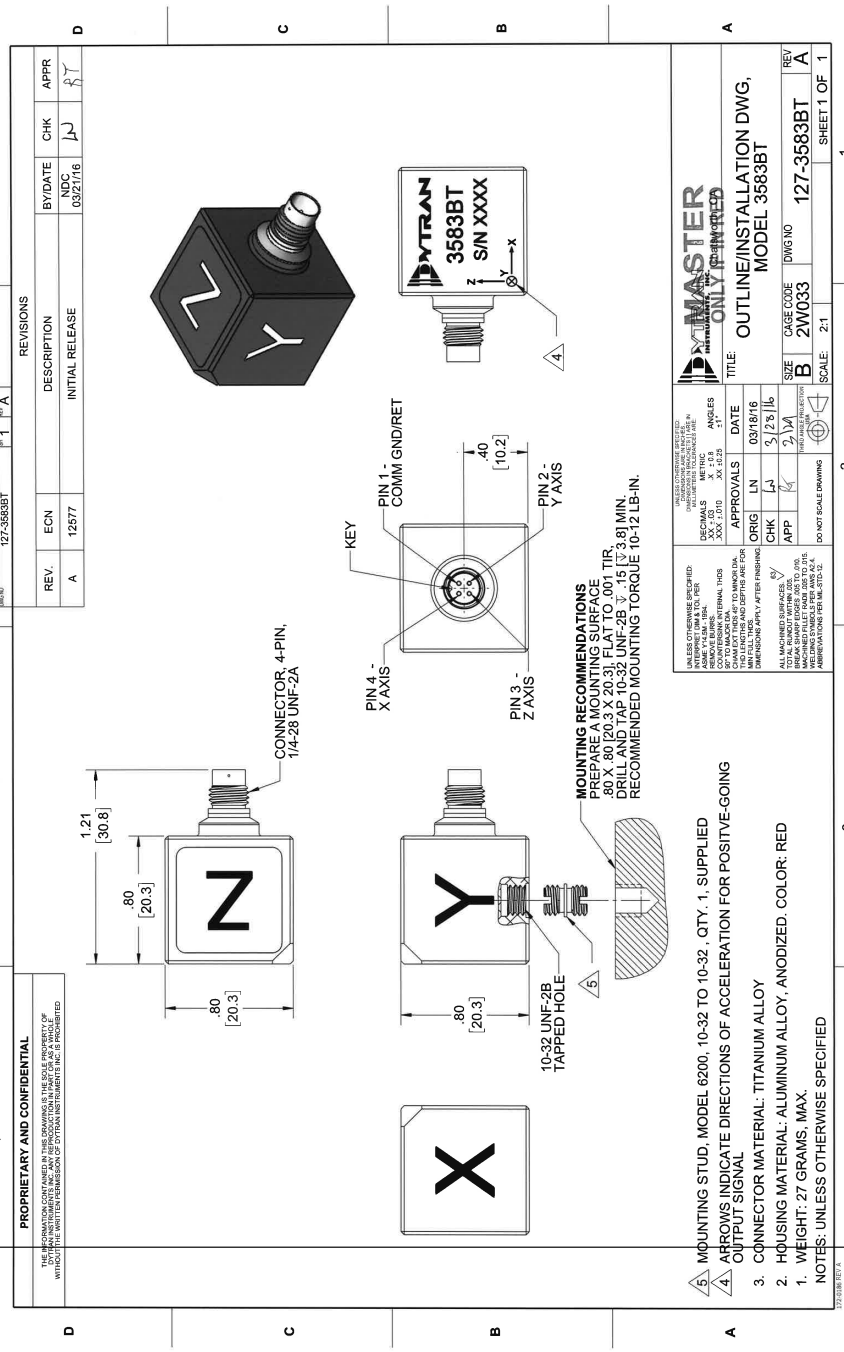

Figure A.1: Datasheet accelerometer p. 1

MODEL 3583BT	PERFORMANCE SPECIFICATIONS	DOC NO. PS3583BT
	Accelerometer, Triaxial, IEPE	REV A, ECN 12577, 03/29/16

- **HIGH SENSITIVITY**
- **LOW NOISE**
- **TEDS FEATURE**

		ENGLISH		SI	
PHYSICAL					
Weight, Max.		0.95	oz	27	grams
Connector [1]	Type	4-pin, 1/4-28		4-pin, 1/4-28	
	Material	Titanium Alloy		Titanium Alloy	
Housing	Material	Aluminum, Anodized		Aluminum, Anodized	
	Isolation	Base Isolated		Base Isolated	
Sensing Element	Material	Ceramic		Ceramic	
	Mode	Shear		Shear	
PERFORMANCE					
Sensitivity, ±10% [2]		500	mV/g	51	mV/m/s^2
Acceleration Range, ±		10	Gpeak	98.1	m/s^2 peak
Frequency Range, ±10%		0.25 to 4000	Hz	0.25 to 4000	Hz
Resonance Frequency		>15	kHz	>15	kHz
Linearity [3]		1	%F.S.	1	%F.S.
Transverse Sensitivity Max		6	%	6	%
Noise floor		0.0002	Grms	0.002	m/s^2 rms
Spectral Noise	1Hz	30	µGrms/sqr(Hz)	294.3	µm/s^2 rms/sqr(Hz)
	10Hz	7	µGrms/sqr(Hz)	68.67	µm/s^2 rms/sqr(Hz)
	100Hz	9	µGrms/sqr(Hz)	88.29	µm/s^2 rms/sqr(Hz)
	1000Hz	1	µGrms/sqr(Hz)	9.81	µm/s^2 rms/sqr(Hz)
	10000Hz	1	µGrms/sqr(Hz)	9.81	µm/s^2 rms/sqr(Hz)
ELECTRICAL					
Supply Current Range [4]		2 to 20	mA	2 to 20	mA
Compliance Voltage Range		+18 to +30	VDC	+18 to +30	VDC
Output Impedance, Typ.		100	Ω	100	Ω
Output Bias Voltage		11 to 13	VDC	11 to 13	VDC
Discharge Time Constant		1.0 to 2.0	sec	1.0 to 2.0	sec
TEDS Feature		IEEE 1451.4		IEEE 1451.4	
ENVIRONMENTAL					
Shock Max		1000	Gpeak	9810	m/s^2
Vibration Max		50	Gpeak	491	m/s^2
Operating Temperature		-60 to +185	°F	-51 to +85	°C
Seal		Epoxy		Epoxy	
Magnetic Sensitivity at 100 Gauss		0.00009	g/Gauss	0.0008829	m/s^2/Gauss
Base Strain Sensitivity, Max		0.002	g/µε	0.01962	m/s^2/µε

This family also includes:

Model	Sensitivity (mV/g)	Range (Gpeak)	Resolution (Grms)	Oper. Temp (°F)	TC(sec.)

Refer to the performance specifications of the products in this family for detailed description

Supplied Accessories:

1) Accredited Calibration Certificate (ISO 17025)
2) Mounting stud, model 6200 (10-32 to 10-32)

Notes:

[1] Mates with Dytran cable Model 6811AXX or 6824AXX (XX denotes length in feet)
[2] Measured at 100 Hz, 1 Grms per ISA RP 37.2
[3] Measured using zero-based straight line method, % of F.S. or any lesser range.
[4] Do not apply power to this system without current limiting, 20 mA MAX. To do so will destroy the IC amplifier
[5] In the interest of constant product improvement, Dytran reserves the rights to change specifications without notice.

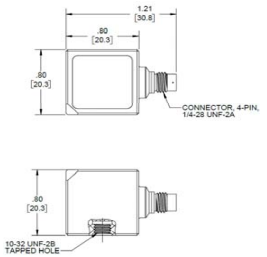

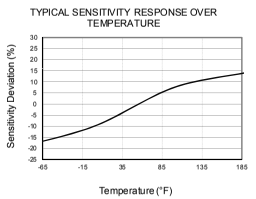

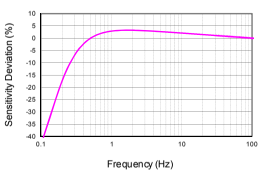

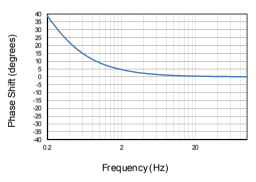

Units on the line drawing are in inches, units in brackets are in millimeters. Refer to 127-3583BT for more information.

21592 Marilla Street, Chatsworth, California 91311 Phone: 818.700.7818 Fax:818.700.7880
www.dytran.com For permission to reprint this content, please contact info@dytran.com

Figure A.2: Datasheet accelerometer p. 2

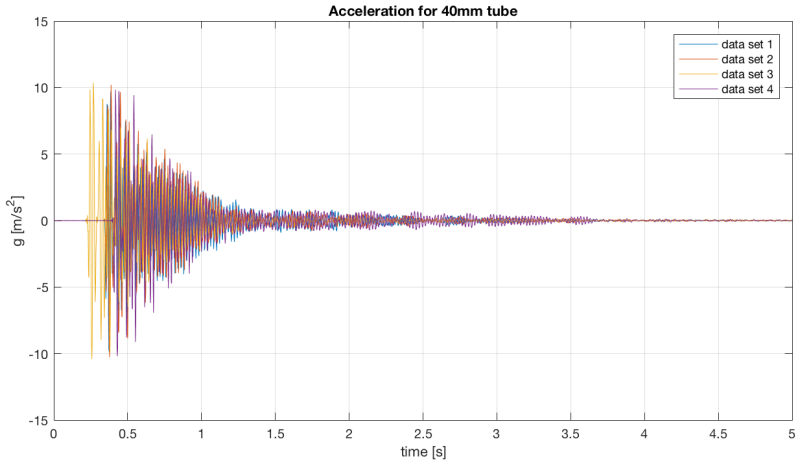

Figure A.3: Time series system response without supports, 40mm

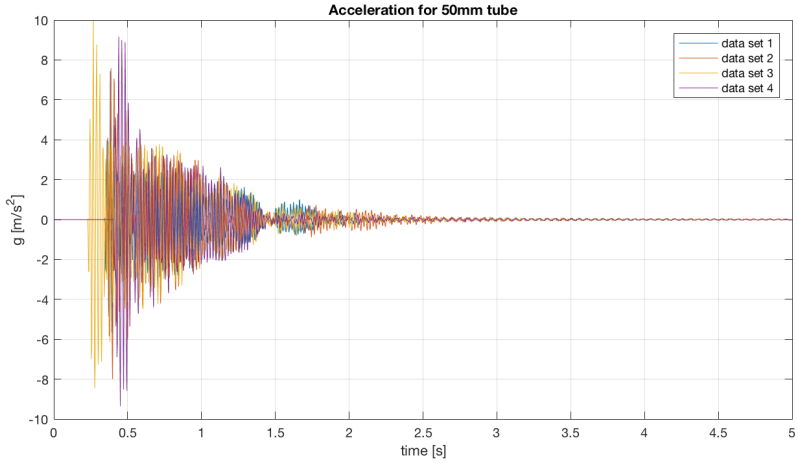

Figure A.4: Time series system response without supports, 50mm

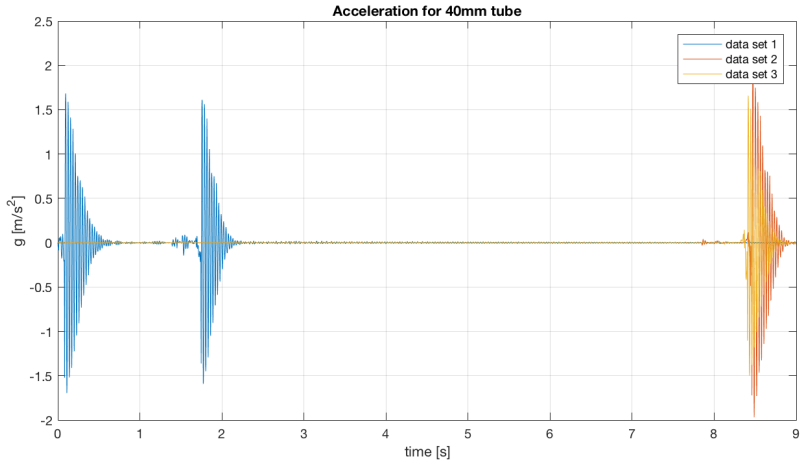

Figure A.5: Time series sensor rocking on 40mm tube

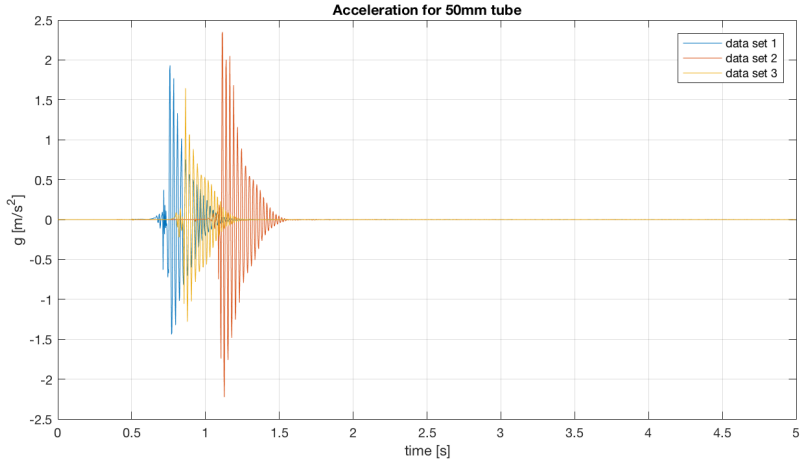

Figure A.6: Time series sensor rocking on 50mm tube

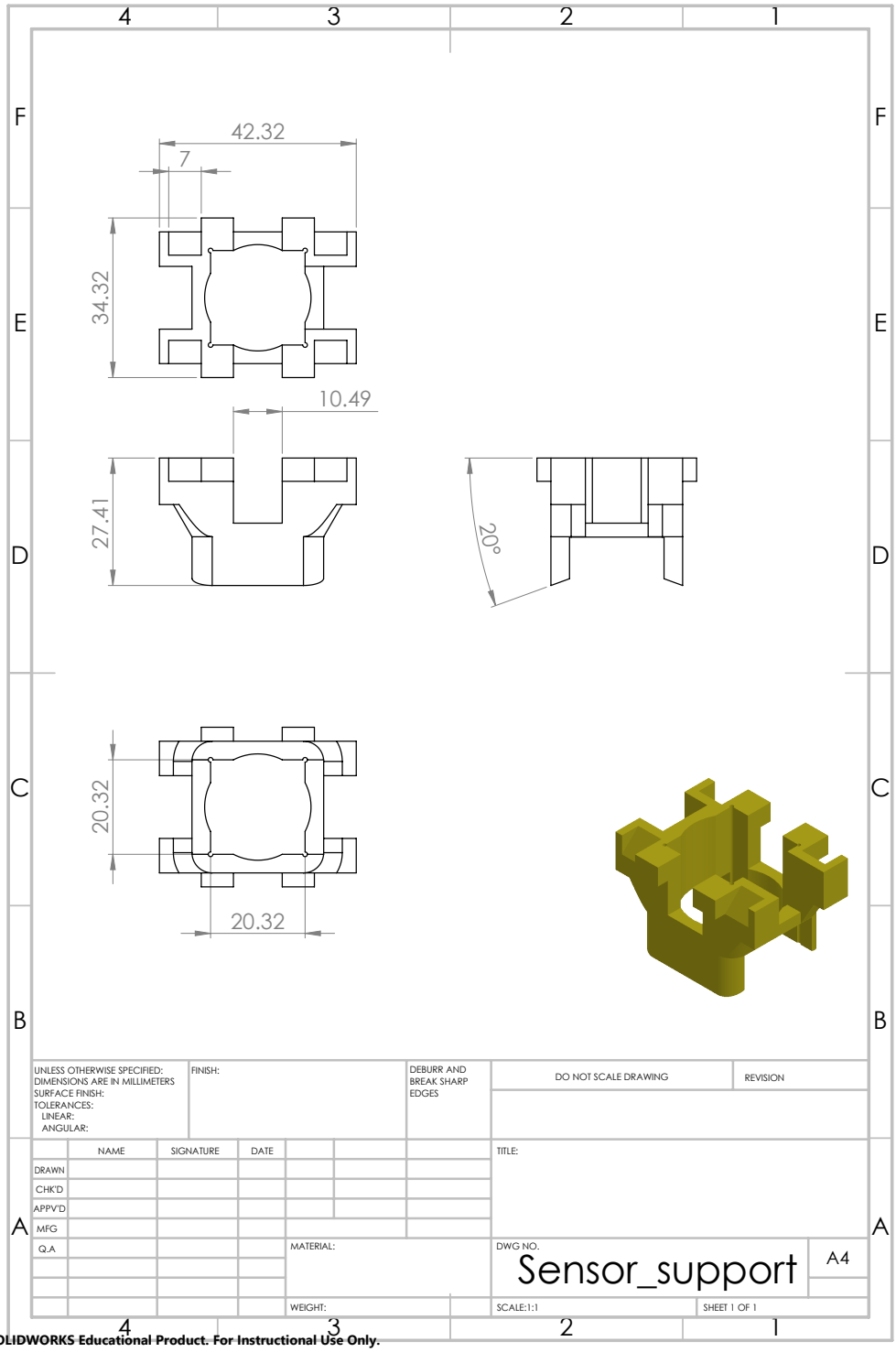

Figure A.7: Drawings of sensor supports

A.2 Spectrums from 10 without RBM removed

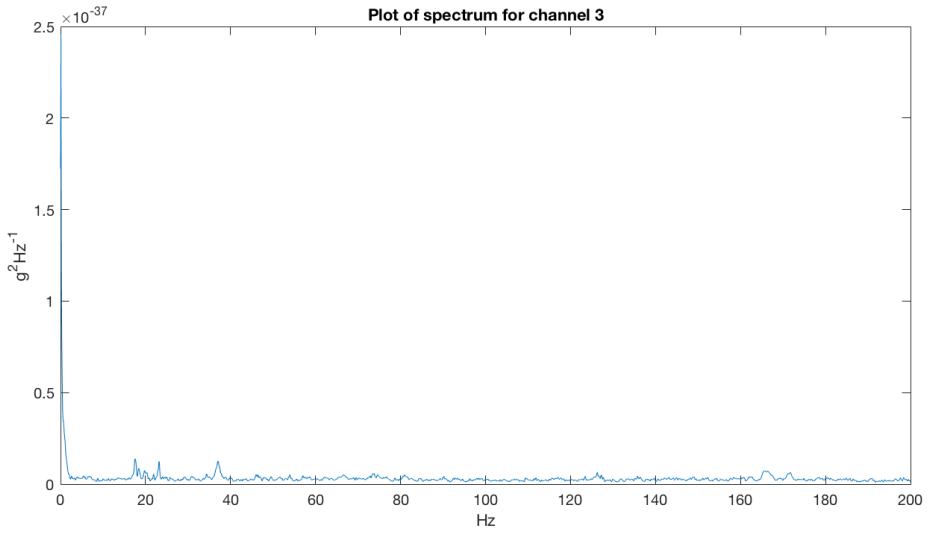

(a) Peaks channel 3

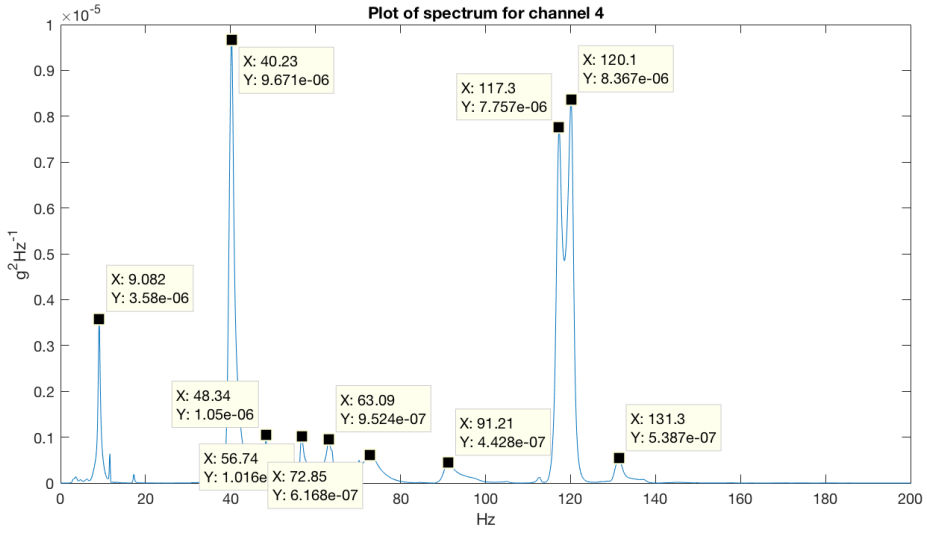

(b) Peaks channel 4

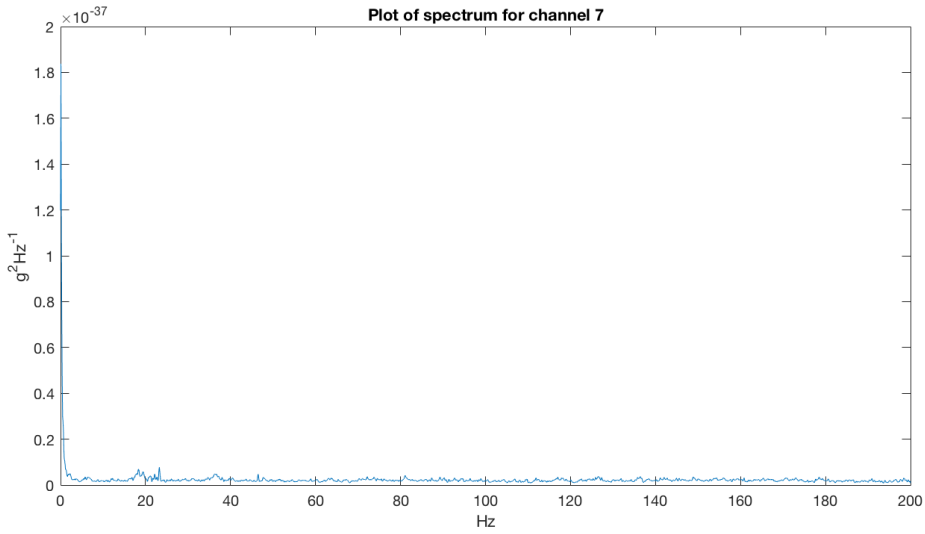

(c) Peaks channel 7

Figure A.8: Spectrums with peaks without RBM removed

A.3 Spectrums from 10 with RBM removed

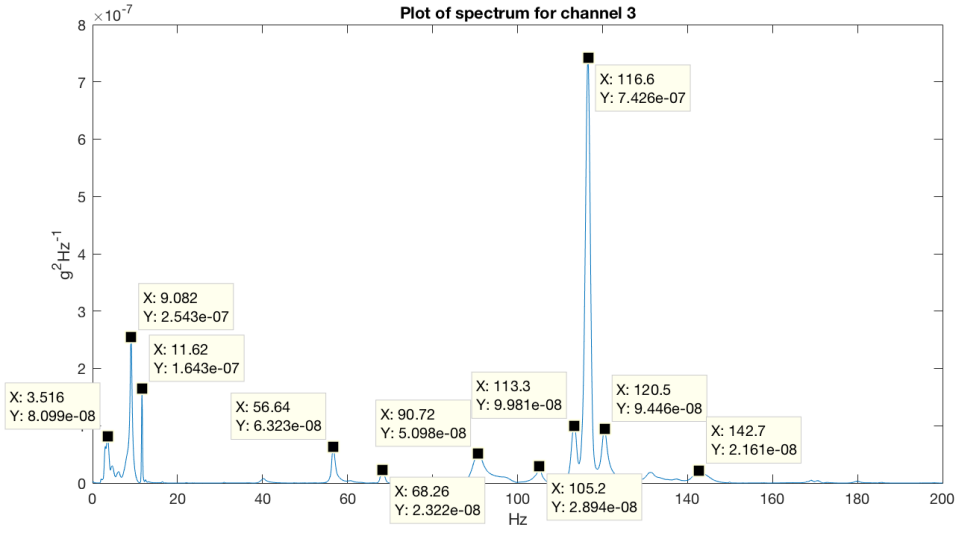

(a) Peaks channel 3

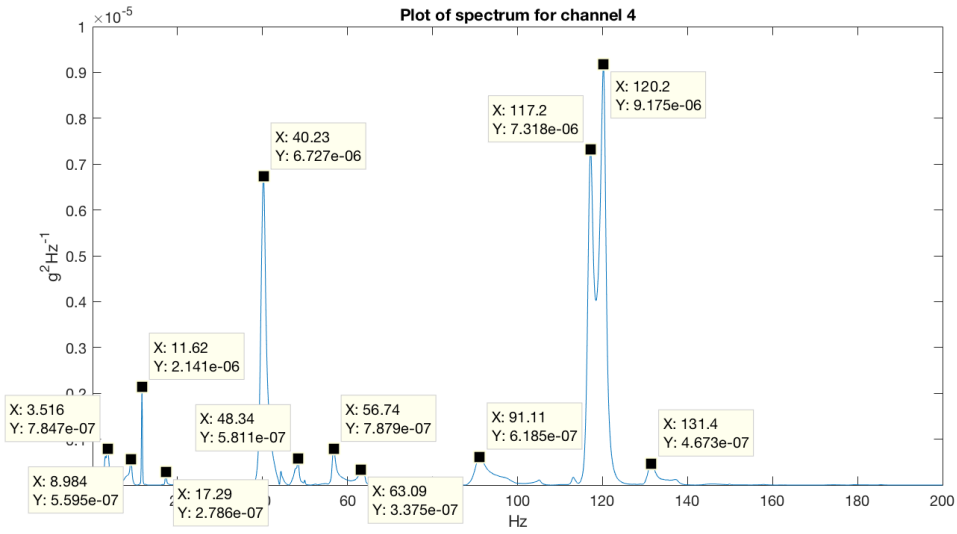

(b) Peaks channel 4

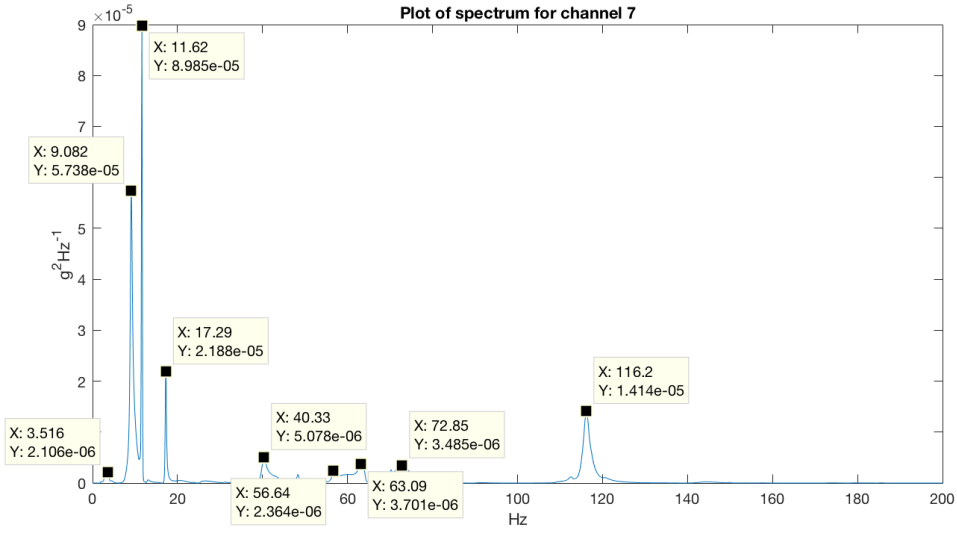

(c) Peaks channel 7

Figure A.9: Spectrums with peaks with RBM removed

A.4 Matlab code, Upper_Arm_Z_direction_sweep.m

```
1  %   General script to create spectrums and find mode shapes from
       measurements
2  %Brief code description
3  %20-32, the .mat files are imported and running parameters such as
        low- and highpass filters, cutting of the times series are
       defined.
4  %33-54, Since the series varies in length due to the manual
       process of starting recording and the sweep the shortest
       series are found and all the data are copied into one 3
       dimensional matrix.
5  %               The values are also converted from mV to G (9.81m/
       s^2).
6  %55-82 the time series are cut if the parameters are set.
7  %83-93 plots the acceleration data of one data set, as well as all
        the series in one figure.
8  %94-122 removes the mean from the time series and filters out the
       rigid body motion described above.
9  %123-151 defines the low- and highpass filters and applies them to
        the time series if opted.\medskip
10 %152-161 plots the filtered acceleration data.
11 %162-175 generates the spectrum for the time series with Welch's
       method.
12 %176-185 does the same for the filtered time series.
13 %186-196 plots the spectrums and the averaged spectrum.
14 %197-207 does the same for the spectrums generated of the filtered
        time series.
15 %208-212 plots the two different spectrums in the same plot to
       compare them.\medskip
16 %213-255 the frequencies of the peaks are used to estimate the
       mode shapes by using cross correlation between the channels.
17 clear all; close all; clc;
18
19 % transformation constant from voltage to acceleration 51mV/m/s^2
20 %% USE CUSTOM TIME? ... FILTER? ... Import mat files to analyse -
        define number of series
21 dataset_1_mat = '/Users/John-Arne/Dropbox/NTNU/Master/matlab/
       converted_to_g/05.10/2018-05-10-14-28-59_cut.mat'; load(
       dataset_1_mat); %data_set_full_1(:,:) = dataout(:,:);
22 dataset_2_mat = '/Users/John-Arne/Dropbox/NTNU/Master/matlab/
       converted_to_g/05.10/2018-05-10-14-33-26_cut.mat'; load(
       dataset_2_mat); %data_set_full_2(:,:) = dataout(:,:);
23  dataset_3_mat = '/Users/John-Arne/Dropbox/NTNU/Master/matlab/
       converted_to_g/05.10/2018-05-10-14-37-37.mat'; load(
       dataset_3_mat); data_set_full_3(:,:) = dataout(:,:);
24 % dataset_4_mat = '2018-04-12-14-16-05.mat'; load(dataset_4_mat);
       data_set_full_4(:,:) = dataout(:,:);
25 % dataset_5_mat = '2018-04-12-14-19-02.mat'; load(dataset_5_mat);
```

```
    data_set_full_5(:,:) = dataout(:,:);
number_of_timeseries = 3;
f_hz=400;
% set = 1 if custom time should be used
set_custom_time = 0;
use_lowpass     = 0;
use_highpass    = 0;
find_mode_shapes = 1;
%%  Check what series beeing the shortest with respect to samples, copy new data arrays and define time vector
min_length = length(data_set_full_1(:,1));
    if length(data_set_full_2)<min_length
        min_length = length(data_set_full_2(:,1));
    end
    if length(data_set_full_3)<min_length
        min_length = length(data_set_full_3(:,1));
    end
%     if length(data_set_full_4)<min_length
%         min_length = length(data_set_full_4(:,1));
%     end
%     if length(data_set_full_5)<min_length
%         min_length = length(data_set_full_5(:,1));
%     end
% add the sets to a X*12*n dimm array
for i=1:min_length
    data_temp(i,:,1) = data_set_full_1(i,:)./(0.50031); % 1/ ( [51 mV/ m/s^2] * 9.81) = 1/0.50031 from voltage to g
    data_temp(i,:,2) = data_set_full_2(i,:)./(0.50031);
    data_temp(i,:,3) = data_set_full_3(i,:)./(0.50031);
%     data_temp(i,:,4) = data_set_full_4(i,:)./(0.50031);
%     data_temp(i,:,5) = data_set_full_5(i,:)./(0.50031);
end
%%  SET CUSTOM TIME ...
% If custom time is used
if (set_custom_time == 1)
    %%% ....
    t0      = 9;
    tend    = 14;
    %%% ....
    t_length=tend-t0;
    dt=1/f_hz;
    nt=t_length*f_hz;
    t=[0:dt:dt*(nt-1)];
    for j=1:nt                                  % Copy the series with shorter length to only contain the specified time
        for n = 1:number_of_timeseries
            i = j+round(t0*f_hz);
            data(j,:,n) = data_temp(i,:,n);
        end
    end
```

```
72
73 % If ordinary time is used
74 else
75     for n=1:number_of_timeseries            % just copying them to
           get the names right
76         data(:,:,n) = data_temp(:,:,n);
77     end
78
79     nt = min_length;              % shortest length found
80     dt = 1/f_hz;                  % timestep depending on the
           sampling frequency
81     t  = [0:dt:dt*(nt-1)];        % time vector with correct length
           and time step for further analysis
82 end
83 %%  Plot acceleration data     ..... SELECT CHANNEL TO PLOT
84 channel_to_plot = 5; % remember to add 1 to the channel index due
       to matlab starting lists with index 1, not 0
85 figure(); plot(t,data(:,channel_to_plot,1)); title(['Plot of
       accelerationdata for channel ',num2str(channel_to_plot-1)]);
       xlabel('time [s]'); ylabel('g [m/s^2]'); grid on;
86 %figure(); plot(t,data(:,channel_to_plot,1)); title(['Acceleration
       for 50mm tube']); xlabel('time [s]'); ylabel('g [m/s^2]');
       grid on;
87
88 legend_text{1} =['data set 1'];
89 hold on;
90 for n = 2 : number_of_timeseries
91     plot(t,data(:,channel_to_plot,n)); legend_text{n}=['data set '
           num2str(n)];
92 end
93 legend(legend_text);
94 %%  Remove mean from signals, find RIGID BODY MOTION contributions
       and filter them out
95
96 for i = 1:length(data(1,:,1))            %   Remove mean from
       series for all channels
97     for n=1:number_of_timeseries
98         data(:,i,n) = data(:,i,n) - mean(data(:,i,n));
99     end
100 end
101 %{
102 % Define left, and right end acceleration vectors for further
       calculation
103 left_end_channel = 4;
104 right_end_channel = 8;
105 for n=1:number_of_timeseries            % Copy the left and right
       channel data
106     left_end(:,n) = data(:,left_end_channel,n);
107     right_end(:,n) = data(:,right_end_channel,n);
108 end
```

```
109 for n = 1:number_of_timeseries %  Using left, and right end to
    calculate the translation and angle of the RBM.
110     translation(:,n) = left_end(:,n)./2 + right_end(:,n)./2;
111     angle(:,n) = left_end(:,n)./(1.947)-right_end(:,n)./(1.947);
112 end
113 % Define channels for sensors and distance from centre
114 sensor_numers = [4,5,10,6,7,8];
115 sensor_distances = [-0.9735, -0.5755, -0.2885, 0.0785, 0.5555,
    0.9735];
116
117 for n=1:number_of_timeseries
118     for i = 1:length(sensor_numers)
119             data(:,sensor_numers(i),n) = data(:,sensor_numers(i),n
                ) - translation(:,n) + angle(:,n).*
                sensor_distances(i);
120     end
121 end
122 %}
123 %%  Module for LOWPASS or HIGHPASS filter
124 if (use_lowpass == 1)
125     % All frequency values are in Hz.
126     Fs = 400;  % Sampling Frequency
127
128     N     = 48;  % Order
129     Fpass = 55;  % Passband Frequency
130     Fstop = 63;  % Stopband Frequency
131     Wpass = 4;   % Passband Weight
132     Wstop = 5;   % Stopband Weight
133     dens  = 24;  % Density Factor
134
135     % Calculate the coefficients using the FIRPM function.
136     b  = firpm(N, [0 Fpass Fstop Fs/2]/(Fs/2), [1 1 0 0], [Wpass
        Wstop], {dens});
137     Hd = dfilt.dffir(b);
138     for n=1:number_of_timeseries
139         for ch = 1:length(data(1,:,1))
140             data_filtered(:,ch,n) = filter(Hd,data(:,ch,n));
141         end
142     end
143 elseif (use_highpass == 1)
144    for n=1:number_of_timeseries
145         for ch = 1:length(data(1,:,1))
146             data_filtered(:,ch,n) = filter(Hd,data(:,ch,n));
147         end
148     end
149 else
150     print('no filter applied');
151 end
152 %%  Plot FILTERED acceleration data
153 if (use_lowpass==1 || use_highpass == 1)
```

```
154     figure(); plot(t,data_filtered(:,channel_to_plot,1)); title(['
            Plot of FILTERED accelerationdata for channel ',num2str(
            channel_to_plot-1)]); xlabel('time [s]'); ylabel('
            acceleration [g]');
155     legend_text{1} =['data set 1'];
156     hold on;
157     for n = 2 : number_of_timeseries
158         plot(t,data_filtered(:,channel_to_plot,n)); legend_text{n
                }=['data set ' num2str(n)];
159     end
160     legend(legend_text);
161 end
162 %%  Welch's method
163 Nwelch  = 10;
164 Nwindow = round(length(t)/Nwelch);
165 nfft    = 2^nextpow2(Nwindow);
166 Fs      = 1/(t(2)-t(1));
167
168 for n = 1:number_of_timeseries                  %   create spectrums,
        rectwin, hanning
169     [Sddot(:,:,n) freq_axis] = pwelch(data(:,:,n),hanning(Nwindow)
            ,[],nfft,Fs,'onesided');
170 end
171 Sddot_average(:,:) = Sddot(:,:,1)./number_of_timeseries;        %
        create average of the spectrums
172 areal_under_Sddot_ch_4 = trapz(freq_axis,Sddot_average(:,5));
173 for n=2:number_of_timeseries
174     Sddot_average(:,:) = Sddot_average(:,:)+Sddot(:,:,n)./
            number_of_timeseries;
175 end             %
176 %%  Welch's method for FILTERED SIGNAL
177 if (use_lowpass==1 || use_highpass == 1)
178     for n = 1:number_of_timeseries                  %   create
            spectrums, rectwin, hanning
179         [Sddot_filtered(:,:,n) freq_axis_filtered] = pwelch(
                data_filtered(:,:,n),rectwin(Nwindow),[],nfft,Fs,'
                onesided');
180     end
181     Sddot_average_filtered(:,:) = Sddot_filtered(:,:,1)./
            number_of_timeseries;       %   create average of the
            spectrums
182     for n=2:number_of_timeseries
183         Sddot_average_filtered(:,:) = Sddot_average_filtered(:,:)+
                Sddot_filtered(:,:,n)./number_of_timeseries;
184     end             %
185 end
186 %%  Plot spectrums
187 figure(); plot(freq_axis,Sddot_average(:,channel_to_plot)); title
        (['Plot of spectrum for channel ', num2str(channel_to_plot-1)
        ]); xlabel('Hz'); ylabel('g^2Hz^{-1}');
```

```
188 %figure(); plot(freq_axis,Sddot_average(:,channel_to_plot)); title
    (['Spectrum position 16, z-direction, 10 Welch windows']);
    xlabel('Hz'); ylabel('g^2Hz^{-1}');
189
190 figure(); plot(freq_axis,Sddot(:,channel_to_plot,1)); title(['
    Spectrums for channel ', num2str(channel_to_plot-1)]);
191 legendtext{1}=['data set 1']; hold on; xlabel('Hz'); ylabel('g^2Hz
    ^{-1}');
192 for n = 2 : number_of_timeseries
193     plot(freq_axis,Sddot(:,channel_to_plot,n));
194     legend_text{n} = ['data set ' num2str(n)];
195 end
196 legend(legend_text);
197 %%  Plot FILTERED spectrums
198 if (use_lowpass==1 || use_highpass == 1)
199     figure(); plot(freq_axis_filtered,Sddot_average_filtered(:,
        channel_to_plot)); title(['Plot of spectrum for FILTERED
        channel',num2str(channel_to_plot-1)]); xlabel('Hz');
        ylabel('g^2Hz^{-1}');
200     figure(); plot(freq_axis_filtered,Sddot_filtered(:,
        channel_to_plot,1)); title(['Spectrums for FILTERED
        channel ', num2str(channel_to_plot-1)]);
201     legendtext{1}=['data set 1']; hold on;  xlabel('Hz'); ylabel('
        g^2Hz^{-1}');
202     for n = 2 : number_of_timeseries
203         plot(freq_axis_filtered,Sddot_filtered(:,channel_to_plot,n
            ));
204         legend_text{n} = ['data set ' num2str(n)];
205     end
206     legend(legend_text);
207 end
208 %% Compare spectrums
209 if (use_lowpass==1 || use_highpass == 1)
210     figure(); plot(freq_axis,Sddot_average(:,channel_to_plot));
        title(['Compare FILTERED to non-filtered spectrum for
        channel ',num2str(channel_to_plot-1)]);
211     hold on; plot(freq_axis_filtered,Sddot_average_filtered(:,
        channel_to_plot)); grid on; legend({'non-filtered','
        FILTERED'});
212 end
213 %%  Find mode shapes and plot them
214 %   frequencies where mode shapes should be determined
215 if find_mode_shapes == 1
216     %frequencies = [3.125, 9.082, 11.62, 17.24, 40.23, 48.44,
        56.64, 63.13, 68.16, 72.61, 91.02, 105.2, 113.5, 117.1,
        120.2, 131.6, 137.4, 143.1, 162, 168.7];
217     frequencies = [3.516, 11.62, 9.082, 17.29, 40.23, 56.64,
        117.3, 63.09, 120.5, 48.34, 131.4, 90.72, 68.26, 72.85,
        105.2, 113.3, 142.7];
218     %frequencies = [9.082, 40.23, 48.34, 63.09, 117.3, 56,73.
```

```
        72.85, 120.1, 131.3, 91.21];
219     subplot_dimm = [5,4]; % Define dimmensions of the
            subplotfigure for mode shapes
220     channels = [4,5,10,6,7,8]; % Channels to cross correlate
221     ref_channel_index = 2; % Specify the list index of the
            reference channel for the CSPD-plot from the channel index
             list
222     %x_coordinates = [0, 0.418, 0.895, 1.262, 1.549, 1.947];
223     x_coordinates = [0, 0.398, 0.685, 1.052, 1.529, 1.947]; % x-
            coordinate for the sensors in the mode shape plot
224     for i=1:length(channels) % Create cross spectrums for the
            different channels
225         for n = 1:number_of_timeseries
226             [Sddot_cross(:,i,n) csp_freq_axis] = cpsd(data(:,
                    channels(i),n),data(:,channels(ref_channel_index),
                    n),hanning(Nwindow),[],nfft, Fs,'onesided');
227         end
228         Sddot_cross_average(:,i) = Sddot_cross(:,i,1)./
                number_of_timeseries;
229         for n = 2:number_of_timeseries
230             Sddot_cross_average(:,i)= Sddot_cross_average(:,i) +
                    Sddot_cross(:,i,n)./number_of_timeseries;
231         end
232
233     end
234     %   plot cross spectral density
235     figure(); plot(csp_freq_axis, Sddot_cross_average); grid on;
            title('CPSD-plot')
236     df_cross = csp_freq_axis(2)-csp_freq_axis(1); % find timestep
            on frequency axis
237     df_freq = freq_axis(2)-freq_axis(1);
238     figure();
239     for i = 1:length(frequencies)
240         for j=1:length(channels)
241             temp = real(Sddot_cross_average( round(frequencies(i)/
                    df_cross+1),j) );
242             if temp > 0
243                 sign(i,j)=1;
244             elseif temp < 0
245                 sign(i,j)=-1;
246             else
247                 sign(i,j)=1;
248             end
249             phi(i,j) = (abs( Sddot_cross_average( round(
                    frequencies(i)/df_cross+1),j ) /
                    Sddot_cross_average( round(frequencies(i)/df_cross
                     +1),ref_channel_index) ) )*sign(i,j);
250         end
251
252         subplot(subplot_dimm(1),subplot_dimm(2),i);
```

```
253         phi(i,:) = (phi(i,:)-min(phi(i,:)))./(max(phi(i,:))-min(
                phi(i,:)));
254         plot(x_coordinates,phi(i,:)); title(['Frequency ' num2str(
                frequencies(i)), 'Hz']); grid on; %xlabel('position
                along arm [m]')
255     end
256     %save('spectrum_supp.mat','Sddot_average');
257     %save('freq_axis_supp.mat','freq_axis');
258 end
259 figure();
260 plot(freq_axis,Sddot_average(:,5)); title('spectrum ch4 and ch6');
        hold on;
261 plot(freq_axis,Sddot_average(:,7),'r');
262 %%  Find mode shapes on other arm
263 %   frequencies where mode shapes should be determined
264 if find_mode_shapes == 1
265     channels_2 = [12, 3, 2]; % Channels to cross correlate
266     ref_channel_index_2 = 1; % Specify the list index of the
            reference channel for the CSPD-plot from the channel index
            list
267     %x_coordinates = [0, 0.418, 0.895, 1.262, 1.549, 1.947];
268     x_coordinates_2 = [0.398, 1.052, 1.947]; % x-coordinate for
            the sensors in the mode shape plot
269     for i=1:length(channels_2) % Create cross spectrums for the
            different channels
270         for n = 1:number_of_timeseries
271             [Sddot_cross_2(:,i,n) csp_freq_axis_2] = cpsd(data(:,
                    channels_2(i),n),data(:,channels(ref_channel_index
                    ),n),hanning(Nwindow),[],nfft, Fs,'onesided');
272         end
273         Sddot_cross_average_2(:,i) = Sddot_cross_2(:,i,1)./
                number_of_timeseries;
274         for n = 2:number_of_timeseries
275             Sddot_cross_average_2(:,i)= Sddot_cross_average_2(:,i)
                    + Sddot_cross_2(:,i,n)./number_of_timeseries;
276         end
277     end
278     %   plot cross spectral density
279     figure(); plot(csp_freq_axis_2, Sddot_cross_average_2); grid
            on; title('CPSD-plot')
280     df_cross_2 = csp_freq_axis_2(2)-csp_freq_axis_2(1); % find
            timestep on frequency axis
281 figure();
282     for i = 1:length(frequencies)
283         for j=1:length(channels_2)
284             temp = real(Sddot_cross_average_2( round(frequencies(i
                    )/df_cross_2+1),j) );
285             if temp > 0
286                 sign_2(i,j)=1;
287             elseif temp < 0
```

```
288                     sign_2(i,j)=-1;
289                 else
290                     sign_2(i,j)=1;
291                 end
292                 phi_2(i,j) = (abs( Sddot_cross_average_2(round(
                        frequencies(i)/df_cross+1),j ) /
                        Sddot_cross_average_2( round(frequencies(i)/
                        df_cross +1),ref_channel_index_2) ) )*sign_2(i,j);
293             end
294
295             subplot(subplot_dimm(1),subplot_dimm(2),i);
296             phi(i,:) = (phi(i,:)-min(phi(i,:)))./(max(phi(i,:))-min(
                    phi(i,:)));
297             plot(x_coordinates_2,[phi_2(i,:)]); title(['Frequency '
                    num2str(frequencies(i)), 'Hz']); grid on; %xlabel('
                    position along arm [m]')
298         end
299         %save('spectrum_supp.mat','Sddot_average');
300         %save('freq_axis_supp.mat','freq_axis');
301     end
302     figure();
303     subplot(6,2,1);
304     for i=1:length(phi(:,1));
305         phi(i,:) = (phi(i,:)-min(phi(i,:)))./(max(phi(i,:))-min(phi(i
                ,:)));
306     end
307     for i=1:length(phi_2(:,1));
308         phi_2(i,:) = (phi_2(i,:)-min(phi_2(i,:)))./(max(phi_2(i,:))-
                min(phi_2(i,:)));
309     end
310     plot(x_coordinates,phi(1,:)); title(['Frequency ' num2str(
            frequencies(1)),'Hz, left arm']); grid on; %xlabel('position
            along arm [m]')
311     subplot(6,2,2);
312     plot(x_coordinates_2,phi_2(1,:),'r'); title(['Frequency ' num2str(
            frequencies(1)),'Hz, right arm']); grid on; %xlabel('position
            along arm [m]')
313     subplot(6,2,3);
314     plot(x_coordinates,phi(2,:)); title(['Frequency ' num2str(
            frequencies(2)),'Hz, left arm']); grid on; %xlabel('position
            along arm [m]')
315     subplot(6,2,4);
316     plot(x_coordinates_2,phi_2(2,:),'r'); title(['Frequency ' num2str(
            frequencies(2)),'Hz, right arm']); grid on; %xlabel('position
            along arm [m]')
317     subplot(6,2,5);
318     plot(x_coordinates,phi(3,:)); title(['Frequency ' num2str(
            frequencies(3)),'Hz, left arm']); grid on; %xlabel('position
            along arm [m]')
319     subplot(6,2,6);
```

```
320 plot(x_coordinates_2,phi_2(3,:),'r'); title(['Frequency ' num2str(
        frequencies(3)),'Hz, right arm']); grid on; %xlabel('position
        along arm [m]')
321 subplot(6,2,7);
322 plot(x_coordinates,phi(4,:)); title(['Frequency ' num2str(
        frequencies(4)),'Hz, left arm']); grid on; %xlabel('position
        along arm [m]')
323 subplot(6,2,8);
324 plot(x_coordinates_2,phi_2(4,:),'r'); title(['Frequency ' num2str(
        frequencies(4)),'Hz, right arm']); grid on; %xlabel('position
        along arm [m]')
325 subplot(6,2,9);
326 plot(x_coordinates,phi(5,:)); title(['Frequency ' num2str(
        frequencies(5)),'Hz, left arm']); grid on; %xlabel('position
        along arm [m]')
327 subplot(6,2,10);
328 plot(x_coordinates_2,phi_2(5,:),'r'); title(['Frequency ' num2str(
        frequencies(5)),'Hz, right arm']); grid on; %xlabel('position
        along arm [m]')
329 subplot(6,2,11);
330 plot(x_coordinates,phi(8,:)); title(['Frequency ' num2str(
        frequencies(8)),'Hz, left arm']); grid on; %xlabel('position
        along arm [m]')
331 subplot(6,2,12);
332 plot(x_coordinates_2,phi_2(8,:),'r'); title(['Frequency ' num2str(
        frequencies(8)),'Hz, right arm']); grid on; %xlabel('position
        along arm [m]')
333
334 % save stuff
335 % save('x_coordinates.mat','x_coordinates');
336 % save('modeshapes.mat','phi');
337 % save('frequencies.mat','frequencies');
338
339 % save('x_coordinates_RBM_removed.mat','x_coordinates');
340 % save('modeshapes_RBM_removed.mat','phi');
341 % save('frequencies_RBM_removed.mat','frequencies');
```

Bibliography

Randel J. Allemang. The modal assurance (mac) criterion - twenty years of use and abuse. *J. Sound Vibr., V. 37*, pages 14–23, 2003.

J. Ambrósio, J. Pombo, M. Pereira, P. Antunes, and A. Mósca. Recent developments in pantograph-catenary interaction modelling and analysis. *International Journal of Railway Technology, Volume 1, Issue 1, p. 249-278, 2012*, pages 249–250, 2012.

Rune Brincker and Carlos Ventura. *Introduction to Operational Modal Analysis*. John Wiley & Sons Ltd, 2015.

Robert D. Cook, David S. Malkus, Michael E. Plesha, and Robert J. Witt. *Concepts and applications of finite element analysis*. John Wiley and Sons. Inc., 4th edition, 2002.

Dassault Systems. *Abaqus 6.14 Documentation*, 2014. http://ivt-abaqusdoc.ivt.ntnu.no:2080/v6.14/index.html, (visited 2018-05-22).

National Instruments. *Understanding FFTs and Windowing*, december 2016. Part of their Instrument Fundamentals Series, http://www.ni.com/white-paper/4844/en/.

Jernbaneverket. *Approval of new trains, Pantographs and pantograph-overhead contact line interaction*, second edition, April 2007. NES TS-01 2007-01-31.

Laurent Mevel Michael Döhler, Palle Anderson. Variance computation of modal parameter estimates from upc subspace identification. *IOMAC'17, 7th International Operational Modal Analysis Conference*, 2017.

Surajit Midya, Dierk Bormann, Thorsten Schutte, and Rajeev Thottappillila. Pantograph arcing in electrified railways—mechanism and influence of various parameters—part i: With dc traction power supply. *IEEE Transactions on Power Delivery, Issue 4, Oct. 2009*, pages 1931–1932, 2009. http://ieeexplore.ieee.org/abstract/document/5235869/?reload=true (visited 2018-01-28).

David Edvard Newland. *An Introduction to Random Vibrations, Spectral and Wavelet Analysis*. Dover Publications, 3rd edition, 2012.

Bart De Moor Peter van Overschee. *Subspace Identification for Linear Systems, Theory Implementation Applications*. Kluwer Academic Publishers Group, softcover reprint of the hardcover 1st edition edition, 1996.

Palle Anderson Rune Brincker. Method for vibration analysis. *US patent no. US 6779404 B1*, 1999.

S. Rao Singiresu. *Mechanical Vibrations*. Pearson Education, Inc., 5th edition, 2011.